

Modeling Electromagnetic Fields in Strongly Inhomogeneous Media

An Application in MRI

K. Koolstra

Delft University of Technology



MODELING ELECTROMAGNETIC FIELDS IN STRONGLY INHOMOGENEOUS MEDIA

AN APPLICATION IN MRI

by

K. Koolstra

in partial fulfillment of the requirements for the degree of

Master of Science
in Applied Mathematics

at the Delft University of Technology,
to be defended publicly on Thursday September 24th, 2015 at 1.30 PM.

Student number:	4062442
Project duration:	January 5 th , 2015 – September 24 th , 2015
Supervisor:	Dr. ir. M.B. van Gijzen, TU Delft Dr. ir. R. Remis, TU Delft W. Brink, MSc. LUMC
Thesis committee:	Dr. ir. M.B. van Gijzen, TU Delft Dr. ir. R.F. Remis, TU Delft Dr. J.L.A. Dubbeldam, TU Delft Prof. dr. ir. C. Vuik, TU Delft W. Brink, MSc. LUMC

An electronic version of this thesis is available at <http://repository.tudelft.nl/>.

Abstract

Modeling electromagnetic fields in MRI involves two main challenges: the solution of the scattering problem resulting from Maxwell's equations has to be accurate and it has to be obtained within short computation time. In this thesis a method that meets both requirements is searched for.

The method of moments with rooftop basis functions is used to discretize different formulations of the volume integral equation corresponding to Maxwell's equations. A simple two-layer cylinder test case is used to compare each solution with a derived analytical solution for scattering on a two-layer cylinder. Two types of errors are analyzed. The good performance of a staggered grid with respect to a non-staggered grid shows that the way of treating the mixed derivative terms is of great importance. The performance of a higher order approximation scheme on a non-staggered grid is close to the performance of a second order approximation scheme on a staggered grid. A contrast study shows that these two methods are particularly beneficial for high contrasts and on low resolution.

The performance of the iterative solvers IDR(s) and GMRES is tested for each discretization method. IDR(4) shows excellent performance in reducing the computation time that is obtained with GMRES. Finally, human body simulations confirm the findings from the two-layer cylinder test case.

Keywords Electromagnetic scattering · High permittivity materials · Magnetic resonance modeling · Volume integral equation · Galerkin's method

PREFACE

During the last years of the Applied Mathematics study program it became clear to me that numerical mathematics and modeling have my main interest. I am happy that I have been able to combine this form of mathematics with my interest for medical applications. Rob Remis, assistant professor in the Circuits and Systems group at the TU Delft, introduced me to the 'C.J. Gorter Center for High-field MRI', which is part of the Leiden University Medical Center. Here I spent parts of my weeks working on electromagnetic numerical simulations. Weekly Gorter meetings made me realize how much research is going on in the MRI field and how much can still be done. It has been an inspiring environment and a nice variation on EWI's third floor. I look back on an educational time and I hope that this thesis will pass my knowledge on to the reader.

Time has flown fast and I am realizing now that in a couple of weeks this adventure will come to an end. Before I will step into my next adventure, I would like to use this opportunity to thank all that have helped me, in any possible way, during the last nine months.

Special thanks to my supervisors Rob Remis, Martin van Gijzen and Wyger Brink, who have surrounded me with enthusiasm and have given me the opportunity to indicate my own path. I would like to express my gratitude to Andrew Webb, who has shown a lot of patience and has offered new possibilities. Thank you, Jeroen van Gemert, for your support on various subjects. Finally, I would like to thank the rest of the Gorter group (and the Men Cave in particular), for offering me a nice place to work from.

*Kirsten Koolstra
Delft, September 2015*

CONTENTS

1	Introduction	1
1.1	Problem Formulation, The Goal, and The Way to Get There.	2
1.2	Thesis Outline	3
2	A Brief Overview of Magnetic Resonance Imaging and its Challenges	5
3	The Electric and Magnetic Fields in MRI	7
3.1	Maxwell's Equations	7
3.2	Boundary Conditions	8
3.3	The Volume Integral Equation	10
3.4	The Scattering Problem	12
3.4.1	Different Formulations of the Scattering Problem	14
4	The Analytical Solution of Scattering on a Two-Layer Conducting Cylinder	17
4.1	Maxwell's equations in Cylindrical Coordinates	18
4.2	The General Solution	19
4.3	Scattering on a Two-Layer Conducting Circular Cylinder	19
5	The Method of Moments	23
5.1	Weak Form	23
5.2	Discretization	24
5.3	Choice of Test Functions	25
5.3.1	Galerkin's Method	26
5.3.2	Point Collocation Method	26
5.4	Choice of Basis Functions	27
6	Model	29
6.1	Mesh	29
6.2	Rooftop Basis and Test Functions	30
6.3	The EVIE Model	31
6.4	The DVIE Model	34
6.5	The DVIE Model on a staggered grid	36
6.6	Higher Order Difference Schemes	37
6.6.1	Fourth Order Central Difference Scheme for a Non-Staggered Grid	38
6.6.2	Fourth Order Central Difference Scheme for a Staggered Grid	38
7	Iterative Solvers	41
7.1	A non-Hermitian Operator	41
7.2	GMRES	42
7.3	IDR(s)	43
7.4	Preconditioning	43
8	Numerical Simulations and Results	45
8.1	Accuracy of the Solution	46
8.1.1	Comparison of Accuracy	46
8.1.2	The Effect of the Contrast on the Accuracy	47
8.1.3	Error Reduction	48
8.2	Efficiency of the Iterative Solver	48
8.2.1	Comparison of IDR(4) and GMRES	49
8.2.2	The Effect of the Contrast on the Convergence Behavior	49
8.2.3	The Choice of the Parameter s in IDR(s)	50

9	Back to Reality	67
9.1	Accuracy	68
9.2	Computation Time	68
10	Conclusion	71
11	Discussion	73
A	List of used variables and their SI units	75
B	Inverse Fourier Transform of the Green's Function	77
C	Weakening of the Green's Function	79
	Bibliography	81

1

INTRODUCTION

Modeling electromagnetic fields has its application in many research areas. One of them is medical imaging, in which the goal is to produce in vivo human images. The arrival of the MRI (Magnetic Resonance Imaging) scanner and its concept in 1969 has led to a whole new world of possibilities. Low-field scanners with strengths under 1 Tesla have transformed gradually into ultra high-field scanners with strengths reaching over 12 Tesla in order to obtain high resolution images. However, the advancement of high-field scanners has brought along technical challenges like heat production, field inhomogeneities and interference patterns. In order to propose suitable solutions to these problems, mathematical models that provide insight in the physics behind these problems are built.

The starting point of these mathematical models is Maxwell's equations, a set of equations that describes the propagation of electromagnetic fields in media. For decades, scientists have been developing and testing new discretization schemes to solve Maxwell's equations numerically. Each method results in different accuracy and convergence behavior. [1], [2], [3],[4],[5], [6], [7]

The different methods can roughly be divided into two groups. The first group of methods chooses Maxwell's equations in partial differential form as a starting point. The finite-difference time-domain and the finite element method are examples of methods in this group. The second group rewrites Maxwell's equations into so-called volume integral equations, a type of integro-differential equations. The method of moments is an example of this type. Even though methods in the latter group involve full matrices and are therefore computationally expensive, the method of moments is a popular method. The main reason for this preference is that the Sommerfeld radiation condition does not have to be implemented via complicated boundary conditions.

It is not without good reason that new methods are still being proposed. Modeling electromagnetic fields involves challenges that must be dealt with carefully.

The human body contains many different tissue types that all have their own permittivity values. Strong differences in materials result in electromagnetic fields that are discontinuous in space. It is well known that approximating discontinuous functions is not always straightforward. Maxwell's equations tell us even more about the discontinuous behavior: it is the normal component of the electric field that is discontinuous across material interfaces. The continuity of the tangential component and the discontinuity of the normal component raise the question whether there is an optimal discretization method that takes into account both the discontinuous and the continuous behavior. Next to the boundary conditions of material interfaces, also the boundary conditions of the domain have to be implemented such that an infinite domain is simulated. Absorbing boundary conditions or perfectly matched layers are often used for this. [8]

In the case of MRI, the computational domain is the whole human body. Because of memory limitations it is therefore necessary to obtain accurate solutions at low resolution. This requirement is also related to the final challenge: in order to work towards mathematical models applicable in the clinical field, the computation time has to be short, even for 3D simulations.

With the above challenges in mind, one method is chosen and investigated further in this thesis. In 1991, P. Zwamborn proposed a method of moments solution using so-called 'rooftop' basis functions. [7] This procedure resulted in a discretization scheme in which the derivatives acting on the vector potential are approximated using finite difference schemes. Many people have thereafter integrated the finite difference approach

in existing codes, which eventually led to multiple variants of P. Zwamborn's 'rooftop' method. [9], [10] In order to limit the research field, all studied variants in this thesis have the rooftop functions as basis and test functions. These functions live on a structured rectangular grid, which is beneficial for a short computation time. Efficient FFT algorithms can be used to evaluate matrix vector multiplications. The variants studied in this thesis differ in the approximated unknowns. More specifically, the equation of interest is formulated in terms of the electric field and in terms of the electric displacement. Each formulation provides a different starting point for a discretization procedure. Finally, some of the variants use a staggered grid, whereas other approaches use non-staggered grids.

1.1. PROBLEM FORMULATION, THE GOAL, AND THE WAY TO GET THERE

Even though various challenges in building a numerical model have been pointed out, there are two aspects that deserve attention in this research. The first aspect, which is the main focus in this thesis, is the accuracy of the studied discretization schemes. One of the models that is being studied in ongoing research turned out to show strong inaccuracies in the neighborhood of material interfaces. These inaccuracies showed the discrepancy between Maxwell's boundary conditions for material interfaces and numerical results. The specific absorption rate in the human body grows with the square of the magnitude of the electric field, and therefore these strong but very local inaccuracies might have severe effects in applications that use this numerical scheme to design medical tools. Without further corrections, inaccuracies can falsely predict heat production in the human body which will lead to change of measures. It is therefore desired to investigate the cause of the inaccuracies and to find improvements where possible.

The second part that receives attention in this thesis is the computation time of the algorithms used. In advanced tools inverse scattering problems can be solved by repeatedly solving forward problems in an iterative way. For large objects like the human body, computation time becomes a limiting factor. Decreasing the computation time of one forward problem is the first step in speeding up the final process. In literature the generalized minimal residual (GMRES) method is a commonly used method and more recent methods have not been studied yet for the MRI application. This offers an opening for new research.

To be concrete, the main goal of this research is twofold.

1. The numerical solution must be accurate on low resolution.
2. The numerical solution must be obtained within short computation time.

To meet the first requirement two different formulations of the volume integral equation are implemented. The first formulation has the electric field as unknown and the second formulation has the electric displacement as unknown. As a third model the latter formulation is implemented on a staggered grid. Finally, variations on those models are studied by implementing higher order difference schemes.

All methods will be tested for a simple test case so that the solutions can be compared with a derived analytical solution. The inaccuracies are localized for each method and the accuracies are mutually compared along 1D reference lines. Values for the global error as well as for the maximum error are studied as a function of grid size. A contrast dependence study is performed to investigate how the accuracy of each method changes for different contrast values and therefore different applications. Comparison between the different methods should bring forward the most accurate candidate on low resolution for this particular test case. A smoothing solution is proposed to decrease the strong and local inaccuracies and the effect is presented.

To meet the second requirement, the performance of the common GMRES method is compared with the performance of the induced dimension reduction (IDR(s)) method. The convergence behavior is studied for both methods and the computation time is studied as a function of the number of unknowns. Finally, the number of iterations is studied as a function of relative permittivity for both methods. A conclusion on the most efficient solver will be drawn based on these results.

To get more insight into human body simulations and to work towards 3D body simulations, a human body model 'Duke' is used to produce a realistic scattering object. The outcomes on the most accurate solution and most efficient solver are verified by studying the performance of the staggered and the non-staggered methods for 2D scattering on one slice of a 3D human body model.

1.2. THESIS OUTLINE

The thesis outline is as follows:

Chapter 2: A Brief Overview of Magnetic Resonance Imaging and its Challenges

Chapter 2 gives a short explanation on the techniques used in MRI. This will help the reader to put the derived mathematical formulations in the right context.

Chapter 3: The Electric and Magnetic Fields in MRI

Chapter 3 describes Maxwell's equations with its corresponding boundary conditions and from these equations the volume integral form is derived. The relations between the electric field, the electric displacement and the electric current are used to derive two variants on the original volume integral equation.

Chapter 4: The Analytical Solution of Scattering on a Two-Layer Conducting Cylinder

Chapter 4 provides the reader with the analytical solution of the scattering problem for a two-layer conducting infinitely long cylinder. The derivation can be found here as well.

Chapter 5: The Method of Moments

The general numerical discretization procedure is discussed in this chapter. Two types of weighting procedures are outlined and one of them will be used for the actual models in this thesis.

Chapter 6: Models

The so-called EVIE model, DVIE model on a non-staggered grid and DVIE model on a staggered grid are derived here. Ready to use discretized equations are presented for all three models. Variations on those models are derived by constructing higher order central difference schemes.

Chapter 7: Iterative Solvers

The discretized system is solved using iterative schemes. A brief summary on the properties of two good candidates are discussed here. Good candidates are considered GMRES and IDR(s).

Chapter 8: Numerical Simulations and Results

Chapter 8 discusses the obtained numerical results in detail. The main focus is on the accuracy of the different derived methods. Comparison is done by studying a two-layer cylinder test case for which an analytical solution has been derived. A convergence study is done here as well to draw conclusions on the efficiency of iterative solvers.

Chapter 9: Back to Reality

The numerical simulation is performed on one slice of a real human body model. The results will help drawing conclusions in the next chapter.

Chapter 10: Conclusion

In this chapter the final conclusions will be drawn based on the results from Chapter 8 and Chapter 9.

Chapter 11: Discussion

Finally, the thesis ends with a critical look back on the work done. Recommendations for further research should encourage the reader to continue the accuracy study in the future.

Throughout the report constants will be presented upright, vectors will be presented upright in bold, matrices will be defined with capitals and scalar functions will be shown in italic script. A list of all the variables that are used in this thesis together with their SI units can be found in [Appendix A](#).

2

A BRIEF OVERVIEW OF MAGNETIC RESONANCE IMAGING AND ITS CHALLENGES

Magnetic resonance imaging (MRI) is a popular technique that offers the opportunity to take a look inside the human body. Unlike computed tomography (CT) MRI does not involve damaging X-rays and it is therefore often seen as a key to the future. It is also a complicated technique based on fundamental physics and electromagnetism. This chapter will shortly explain the basic principle of MRI.

In the MRI-scanner a large coil produces a magnetic field (B_0). The field lines of this induced magnetic field are schematically shown in Figure 2.1. A large part of the human body contains hydrogen atoms, which all act as small magnets. Under influence of the B_0 field the net spin of the individual hydrogen spins aligns along the B_0 field lines. Once this stage has been reached, an RF (radio frequency) pulse is sent toward the human body. This causes a large part of the spins to flip, usually with 90 degrees. In this stage, signal can first be measured. Once the RF pulse is released, the hydrogen atoms start to relax toward their original state. During this process the decrease in signal can be measured. A high signal corresponds with a large amount of hydrogen atoms and a low signal with a small amount of hydrogen atoms. A gradient in the B_0 field introduces phase encoding and frequency encoding and in this way high and low signals can be linked to locations in the human body. The amount of signal contains information about the tissue type and this information can be translated into greyscale images via inverse Fourier transforms. The focus on different tissue types in these images can be shifted by changing the time at which the signal is measured during the relaxation process. This is the idea behind T1 weighted and T2 weighted images. [11]

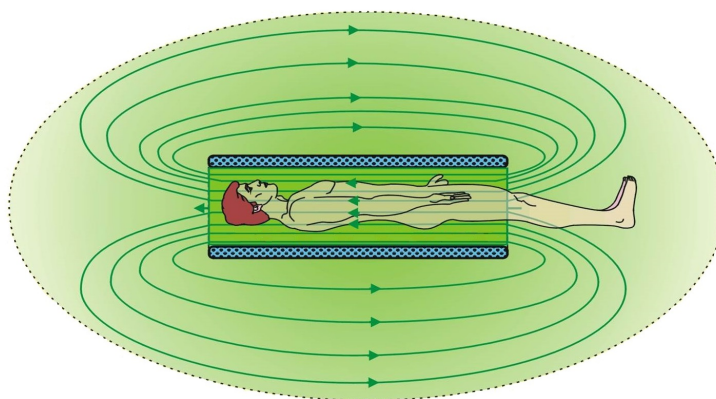
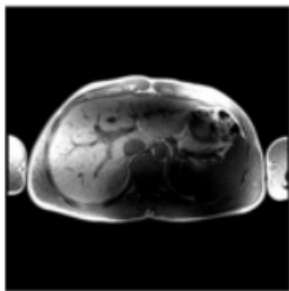


Figure 2.1: Magnetic field lines in an MRI scan.

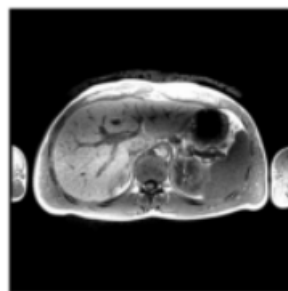
The overall aim in ongoing MRI research is to produce high quality images. One way to improve the quality is by increasing the total amount of signal. By placing the patient in a stronger magnetic field the net spin of all

proton spins increases, which improves the signal-to-noise ratio. In theory this sounds nice and easy, but in practice two important phenomena have to be taken into account.

First of all, the heat production in the human body grows proportional to the square of the magnitude of the electric field. Unfortunately, heat production can be an uncomfortable and sometimes harmful side effect for the patient. Safety guidelines fix the field intensity that is allowed in the human body and cannot be ignored. Second, the wavelength of an electromagnetic wave is inversely proportional to the strength of the magnetic field. This means that increasing the field strength of an MRI-scan leads to wavelength reduction of the electromagnetic waves. When these wave travels through the human body, the wavelength is even further reduced. If the wavelength is small compared to the size of the human body, interference patterns will occur that result in dark and blurry areas in reconstructed images. An example of this effect can be seen in Figure 2.2a, which shows a reconstructed image of the abdomen.



(a) Conventional abdominal imaging.



(b) The effect of a dielectric pad.

Figure 2.2: Abdominal imaging with and without dielectric pad. [12]

To tackle the above described phenomenon the dielectric pad has been developed. A dielectric pad is a small bag filled with a high permittivity material and it is positioned on the patient during an MRI-scan. The physics behind the dielectric pad is not fully understood yet, but the pads have shown to improve field homogeneity and contrast-to-noise ratio. [12],[13],[14] The effect can be seen in Figure 2.2b. However, the dielectric pad is patient specific and requires a fast and accurate design procedure for each patient.

The design procedure is performed by numerical modeling, which is where mathematics is involved. The pad is therefore a clear example in which modeling of the electromagnetic fields is essential. In the modeling part the challenges discussed in the introduction are all present and need to be dealt with. But before any modeling can be done the physics needs to be written down mathematically. This will be done in the next chapter.

3

THE ELECTRIC AND MAGNETIC FIELDS IN MRI

Electromagnetism has been studied by many physicists. James Clerk Maxwell, a physicist and mathematician, fully understood the physics and was able to transform experimental results into mathematical equations in the nineteenth century. His derived equations were called Maxwell's equations and they describe how electric and magnetic fields propagate and interact. They form the basis of classical electrodynamics and are therefore important in understanding the fields in MRI.

Maxwell's equations are discussed in Section 3.1. The material boundary conditions that complement Maxwell's equations are derived in Section 3.2. They will be important when developing the models in Chapter 6. In this study the focus is on the volume integral equation approach, so in Section 3.3 the volume integral formulation is derived from Maxwell's equations, along with its different variations. The derivation of the first volume integral formulation can also be found in [15].

3.1. MAXWELL'S EQUATIONS

Maxwell's equations are given by

$$-\nabla \times \mathbf{H} + \mathbf{J} + \frac{\partial \mathbf{D}}{\partial t} = -\mathbf{J}^{\text{ext}} \quad (3.1)$$

$$\nabla \times \mathbf{E} + \frac{\partial \mathbf{B}}{\partial t} = -\mathbf{K}^{\text{ext}}. \quad (3.2)$$

The variables \mathbf{J}^{ext} and \mathbf{K}^{ext} are the external sources and are therefore known. More specifically, the external magnetic source is always zero. Both sources start to act at $t = 0$. The unknowns are related via the constitutive relations,

$$\mathbf{D} = \varepsilon \mathbf{E} \quad (3.3)$$

$$\mathbf{B} = \mu \mathbf{H} \quad (3.4)$$

$$\mathbf{J} = \sigma \mathbf{E}, \quad (3.5)$$

where σ is the conductivity of the material, ε is the permittivity and μ is the permeability. In this study only nonmagnetic media will be considered, which means that $\mu = \mu_0$ where μ_0 is the permeability of vacuum. The unknown fields are the electric field strength \mathbf{E} and the magnetic field strength \mathbf{H} . Both fields vanish everywhere for $t < 0$. \mathbf{D} and \mathbf{B} are the electric displacement field and the magnetic flux density respectively.

To complete Maxwell's equations, the compatibility relations are derived by taking the divergence of (3.1) and (3.2). This yields

$$\nabla \cdot \mathbf{J} + \frac{\partial}{\partial t} \nabla \cdot \mathbf{D} = -\nabla \cdot \mathbf{J}^{\text{ext}} \quad (3.6)$$

$$\frac{\partial}{\partial t} \nabla \cdot \mathbf{B} = 0. \quad (3.7)$$

The total current is defined by $\mathbf{J}^{\text{tot}} = \mathbf{J} + \mathbf{J}^{\text{ext}}$ and with $\nabla \cdot \mathbf{D} = \rho$ (3.6) becomes $\nabla \cdot \mathbf{J}^{\text{tot}} + \frac{\partial \rho}{\partial t} = 0$, which means that there is conservation of charge. From (3.7) it follows that $\nabla \cdot \mathbf{B}$ is constant in time and because of the initial condition it follows that this constant is zero. Therefore,

$$\begin{aligned}\nabla \cdot \mathbf{D} &= \rho \\ \nabla \cdot \mathbf{B} &= 0.\end{aligned}$$

In summary, Maxwell's equations describe that magnetic fields can be created by a change in electric field or by an electric current. A changing magnetic field creates an electric field. The strength of the electric field is related to the distance away from the charge and the divergence of the magnetic flux density is always zero.

3.2. BOUNDARY CONDITIONS

Maxwell's equations in partial differential form are only valid inside homogeneous or smoothly changing media, because derivative terms appear in the formulation. Material boundary conditions can be derived, [16], from Maxwell's equations in integral form,

$$\oint \mathbf{H} \cdot d\mathbf{l} = \iint \mathbf{J} \cdot d\mathbf{S} + \frac{\partial}{\partial t} \iint \mathbf{D} \cdot d\mathbf{S} \quad (3.8)$$

$$\oint \mathbf{E} \cdot d\mathbf{l} = -\frac{\partial}{\partial t} \iint \mathbf{B} \cdot d\mathbf{S} \quad (3.9)$$

$$\oiint \mathbf{D} \cdot d\mathbf{S} = \iiint \rho dV \quad (3.10)$$

$$\oiint \mathbf{B} \cdot d\mathbf{S} = 0, \quad (3.11)$$

so that the behavior of the electromagnetic fields can also be described at material interfaces where the material parameters are discontinuous in space.

TANGENTIAL COMPONENT OF \mathbf{H}

Consider (3.8) on a rectangular region that is given in Figure 3.1a with $\mathbf{r}(s)$ a parametrization for the line l . As the height of the rectangle Δh drops to zero, the integral of the derivative term vanishes. In physical media the conduction is finite and therefore also \mathbf{J} . In that case the \mathbf{J} term vanishes and

$$\begin{aligned}\oint_l \mathbf{H} \cdot d\mathbf{r} &= 0 \Leftrightarrow \\ \int_a^b \mathbf{H}_1 \cdot \frac{d\mathbf{r}}{ds} ds + \int_c^d \mathbf{H}_2 \cdot \frac{d\mathbf{r}}{ds} ds &= 0.\end{aligned}$$

If the width of the rectangle is chosen arbitrarily small, the magnetic fields are assumed to be constant in the direct surroundings of the line l and therefore

$$\begin{aligned}\mathbf{H}_1 \cdot \begin{bmatrix} -1 \\ 0 \end{bmatrix} \int_a^b ds + \mathbf{H}_2 \cdot \begin{bmatrix} 1 \\ 0 \end{bmatrix} \int_c^d ds &= 0 \Leftrightarrow \\ (\mathbf{H}_1 - \mathbf{H}_2) \cdot \begin{bmatrix} 1 \\ 0 \end{bmatrix} \Delta l &= 0 \Leftrightarrow \\ \mathbf{n} \times (\mathbf{H}_1 - \mathbf{H}_2) &= \mathbf{0}.\end{aligned}$$

This means that the tangential component of the magnetic field is continuous across the interface between different media.

TANGENTIAL COMPONENT OF \mathbf{E}

Consider (3.9) on a rectangular region that is given in Figure 3.1a. As the height of the rectangle Δh drops to zero, the integral of the derivative term again vanishes and

$$\int_a^b \mathbf{E}_1 \cdot \frac{d\mathbf{r}}{ds} ds + \int_c^d \mathbf{E}_2 \cdot \frac{d\mathbf{r}}{ds} ds = 0.$$

Also in this case the width can be chosen arbitrarily small, and therefore

$$\begin{aligned} \mathbf{E}_1 \cdot \begin{bmatrix} -1 \\ 0 \end{bmatrix} \int_a^b ds + \mathbf{E}_2 \cdot \begin{bmatrix} 1 \\ 0 \end{bmatrix} \int_c^d ds &= 0 \Leftrightarrow \\ \mathbf{n} \times (\mathbf{E}_1 - \mathbf{E}_2) &= \mathbf{0}. \end{aligned}$$

Also the tangential component of the electric field is continuous across the interface between different media.

NORMAL COMPONENT OF \mathbf{D}_c

Consider (3.10) on a cylinder with surface \mathcal{S} that is shown in Figure 3.1b, with $\mathbf{r}(u, v)$ a parametrization for the surface \mathcal{S} . The third Maxwell equation can be rewritten by differentiating both sides of the equation with respect to time and using the relation $\frac{\partial \rho}{\partial t} = -\nabla \cdot \mathbf{J}^{\text{tot}}$:

$$\begin{aligned} \frac{\partial}{\partial t} \oiint \mathbf{D} \cdot d\mathbf{S} &= \frac{\partial}{\partial t} \iiint \rho dV \Leftrightarrow \\ \oiint \mathbf{J}^{\text{tot}} \cdot d\mathbf{S} + \frac{\partial}{\partial t} \oiint \mathbf{D} \cdot d\mathbf{S} &= 0. \end{aligned} \quad (3.12)$$

Making the cylinder arbitrarily small in height, results in a vanishing integral over the curved surface and therefore (3.12) becomes

$$\begin{aligned} \oiint_{\mathcal{S}_1} \left(\mathbf{J}^{\text{tot}} + \frac{\partial \mathbf{D}}{\partial t} \right) \cdot d\mathbf{S} &= 0 \Leftrightarrow \\ \oiint_{\mathcal{S}_1} \left(\mathbf{J}^{\text{tot}} + \frac{\partial \mathbf{D}}{\partial t} \right) \cdot \left(\frac{\partial \mathbf{r}}{\partial u} \times \frac{\partial \mathbf{r}}{\partial v} \right) dudv + \oiint_{\mathcal{S}_2} \left(\mathbf{J}^{\text{tot}} + \frac{\partial \mathbf{D}}{\partial t} \right) \cdot \left(\frac{\partial \mathbf{r}}{\partial u} \times \frac{\partial \mathbf{r}}{\partial v} \right) dudv &= 0. \end{aligned}$$

If also the diameter of the cylinder is made arbitrarily small, then

$$\begin{aligned} \left(\mathbf{J}_1^{\text{tot}} + \frac{\partial \mathbf{D}_1}{\partial t} \right) \cdot \begin{bmatrix} 0 \\ 0 \\ 1 \end{bmatrix} \oiint_{\mathcal{S}_1} dudv + \left(\mathbf{J}_2^{\text{tot}} + \frac{\partial \mathbf{D}_2}{\partial t} \right) \cdot \begin{bmatrix} 0 \\ 0 \\ -1 \end{bmatrix} \oiint_{\mathcal{S}_2} dudv &= 0 \Leftrightarrow \\ \left(\left(\mathbf{J}_1^{\text{tot}} + \frac{\partial \mathbf{D}_1}{\partial t} \right) - \left(\mathbf{J}_2^{\text{tot}} + \frac{\partial \mathbf{D}_2}{\partial t} \right) \right) \cdot \mathbf{n} &= 0, \end{aligned}$$

which means that the normal component of $\mathbf{J}^{\text{tot}} + \frac{\partial \mathbf{D}}{\partial t}$ is continuous across the interface between different media.

NORMAL COMPONENT OF \mathbf{B}

Considering (3.11) on a cylinder that is shown in Figure 3.1b and applying the same integration procedure as above, a boundary condition can be derived for the magnetic flux density:

$$(\mathbf{B}_1 - \mathbf{B}_2) \cdot \mathbf{n} = 0,$$

which means that the normal component of the magnetic flux density is continuous across the interface between different media.

To summarize the findings, the boundary conditions corresponding to Maxwell's equations are given by

$$\begin{aligned} \mathbf{n} \times (\mathbf{E}_1 - \mathbf{E}_2) &= \mathbf{0} \\ \left(\left(\mathbf{J}_1 + \frac{\partial \mathbf{D}_1}{\partial t} \right) - \left(\mathbf{J}_2 + \frac{\partial \mathbf{D}_2}{\partial t} \right) \right) \cdot \mathbf{n} &= 0 \\ (\mathbf{B}_1 - \mathbf{B}_2) \cdot \mathbf{n} &= 0 \\ \mathbf{n} \times (\mathbf{H}_1 - \mathbf{H}_2) &= \mathbf{0}. \end{aligned}$$

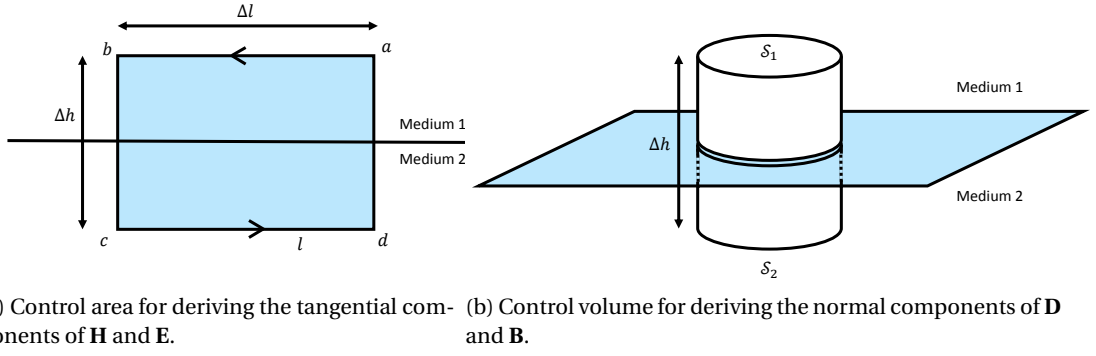


Figure 3.1

3.3. THE VOLUME INTEGRAL EQUATION

Maxwell's equations can be written in a different form: the volume integral equation (VIE). The transformation will be done for the general 3D case, from which also the 2D case can be derived. In the final form of this formulation both the unknowns \mathbf{E} and \mathbf{H} and their integrals are present, but the magnetic field \mathbf{H} has been eliminated from the equation for \mathbf{E} , so that the equations for \mathbf{E} can be solved separately from the equation for \mathbf{H} . To arrive at the volume integral formulation, consider first the Laplace transform of (3.1) and (3.2),

$$-\nabla \times \hat{\mathbf{H}} + \eta \hat{\mathbf{E}} = -\mathbf{J}^{\text{ext}} \quad (3.13)$$

$$\nabla \times \mathbf{E} + \zeta \hat{\mathbf{H}} = -\mathbf{K}^{\text{ext}}. \quad (3.14)$$

with the Laplace transform defined by

$$\hat{f}(\mathbf{x}, s) = \mathcal{L}\{f(\mathbf{x}, t)\} = \int_0^\infty f(\mathbf{x}, t) e^{-st} dt$$

and $\eta = \sigma + s\varepsilon$, $\zeta = s\mu$. The compatibility relations then transform into

$$\nabla \cdot \eta \hat{\mathbf{E}} = -\nabla \cdot \hat{\mathbf{J}}^{\text{ext}}$$

$$\nabla \cdot \zeta \hat{\mathbf{H}} = -\nabla \cdot \hat{\mathbf{K}}^{\text{ext}}.$$

Now consider (3.13) and (3.14) for the medium vacuum. In that case, $\varepsilon = \varepsilon_0$, $\mu = \mu_0$ and $\sigma = 0$. This gives the system

$$-\nabla \times \hat{\mathbf{H}} + \eta_0 \hat{\mathbf{E}} = -\hat{\mathbf{J}}^{\text{ext}} \quad (3.15)$$

$$\nabla \times \hat{\mathbf{E}} + \zeta_0 \hat{\mathbf{H}} = -\hat{\mathbf{K}}^{\text{ext}}, \quad (3.16)$$

with $\eta_0 = s\varepsilon_0$ and $\zeta_0 = s\mu_0$.

Next, a Fourier transform defined by

$$\tilde{f}(\mathbf{k}, s) = \mathcal{F}\{f(\mathbf{x}, s)\} = \int_{\mathbf{x} \in \mathbb{R}^3} f(\mathbf{x}, s) e^{i\mathbf{k} \cdot \mathbf{x}} dV,$$

transforms (3.15) and (3.16) into

$$i\mathbf{k} \times \tilde{\mathbf{H}} + \eta_0 \tilde{\mathbf{E}} = -\tilde{\mathbf{J}}^{\text{ext}} \quad (3.17)$$

$$-i\mathbf{k} \times \tilde{\mathbf{E}} + \zeta_0 \tilde{\mathbf{H}} = -\tilde{\mathbf{K}}^{\text{ext}}. \quad (3.18)$$

Note that in the last system both the time derivatives and the spatial derivatives have been eliminated. This makes it easier to find expressions for $\tilde{\mathbf{H}}$ and $\tilde{\mathbf{E}}$. (3.18) can be rewritten into

$$\tilde{\mathbf{H}} = \frac{1}{\zeta_0} (-\tilde{\mathbf{K}}^{\text{ext}} + i\mathbf{k} \times \tilde{\mathbf{E}}) \quad (3.19)$$

after which $\tilde{\mathbf{H}}$ can be eliminated from (3.17). This yields

$$((\mathbf{k}^T \mathbf{k} + \gamma_0^2) \mathbf{I} - \mathbf{k} \mathbf{k}^T) \tilde{\mathbf{E}} = -\zeta_0 \tilde{\mathbf{J}}^{\text{ext}} + \mathbf{i} \mathbf{k} \times \tilde{\mathbf{K}}^{\text{ext}} \quad (3.20)$$

where $\zeta_0 \eta_0 = \gamma_0^2$. In order to find an expression for $\tilde{\mathbf{E}}$ in terms of $\tilde{\mathbf{J}}^{\text{ext}}$ and $\tilde{\mathbf{K}}^{\text{ext}}$, (3.20) is rewritten with the help of the compatibility relations. The compatibility relations for Maxwell's equations in vacuum,

$$\eta_0 \nabla \cdot \hat{\mathbf{E}} = -\nabla \cdot \hat{\mathbf{J}}^{\text{ext}} \quad (3.21)$$

$$\zeta_0 \nabla \cdot \hat{\mathbf{H}} = -\nabla \cdot \hat{\mathbf{K}}^{\text{ext}}, \quad (3.22)$$

can be transformed into frequency domain,

$$\eta_0 \mathbf{k}^T \tilde{\mathbf{E}} = -\mathbf{k}^T \tilde{\mathbf{J}}^{\text{ext}} \quad (3.23)$$

$$\zeta_0 \mathbf{k}^T \tilde{\mathbf{H}} = -\mathbf{k}^T \tilde{\mathbf{K}}^{\text{ext}}, \quad (3.24)$$

and (3.23) turns out useful in rewriting the left hand side of (3.20) as

$$((\mathbf{k}^T \mathbf{k} + \gamma_0^2) \mathbf{I} - \mathbf{k} \mathbf{k}^T) \tilde{\mathbf{E}} = (\mathbf{k}^T \mathbf{k} + \gamma_0^2) \tilde{\mathbf{E}} + \frac{1}{\eta_0} \mathbf{k} \mathbf{k}^T \tilde{\mathbf{J}}^{\text{ext}}.$$

Now the new equation for $\tilde{\mathbf{E}}$ is given by

$$(\mathbf{k}^T \mathbf{k} + \gamma_0^2) \tilde{\mathbf{E}} + \frac{1}{\eta_0} \mathbf{k} \mathbf{k}^T \tilde{\mathbf{J}}^{\text{ext}} = -\zeta_0 \tilde{\mathbf{J}}^{\text{ext}} + \mathbf{i} \mathbf{k} \times \tilde{\mathbf{K}}^{\text{ext}}$$

from which $\tilde{\mathbf{E}}$ can be written as

$$\tilde{\mathbf{E}} = \frac{1}{\mathbf{k}^T \mathbf{k} + \gamma_0^2} \left(-(\zeta_0 \mathbf{I} + \frac{1}{\eta_0} \mathbf{k} \mathbf{k}^T) \tilde{\mathbf{J}}^{\text{ext}} + \mathbf{i} \mathbf{k} \times \tilde{\mathbf{K}}^{\text{ext}} \right). \quad (3.25)$$

Substitution of (3.25) in (3.19) gives

$$\tilde{\mathbf{H}} = \frac{1}{\mathbf{k}^T \mathbf{k} + \gamma_0^2} \left(-\left(\eta_0 \mathbf{I} + \frac{1}{\zeta_0} \mathbf{k} \mathbf{k}^T \right) \tilde{\mathbf{K}}^{\text{ext}} - \mathbf{i} \mathbf{k} \times \tilde{\mathbf{J}}^{\text{ext}} \right).$$

Now that expressions for $\tilde{\mathbf{E}}$ and $\tilde{\mathbf{H}}$ have been found, the next step is to transform the expressions back into space domain by applying the inverse Fourier transform. This is done by introducing the vector potentials $\tilde{\mathbf{A}}$ and $\tilde{\mathbf{F}}$:

$$\begin{aligned} \tilde{\mathbf{A}} &= \tilde{\mathbf{g}} \tilde{\mathbf{J}}^{\text{ext}} \\ \tilde{\mathbf{F}} &= \tilde{\mathbf{g}} \tilde{\mathbf{K}}^{\text{ext}}, \end{aligned}$$

where $\tilde{\mathbf{g}} = \frac{1}{\mathbf{k}^T \mathbf{k} + \gamma_0^2}$ is the Green's function of the Helmholtz equation. In terms of these new variables the set of equations becomes

$$\begin{aligned} \tilde{\mathbf{E}} &= -\left(\zeta_0 \mathbf{I} + \frac{1}{\eta_0} \mathbf{k} \mathbf{k}^T \right) \tilde{\mathbf{A}} + \mathbf{i} \mathbf{k} \times \tilde{\mathbf{F}} \\ \tilde{\mathbf{H}} &= -\left(\eta_0 \mathbf{I} + \frac{1}{\zeta_0} \mathbf{k} \mathbf{k}^T \right) \tilde{\mathbf{F}} - \mathbf{i} \mathbf{k} \times \tilde{\mathbf{A}} \end{aligned}$$

and in Laplace domain

$$\begin{aligned} \hat{\mathbf{E}} &= -\zeta_0 \hat{\mathbf{A}} + \frac{1}{\eta_0} \nabla (\nabla \cdot \hat{\mathbf{A}}) - \nabla \times \hat{\mathbf{F}} \\ \hat{\mathbf{H}} &= -\eta_0 \hat{\mathbf{F}} + \frac{1}{\zeta_0} \nabla (\nabla \cdot \hat{\mathbf{F}}) + \nabla \times \hat{\mathbf{A}} \end{aligned}$$

where

$$\begin{aligned} \hat{\mathbf{A}} &= \int_{\mathbf{x}' \in \mathbb{R}^3} \hat{\mathbf{g}}(\mathbf{x} - \mathbf{x}', s) \hat{\mathbf{J}}^{\text{ext}}(\mathbf{x}', s) dV' \\ \hat{\mathbf{F}} &= \int_{\mathbf{x}' \in \mathbb{R}^3} \hat{\mathbf{g}}(\mathbf{x} - \mathbf{x}', s) \hat{\mathbf{K}}^{\text{ext}}(\mathbf{x}', s) dV' \end{aligned}$$

by the convolution theorem.

The inverse Fourier transform of the Green's function for the 3D configuration is

$$\hat{g}(\mathbf{x}, \omega) = \frac{e^{-ik_b|\mathbf{x}|}}{4\pi|\mathbf{x}|}$$

and for the 2D configuration the result is

$$\hat{g}(\mathbf{x}, \omega) = -\frac{i}{4}H_0^{(2)}(k_b|\mathbf{x}|), [17],$$

where

$$k_b^2 = -\gamma_0^2.$$

The derivation for the 2D case can be found in Appendix B, where the time convention $s = \omega i$ is used.

3.4. THE SCATTERING PROBLEM

So far it was assumed that the source is surrounded by vacuum. In many cases, including the MRI problem where the human body is the object, this is not true and induced currents are produced. In order to take induced currents into account, Maxwell's equations are rewritten as

$$\begin{aligned} -\nabla \times \mathbf{H} + \varepsilon_0 \frac{\partial \mathbf{E}}{\partial t} &= -(\mathbf{J}^{\text{ind}} + \mathbf{J}^{\text{ext}}) \\ \nabla \times \mathbf{E} + \mu_0 \frac{\partial \mathbf{H}}{\partial t} &= -(\mathbf{K}^{\text{ind}} + \mathbf{K}^{\text{ext}}), \end{aligned}$$

where \mathbf{J}^{ext} and \mathbf{K}^{ext} are again the external sources and \mathbf{J}^{ind} and \mathbf{K}^{ind} are the scattering sources. With these new right hand sides of Maxwell's equations, it follows by substitution that the volume integral equations become

$$\begin{aligned} \hat{\mathbf{E}}(\mathbf{x}, s) &= -\zeta_0 \int_{\mathbf{x}' \in \mathbb{R}^3} \hat{g}(\mathbf{x} - \mathbf{x}', s) (\hat{\mathbf{J}}^{\text{ext}}(\mathbf{x}', s) + \hat{\mathbf{J}}^{\text{ind}}(\mathbf{x}', s)) dV' + \frac{1}{\eta_0} \nabla \left(\nabla \cdot \int_{\mathbf{x}' \in \mathbb{R}^3} \hat{g}(\mathbf{x} - \mathbf{x}', s) (\hat{\mathbf{J}}^{\text{ext}}(\mathbf{x}', s) + \hat{\mathbf{J}}^{\text{ind}}(\mathbf{x}', s)) dV' \right) \\ &\quad - \nabla \times \int_{\mathbf{x}' \in \mathbb{R}^3} \hat{g}(\mathbf{x} - \mathbf{x}', s) (\hat{\mathbf{K}}^{\text{ext}}(\mathbf{x}', s) + \hat{\mathbf{K}}^{\text{ind}}(\mathbf{x}', s)) dV' \end{aligned} \quad (3.26)$$

$$\begin{aligned} \hat{\mathbf{H}}(\mathbf{x}, s) &= -\eta_0 \int_{\mathbf{x}' \in \mathbb{R}^3} \hat{g}(\mathbf{x} - \mathbf{x}', s) (\hat{\mathbf{K}}^{\text{ext}}(\mathbf{x}', s) + \hat{\mathbf{K}}^{\text{ind}}(\mathbf{x}', s)) dV' + \frac{1}{\zeta_0} \nabla \left(\nabla \cdot \int_{\mathbf{x}' \in \mathbb{R}^3} \hat{g}(\mathbf{x} - \mathbf{x}', s) (\hat{\mathbf{K}}^{\text{ext}}(\mathbf{x}', s) + \hat{\mathbf{K}}^{\text{ind}}(\mathbf{x}', s)) dV' \right) \\ &\quad + \nabla \times \int_{\mathbf{x}' \in \mathbb{R}^3} \hat{g}(\mathbf{x} - \mathbf{x}', s) (\hat{\mathbf{J}}^{\text{ext}}(\mathbf{x}', s) + \hat{\mathbf{J}}^{\text{ind}}(\mathbf{x}', s)) (\mathbf{x}', s) dV'. \end{aligned} \quad (3.27)$$

There is a relation between the total fields with an object present and the electromagnetic fields in vacuum where no object is present. The difference between the two is the field radiated by the induced currents, called the scattered field. This can be written as

$$\hat{\mathbf{E}}^{\text{sc}} = \hat{\mathbf{E}} - \hat{\mathbf{E}}^{\text{inc}} \quad (3.28)$$

$$\hat{\mathbf{H}}^{\text{sc}} = \hat{\mathbf{H}} - \hat{\mathbf{H}}^{\text{inc}}, \quad (3.29)$$

where $\hat{\mathbf{E}}^{\text{inc}}$ and $\hat{\mathbf{H}}^{\text{inc}}$ are the fields in vacuum ('inc' is short for incident, 'sc' is short for scattered) and are given by

$$\begin{aligned} \hat{\mathbf{E}}^{\text{inc}}(\mathbf{x}, s) &= -\zeta_0 \int_{\mathbf{x}' \in \mathbb{R}^3} \hat{g}(\mathbf{x} - \mathbf{x}', s) \hat{\mathbf{J}}^{\text{ext}}(\mathbf{x}', s) dV' + \frac{1}{\eta_0} \nabla \left(\nabla \cdot \int_{\mathbf{x}' \in \mathbb{R}^3} \hat{g}(\mathbf{x} - \mathbf{x}', s) \hat{\mathbf{J}}^{\text{ext}}(\mathbf{x}', s) dV' \right) \\ &\quad - \nabla \times \int_{\mathbf{x}' \in \mathbb{R}^3} \hat{g}(\mathbf{x} - \mathbf{x}', s) \hat{\mathbf{K}}^{\text{ext}}(\mathbf{x}', s) dV' \end{aligned} \quad (3.30)$$

$$\begin{aligned} \hat{\mathbf{H}}^{\text{inc}}(\mathbf{x}, s) &= -\eta_0 \int_{\mathbf{x}' \in \mathbb{R}^3} \hat{g}(\mathbf{x} - \mathbf{x}', s) \hat{\mathbf{K}}^{\text{ext}}(\mathbf{x}', s) dV' + \frac{1}{\zeta_0} \nabla \left(\nabla \cdot \int_{\mathbf{x}' \in \mathbb{R}^3} \hat{g}(\mathbf{x} - \mathbf{x}', s) \hat{\mathbf{K}}^{\text{ext}}(\mathbf{x}', s) dV' \right) \\ &\quad + \nabla \times \int_{\mathbf{x}' \in \mathbb{R}^3} \hat{g}(\mathbf{x} - \mathbf{x}', s) \hat{\mathbf{J}}^{\text{ext}}(\mathbf{x}', s) dV' \end{aligned} \quad (3.31)$$

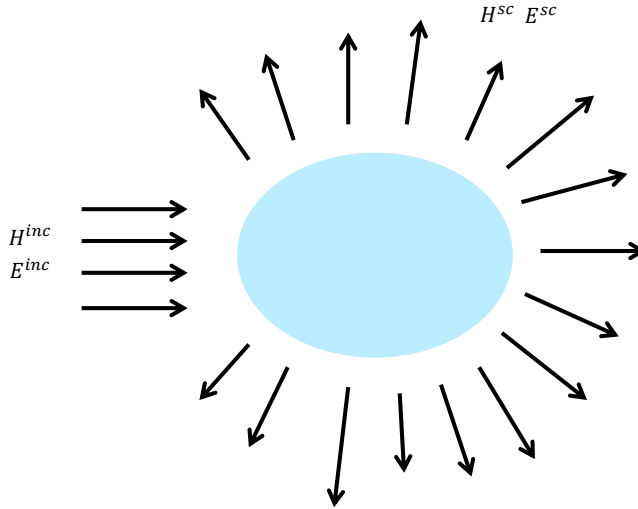


Figure 3.2: Scattering principle.

according to Maxwell's equations. The scattering principle is schematically shown in Figure 3.2. It is important to note that the incident fields are known, because they are determined by the external sources in vacuum. Subtracting (3.30) and (3.31) from (3.26) and (3.27) gives expressions for the scattered fields and these can be substituted in (3.28) and (3.29) to find

$$\begin{aligned} \hat{\mathbf{E}}^{\text{inc}}(\mathbf{x}, s) &= \hat{\mathbf{E}}(\mathbf{x}, s) + \zeta_0 \int_{\mathbf{x}' \in \mathbb{R}^3} \hat{\mathbf{g}}(\mathbf{x} - \mathbf{x}', s) \hat{\mathbf{J}}^{\text{ind}}(\mathbf{x}', s) dV' - \frac{1}{\eta_0} \nabla \left(\nabla \cdot \int_{\mathbf{x}' \in \mathbb{R}^3} \hat{\mathbf{g}}(\mathbf{x} - \mathbf{x}', s) \hat{\mathbf{J}}^{\text{ind}}(\mathbf{x}', s) dV' \right) \\ &\quad + \nabla \times \int_{\mathbf{x}' \in \mathbb{R}^3} \hat{\mathbf{g}}(\mathbf{x} - \mathbf{x}', s) \hat{\mathbf{K}}^{\text{ind}}(\mathbf{x}', s) dV' \end{aligned} \quad (3.32)$$

$$\begin{aligned} \hat{\mathbf{H}}^{\text{inc}}(\mathbf{x}, s) &= \hat{\mathbf{H}}(\mathbf{x}, s) + \eta_0 \int_{\mathbf{x}' \in \mathbb{R}^3} \hat{\mathbf{g}}(\mathbf{x} - \mathbf{x}', s) \hat{\mathbf{K}}^{\text{ind}}(\mathbf{x}', s) dV' - \frac{1}{\xi_0} \nabla \left(\nabla \cdot \int_{\mathbf{x}' \in \mathbb{R}^3} \hat{\mathbf{g}}(\mathbf{x} - \mathbf{x}', s) \hat{\mathbf{K}}^{\text{ind}}(\mathbf{x}', s) dV' \right) \\ &\quad - \nabla \times \int_{\mathbf{x}' \in \mathbb{R}^3} \hat{\mathbf{g}}(\mathbf{x} - \mathbf{x}', s) \hat{\mathbf{J}}^{\text{ind}}(\mathbf{x}', s) dV'. \end{aligned} \quad (3.33)$$

Together (3.32) and (3.33) still contain four unknowns, which makes it impossible to solve for the fields $\hat{\mathbf{E}}$ and $\hat{\mathbf{H}}$. In order to eliminate the unknowns $\hat{\mathbf{K}}^{\text{ind}}$ and $\hat{\mathbf{J}}^{\text{ind}}$ the following relations for the scattering sources are introduced:

$$\mathbf{J}^{\text{ind}} = \mathbf{J} + \frac{\partial}{\partial t} (\mathbf{D} - \varepsilon_0 \mathbf{E}) \quad (3.34)$$

$$\mathbf{K}^{\text{ind}} = \frac{\partial}{\partial t} (\mathbf{B} - \mu_0 \mathbf{H}), \quad (3.35)$$

where \mathbf{J} is the electric current density produced by freely moving charged particles. Furthermore, the constitutive relations in Laplace domain,

$$\hat{\mathbf{D}}(\mathbf{x}, s) = \varepsilon(\mathbf{x}, s) \hat{\mathbf{E}}(\mathbf{x}, s) \quad (3.36)$$

$$\hat{\mathbf{B}}(\mathbf{x}, s) = \mu(\mathbf{x}, s) \hat{\mathbf{H}}(\mathbf{x}, s) \quad (3.37)$$

$$\hat{\mathbf{J}}(\mathbf{x}, s) = \sigma(\mathbf{x}, s) \hat{\mathbf{E}}(\mathbf{x}, s), \quad (3.38)$$

turn out useful in finding expressions for $\hat{\mathbf{J}}^{\text{ind}}$ and $\hat{\mathbf{K}}^{\text{ind}}$ that depend on the unknowns $\hat{\mathbf{E}}$ and $\hat{\mathbf{H}}$ only. The result is obtained via transforming (3.34) and (3.35) into Laplace domain and substituting (3.36) - (3.38) in the result. This gives

$$\begin{aligned} \hat{\mathbf{J}}^{\text{ind}}(\mathbf{x}, s) &= (\sigma(\mathbf{x}, s) + s(\varepsilon(\mathbf{x}, s) - \varepsilon_0(\mathbf{x}, s))) \hat{\mathbf{E}}(\mathbf{x}, s) = (\eta(\mathbf{x}, s) - \eta_0(\mathbf{x}, s)) \hat{\mathbf{E}}(\mathbf{x}, s) \\ \hat{\mathbf{K}}^{\text{ind}}(\mathbf{x}, s) &= s(\mu(\mathbf{x}, s) - \mu_0(\mathbf{x}, s)) \hat{\mathbf{H}}(\mathbf{x}, s) = (\zeta(\mathbf{x}, s) - \zeta_0(\mathbf{x}, s)) \hat{\mathbf{H}}(\mathbf{x}, s). \end{aligned}$$

Finally,

$$\begin{aligned}\hat{\mathbf{E}}^{\text{inc}}(\mathbf{x}, s) &= \hat{\mathbf{E}}(\mathbf{x}, s) + \zeta_0(s)\eta_0(s) \int_{\mathbf{x}' \in \mathbb{R}^3} \hat{g}(\mathbf{x} - \mathbf{x}', s) \chi_e(\mathbf{x}', s) \hat{\mathbf{E}}(\mathbf{x}', s) dV' - \nabla \left(\nabla \cdot \int_{\mathbf{x}' \in \mathbb{R}^3} \hat{g}(\mathbf{x} - \mathbf{x}', s) \chi_e(\mathbf{x}', s) \hat{\mathbf{E}}(\mathbf{x}', s) dV' \right) \\ &\quad + \xi_0(s) \nabla \times \int_{\mathbf{x}' \in \mathbb{R}^3} \hat{g}(\mathbf{x} - \mathbf{x}', s) \chi_m(\mathbf{x}', s) \hat{\mathbf{H}}(\mathbf{x}', s) dV'\end{aligned}\quad (3.39)$$

$$\begin{aligned}\hat{\mathbf{H}}^{\text{inc}}(\mathbf{x}, s) &= \hat{\mathbf{H}}(\mathbf{x}, s) + \eta_0(s)\zeta_0(s) \int_{\mathbf{x}' \in \mathbb{R}^3} \hat{g}(\mathbf{x} - \mathbf{x}', s) \chi_m(\mathbf{x}', s) \hat{\mathbf{H}}(\mathbf{x}', s) dV' - \nabla \left(\nabla \cdot \int_{\mathbf{x}' \in \mathbb{R}^3} \hat{g}(\mathbf{x} - \mathbf{x}', s) \chi_m(\mathbf{x}', s) \hat{\mathbf{H}}(\mathbf{x}', s) dV' \right) \\ &\quad - \eta_0(s) \nabla \times \int_{\mathbf{x}' \in \mathbb{R}^3} \hat{g}(\mathbf{x} - \mathbf{x}', s) \chi_e(\mathbf{x}', s) \hat{\mathbf{E}}(\mathbf{x}', s) dV'\end{aligned}\quad (3.40)$$

where the contrast functions are defined by

$$\begin{aligned}\chi_e(\mathbf{x}, s) &= \frac{\eta(\mathbf{x}, s)}{\eta_0(s)} - 1, \\ \chi_m(\mathbf{x}, s) &= \frac{\zeta(\mathbf{x}, s)}{\zeta_0(s)} - 1.\end{aligned}$$

In the human body the magnetic contrast χ_m is zero, so in this research (3.39) and (3.40) simplify to

$$\begin{aligned}\hat{\mathbf{E}}^{\text{inc}}(\mathbf{x}, s) &= \hat{\mathbf{E}}(\mathbf{x}, s) + \zeta_0(s)\eta_0(s) \int_{\mathbf{x}' \in \mathbb{R}^3} \hat{g}(\mathbf{x} - \mathbf{x}', s) \chi_e(\mathbf{x}', s) \hat{\mathbf{E}}(\mathbf{x}', s) dV' \\ &\quad - \nabla \left(\nabla \cdot \int_{\mathbf{x}' \in \mathbb{R}^3} \hat{g}(\mathbf{x} - \mathbf{x}', s) \chi_e(\mathbf{x}', s) \hat{\mathbf{E}}(\mathbf{x}', s) dV' \right)\end{aligned}\quad (3.41)$$

$$\hat{\mathbf{H}}^{\text{inc}}(\mathbf{x}, s) = \hat{\mathbf{H}}(\mathbf{x}, s) - \eta_0(s) \nabla \times \int_{\mathbf{x}' \in \mathbb{R}^3} \hat{g}(\mathbf{x} - \mathbf{x}', s) \chi_e(\mathbf{x}', s) \hat{\mathbf{E}}(\mathbf{x}', s) dV' \quad (3.42)$$

and these last two equations form the basis of the volume integral approach.

3.4.1. DIFFERENT FORMULATIONS OF THE SCATTERING PROBLEM

In Section 3.4 (3.41) and (3.42) define two volume integral equations derived from Maxwell's equations. In this thesis only the volume integral equation for the electric field, or one of its variants, will be solved. Once a solution for the electric field has been obtained, the magnetic field can be found via substitution of the electric field in the volume integral equation for the magnetic field or in Maxwell's equations.

It is possible to rewrite the volume integral equation into equations expressed in different unknowns with the help of (3.36) - (3.38). In this research the volume integral equation for the magnetic field will not be considered, because once the electric field is known, also the magnetic field can be found by substitution. Four different formulations will be discussed here. In rewriting the formulations, the relations

$$\hat{\mathbf{D}}_c = \varepsilon_c \hat{\mathbf{E}} = \frac{\eta}{s} \hat{\mathbf{E}} = \left(\frac{\sigma}{s} + \varepsilon \right) \hat{\mathbf{E}}$$

and

$$\hat{\mathbf{J}}_c = \eta_0 \chi_e \hat{\mathbf{E}} = \sigma \hat{\mathbf{E}} + s \hat{\mathbf{E}} (\varepsilon - \varepsilon_0)$$

are introduced.

EVIE

The first formulation has already been derived in the beginning of this section, namely the EVIE (Electric Volume Integral Equation) formulation:

$$\hat{\mathbf{E}}^{\text{inc}} = \hat{\mathbf{E}} - (\mathbf{k}_b^2 + \nabla \nabla \cdot) \mathbf{S}(\chi_e \hat{\mathbf{E}}) \quad (3.43)$$

where

$$\mathbf{S}(\mathbf{J}) = \int_{\Omega} \hat{g}(\mathbf{x} - \mathbf{x}', s) \mathbf{J}(\mathbf{x}', s) dV'$$

and $\mathbf{k}_b^2 = -\zeta_0 \eta_0$. The other formulations are based on the EVIE formulation.

DVIE

Substitution of the relation $\hat{\mathbf{D}}_c = \varepsilon_c \hat{\mathbf{E}}$ in (3.43) gives the DVIE (Electric Displacement Volume Integral Equation) formulation:

$$\hat{\mathbf{E}}^{\text{inc}} = \frac{1}{\varepsilon_c} \hat{\mathbf{D}}_c - (k_b^2 + \nabla \nabla \cdot) \mathbf{S} \left(\frac{\chi_e}{\varepsilon_c} \hat{\mathbf{D}}_c \right). \quad (3.44)$$

JVIE

Substitution of the relation $\hat{\mathbf{J}}_c = \eta_0 \chi_e \hat{\mathbf{E}}$ in (3.43) gives the JVIE (Electric Current Volume Integral Equation) formulation:

$$\hat{\mathbf{E}}^{\text{inc}} = \frac{1}{\eta_0 \chi_e} \hat{\mathbf{J}}_c - \frac{1}{\eta_0} (k_b^2 + \nabla \nabla \cdot) \mathbf{S}(\hat{\mathbf{J}}_c).$$

In the last formulation a problem would occur if the contrast is zero, which is the case in the background medium vacuum. Therefore the JVIE formulation is usually formulated as

$$\eta_0 \chi_e \hat{\mathbf{E}}^{\text{inc}} = \hat{\mathbf{J}}_c - \chi_e (k_b^2 + \nabla \nabla \cdot) \mathbf{S}(\hat{\mathbf{J}}_c). \quad (3.45)$$

For the above three formulations it has been shown in [18] that they are equivalent, that a unique solution exists and that the problems are well-posed in their corresponding function spaces. Although the three formulations are very similar, they are different because of their mapping properties. In [19] and [20] it is explained that in order to derive mathematically correct numerical schemes that guarantee convergence, the mapping properties should be taken into account. In the schemes studied in this thesis the mapping properties have not been taken into account, but earlier studies have shown that also in this case satisfactory accuracy can be obtained for the MRI application.

4

THE ANALYTICAL SOLUTION OF SCATTERING ON A TWO-LAYER CONDUCTING CYLINDER

For some configurations it is possible to derive an analytical solution of the scattering problem. To be able to analyze the accuracy of the developed numerical methods in Chapter 6, an expression for such an analytical solution is derived in this chapter. Fundamentals of the derivation can be found in [21].

As configuration an infinitely long circular cylinder is chosen with the symmetry axis of the cylinder aligned with the z -axis. The cylinder is composed of two different conducting materials. The outer layer with radius a_1 has a relative permittivity of ϵ_{r1} and a conductivity of σ_1 siemens per meter and the inner layer with radius a_2 has a relative permittivity of ϵ_{r2} and a conductivity of σ_2 siemens per meter. Transverse electric (TE) polarization is studied, which means that the magnetic field only has a z -component and the electric field propagates in the x, y -plane. Figure 4.1 schematically shows the 3D view and the top view of a part of the studied configuration.

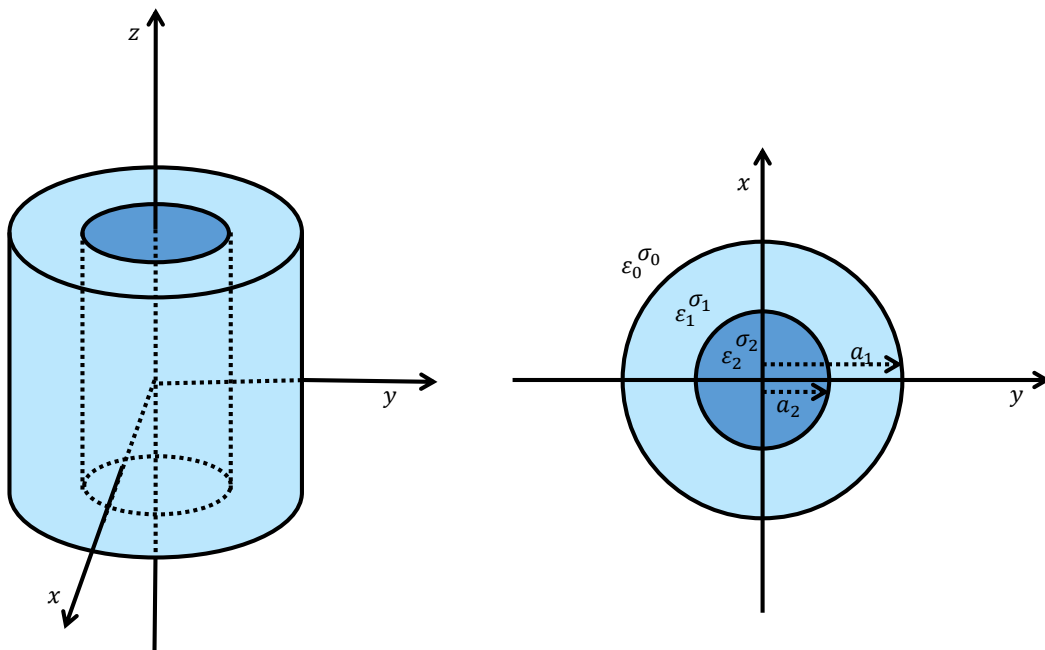


Figure 4.1: 3D and top view of a part of the infinitely long cylinder.

4.1. MAXWELL'S EQUATIONS IN CYLINDRICAL COORDINATES

The analytical solution can be found after transforming Maxwell's equations into cylindrical coordinates. Component-wise, the result is given by

$$\begin{aligned} E_\rho &= \frac{1}{\eta} \left(\frac{1}{\rho} \frac{\partial H_z}{\partial \phi} - \frac{\partial H_\phi}{\partial z} \right) \\ E_\phi &= \frac{1}{\eta} \left(\frac{\partial H_\rho}{\partial z} - \frac{\partial H_z}{\partial \rho} \right) \\ E_z &= \frac{1}{\rho \eta} \left(\frac{\partial}{\partial \rho} (\rho H_\rho) - \frac{\partial H_\rho}{\partial \phi} \right). \end{aligned}$$

and

$$\begin{aligned} H_\rho &= \frac{1}{\zeta_0} \left(\frac{1}{\rho} \frac{\partial E_z}{\partial \phi} - \frac{\partial E_\phi}{\partial z} \right) \\ H_\phi &= \frac{1}{\zeta_0} \left(\frac{\partial E_\rho}{\partial z} - \frac{\partial E_z}{\partial \rho} \right) \\ H_z &= \frac{1}{\rho \zeta_0} \left(\frac{\partial}{\partial \rho} (\rho E_\rho) - \frac{\partial E_\rho}{\partial \phi} \right). \end{aligned}$$

The fields are invariant in z -direction because the cylinder is assumed to have an infinitely long z -axis and the incident field is chosen to be invariant in z -direction as well. Therefore, Maxwell's equations in cylindrical coordinates simplify to

$$\begin{aligned} E_\rho &= \frac{1}{\rho \eta} \frac{\partial H_z}{\partial \phi} \\ E_\phi &= -\frac{1}{\eta} \frac{\partial H_z}{\partial \rho} \\ E_z &= \frac{1}{\rho \eta} \left(\frac{\partial}{\partial \rho} (\rho H_\phi) - \frac{\partial H_\rho}{\partial \phi} \right) \end{aligned}$$

and

$$\begin{aligned} H_\rho &= \frac{1}{\rho \zeta_0} \frac{\partial E_z}{\partial \phi} \\ H_\phi &= -\frac{1}{\zeta_0} \frac{\partial E_z}{\partial \rho} \\ H_z &= \frac{1}{\rho \zeta_0} \left(\frac{\partial}{\partial \rho} (\rho E_\phi) - \frac{\partial E_\rho}{\partial \phi} \right). \end{aligned}$$

In this set of equations, E_z, H_ϕ and H_ρ have been decoupled from H_z, E_ϕ and E_ρ . If the electric field is invariant in z -direction, then the corresponding waves are said to be H -polarized or TE-polarized. If the magnetic field is invariant in z -direction, then the waves are said to be E -polarized or TH-polarized. In this thesis the volume integral equation for the electric field, with the important $\nabla \cdot$ operator, is the equation of interest. Both polarization types can be studied with this equation, but for the H -polarized case 2D equations are sufficient and the full effect of the $\nabla \cdot$ operator can be taken into account. Therefore, H -polarization is studied and the equations describing the scattering problem are

$$E_\rho = \frac{1}{\rho \eta} \frac{\partial H_z}{\partial \phi} \quad (4.1)$$

$$E_\phi = -\frac{1}{\eta} \frac{\partial H_z}{\partial \rho} \quad (4.2)$$

$$H_z = \frac{1}{\rho \zeta_0} \left(\frac{\partial}{\partial \rho} (\rho E_\phi) - \frac{\partial E_\rho}{\partial \phi} \right). \quad (4.3)$$

4.2. THE GENERAL SOLUTION

The general solution of (4.1) - (4.3) can be found via separation of variables. The equation of interest is

$$\rho^2 \frac{\partial^2 H_z}{\partial \rho^2} + \rho \frac{\partial H_z}{\partial \rho} + \frac{\partial^2 H_z}{\partial \phi^2} + \rho^2 \zeta_0 \eta H_z = 0, \quad (4.4)$$

which can be found by substituting (4.1) and (4.2) in (4.3). Substitution of $H_z(\rho, \phi) = A(\rho)B(\phi)$ in (4.4) gives the two uncoupled second order differential equations

$$\frac{\partial^2 B}{\partial \phi^2} + k^2 B = 0 \quad (4.5)$$

and

$$\rho^2 \frac{\partial^2 A}{\partial \rho^2} + \rho \frac{\partial A}{\partial \rho} + (\rho^2 \zeta_0 \eta - k^2) A = 0. \quad (4.6)$$

The characteristic equation corresponding with (4.5) has roots ki and $-ki$, so the solution is given by $B(\phi) = B_k e^{ik\phi}$ with B_k constant and k integer because of the 2π -periodicity condition for H_z . (4.6) requires the additional transformation $\rho \sqrt{\zeta_0 \eta} = z$, so that

$$z^2 \frac{\partial^2 A(z)}{\partial z^2} + z \frac{\partial A(z)}{\partial z} + (z^2 - k^2) A(z) = 0$$

can be recognized as Bessel's differential equation with general solution

$$A(z) = C_k J_k(z) + D_k Y_k(z) \quad \text{or} \quad A(z) = E_k H_k^{(1)}(z) + F_k H_k^{(2)}(z),$$

in which $H_k^{(1)}$ and $H_k^{(2)}$ are k -th integer order Hankel functions of the first and second kind respectively, and J_k and Y_k are k -th integer order Bessel functions of the first and second kind respectively. Finally, the principle of superposition gives the general solution of Maxwell's equations:

$$H_z(\rho, \phi) = \sum_{k=1}^{\infty} A(z) e^{ik\phi}. \quad (4.7)$$

4.3. SCATTERING ON A TWO-LAYER CONDUCTING CIRCULAR CYLINDER

With (4.7) in mind the magnetic field in each layer of the cylinder (shown in Figure 4.1) can be expanded according to the physical properties of propagation of the waves in each part of the cylinder. For this it is important to know that with the time convention $s = \omega i$, Hankel functions of the first kind represent incoming waves, Hankel functions of the second kind represent outgoing waves and Bessel functions represent standing waves. More information on wave representation can be found in [21] and [22].

As starting point a plane wave incident field traveling in the x -direction is chosen. It was explained in [22] that plane waves can be expanded using Bessel functions. An object disturbs the incident wave by inducing an additional outgoing wave. The scattered field is therefore written as a sum of Hankel functions of the second kind. The standing wave in the first layer of the cylinder is disturbed by an additional outgoing wave resulting from the scattering of the inner layer of the cylinder. Since Hankel functions and thus outgoing waves can be represented in terms of Bessel functions of the first and second kind, the field inside the first layer of the cylinder is expanded as a sum of Bessel functions of the first kind and Bessel functions of the second kind. The field in the inner layer of the cylinder is again totally reflected in the origin, and therefore remains a standing wave. Summarized,

$$H_z^i = H_0 \sum_{k=-\infty}^{\infty} i^{-k} J_k(\beta_0 \rho) e^{ik\phi} \quad (4.8)$$

$$H_z^s = H_0 \sum_{k=-\infty}^{\infty} a_k H_k^{(2)}(\beta_0 \rho) e^{ik\phi} \quad (4.9)$$

$$H_z^d = H_0 \sum_{k=-\infty}^{\infty} [b_k J_k(\beta_1 \rho) + c_k Y_k(\beta_1 \rho)] e^{ik\phi} \quad (4.10)$$

$$H_z^f = H_0 \sum_{k=-\infty}^{\infty} d_k J_k(\beta_2 \rho) e^{ik\phi}, \quad (4.11)$$

where the sum of H_z^i and H_z^s is the total magnetic field outside the cylinder, H_z^d is the magnetic field in the outer layer of the cylinder and H_z^f is the magnetic field in the inner layer of the cylinder. Furthermore, $H_0 = -\sqrt{\frac{\varepsilon_0}{\mu_0}}$ is a chosen constant so that the electric incident field has amplitude 1. The wave numbers in the different layers of the cylinder are defined as

$$\begin{aligned}\beta_0 &= k_b = s\sqrt{-\mu_0\varepsilon_0} \\ \beta_1 &= s\sqrt{-\mu_0\varepsilon_0\left(\varepsilon_{r_1} + \frac{\sigma_1}{s\varepsilon_0}\right)} \\ \beta_2 &= s\sqrt{-\mu_0\varepsilon_0\left(\varepsilon_{r_2} + \frac{\sigma_2}{s\varepsilon_0}\right)}.\end{aligned}$$

Note that the magnetic field in the inner layer of the cylinder is only expanded with Bessel functions of the first kind, because Bessel functions of the second kind have a singularity at the origin.

Substituting (4.8) in (4.1) and in (4.2) gives

$$\begin{aligned}E_\phi^i &= -\frac{H_0\beta_0}{\eta_0} \sum_{k=-\infty}^{\infty} i^{-k} J'_k(\beta_0\rho) e^{ik\phi} \\ E_\rho^i &= \frac{H_0}{\eta_0\rho} \sum_{k=-\infty}^{\infty} i^{-k} J_k(\beta_0\rho) e^{ik\phi} ik.\end{aligned}$$

Substituting (4.9) in (4.1) and in (4.2) gives

$$\begin{aligned}E_\phi^s &= -\frac{H_0\beta_0}{\eta_0} \sum_{k=-\infty}^{\infty} a_k H_k^{(2)}(\beta_0\rho) e^{ik\phi} \\ E_\rho^s &= \frac{H_0}{\eta_0\rho} \sum_{k=-\infty}^{\infty} a_k H_k^{(2)}(\beta_0\rho) e^{ik\phi} ik.\end{aligned}$$

Substituting (4.10) in (4.1) and in (4.2) gives

$$\begin{aligned}E_\phi^d &= -\frac{H_0\beta_1}{\eta_1} \sum_{k=-\infty}^{\infty} [b_k J'_k(\beta_1\rho) + c_k Y'_k(\beta_1\rho)] e^{ik\phi} \\ E_\rho^d &= \frac{H_0}{\eta_1\rho} \sum_{k=-\infty}^{\infty} [b_k J_k(\beta_1\rho) + c_k Y_k(\beta_1\rho)] e^{ik\phi} ik\end{aligned}$$

and substituting (4.11) in (4.1) and in (4.2) gives

$$\begin{aligned}E_\phi^f &= -\frac{H_0\beta_2}{\eta_2} \sum_{k=-\infty}^{\infty} d_k J'_k(\beta_2\rho) e^{ik\phi} \\ E_\rho^f &= \frac{H_0}{\eta_2\rho} \sum_{k=-\infty}^{\infty} d_k J_k(\beta_2\rho) e^{ik\phi} ik.\end{aligned}$$

The unknown coefficients can be determined by enforcing the material boundary conditions. Since the considered configuration is a perfect cylinder in the x, y, z -plane aligned along the z -axis, the tangential components correspond with the ϕ - and the z -component and therefore continuity in tangential components can be obtained via requiring that

$$\begin{aligned}\lim_{\rho \uparrow a_1} (H_z^i(\phi, \rho) + H_z^s(\phi, \rho)) &= \lim_{\rho \uparrow a_1} H_z^d(\phi, \rho) \\ \lim_{\rho \downarrow a_2} H_z^d(\phi, \rho) &= \lim_{\rho \downarrow a_2} H_z^f(\phi, \rho)\end{aligned}$$

and

$$\begin{aligned}\lim_{\rho \uparrow a_1} (E_\phi^i(\phi, \rho) + E_\phi^s(\phi, \rho)) &= \lim_{\rho \uparrow a_1} E_\phi^d(\phi, \rho) \\ \lim_{\rho \downarrow a_2} E_\phi^d(\phi, \rho) &= \lim_{\rho \downarrow a_2} E_\phi^f(\phi, \rho).\end{aligned}$$

These equations translate to

$$i^{-k} J_k(\beta_0 a_1) + a_k H_k^{(2)}(\beta_0 a_1) = b_k J_k(\beta_1 a_1) + c_k Y_k(\beta_1 a_1) \quad (4.12)$$

$$b_k J_k(\beta_1 a_2) + c_k Y_k(\beta_1 a_2) = d_k J_k(\beta_2 a_2) \quad (4.13)$$

and

$$-\frac{\beta_0}{\eta_0} \left(i^{-k} J'_k(\beta_0 a_1) + a_k H_k^{(2)'}(\beta_0 a_1) \right) = -\frac{\beta_1}{\eta_1} (b_k J'_k(\beta_1 a_1) + c_k Y'_k(\beta_1 a_1)) \quad (4.14)$$

$$-\frac{\beta_1}{\eta_1} (b_k J'_k(\beta_1 a_2) + c_k Y'_k(\beta_1 a_2)) = -\frac{\beta_2}{\eta_2} d_k J'_k(\beta_2 a_2), \quad (4.15)$$

where the orthogonality property of the complex exponential function has been used. Together (4.12) - (4.15) form the system

$$\begin{bmatrix} H_k^{(2)}(\beta_0 a_1) & -J_k(\beta_1 a_1) & -Y_k(\beta_1 a_1) & 0 \\ 0 & J_k(\beta_1 a_2) & Y_k(\beta_1 a_2) & -J_k(\beta_2 a_2) \\ -\frac{\beta_0}{\eta_0} H_k^{(2)'}(\beta_0 a_1) & \frac{\beta_1}{\eta_1} J'_k(\beta_1 a_1) & \frac{\beta_1}{\eta_1} Y'_k(\beta_1 a_1) & 0 \\ 0 & -\frac{\beta_1}{\eta_1} J'_k(\beta_1 a_2) & -\frac{\beta_1}{\eta_1} Y'_k(\beta_1 a_2) & \frac{\beta_2}{\eta_2} J'_k(\beta_2 a_2) \end{bmatrix} \begin{bmatrix} a_k \\ b_k \\ c_k \\ d_k \end{bmatrix} = \begin{bmatrix} -i^{-k} J_k(\beta_0 a_1) \\ 0 \\ \frac{\beta_0}{\eta_0} i^{-k} J'_k(\beta_0 a_1) \\ 0 \end{bmatrix}$$

from which a_k, b_k, c_k and d_k can be solved for each $k \in \mathbb{Z}$.

5

THE METHOD OF MOMENTS

For the majority of the configurations it is not possible to derive an analytical solution. These cases require numerical simulations to find solutions of the scattering problem. As was discussed earlier, different starting points of Maxwell's equations correspond with different numerical techniques. In Section 3.3 the volume integral form was derived, which is the starting point for the method of moments. In high frequency fields the method of moments is not applicable, because a high frequency means a small wavelength with respect to the object and therefore impractically fine grids are unavoidable. For small frequencies, however, a small number of grid nodes is sufficient to model the scattering problem. MRI is an application that works with small frequencies (100 MHz - 300 MHz) and therefore the method of moments has become popular. The preference for this method is explained by the fact that the Sommerfeld radiation condition is automatically satisfied. This means that one does not have to deal with absorbing boundary conditions like in the finite element method (FEM) or in the finite difference time domain (FDTD) method to obtain a unique solution. The steps in the method of moments are similar to the ones in the finite element method. The first step is deriving the weak form of the volume integral equation. Once the weak form is obtained, the discretization procedure begins by approximating the unknown by a sum of basis functions multiplied with unknown coefficients. These coefficients are the ones that need to be solved from the final system. To be able to do so, basis functions are chosen in such a way that they span the solution space and that the coefficients are easy to obtain. Two choices of test functions are commonly used. One results in Galerkin's method and the other one in the point collocation method. Both of these methods will be described in this chapter and the first method forms the basis for the final models derived in Chapter 6. From this point on, the method will be explained for the 2D case because TE polarization is studied.

5.1. WEAK FORM

Remember that the volume integral equation can be compactly written as

$$\hat{\mathbf{E}}^{\text{inc}} = \hat{\mathbf{E}} - (\mathbf{k}_b^2 + \nabla\nabla\cdot)\mathbf{S}(\chi_e\hat{\mathbf{E}}). \quad (5.1)$$

In the 2D case (5.1) is a system of two coupled equations, where the electric field $\hat{\mathbf{E}}$ is a two-dimensional vectorial unknown. Therefore two weak forms are derived, one for each component. By doing this, both the x -component and the y -component of the electric field can be expanded with (possibly) different basis functions and different coefficients in the next step. In order to derive the weak forms, the system is written in separate equations for the two components:

$$E_x^{\text{inc}} = E_x - k_b^2 S(\chi_e E_x) - \frac{\partial}{\partial x} \left(\frac{\partial}{\partial x} S(\chi_e E_x) + \frac{\partial}{\partial y} S(\chi_e E_y) \right) \quad (5.2)$$

$$E_y^{\text{inc}} = E_y - k_b^2 S(\chi_e E_y) - \frac{\partial}{\partial y} \left(\frac{\partial}{\partial x} S(\chi_e E_x) + \frac{\partial}{\partial y} S(\chi_e E_y) \right) \quad (5.3)$$

where

$$S(J_\alpha) = \int_{\Omega} \hat{\mathbf{g}}(\mathbf{x} - \mathbf{x}', \omega) J_\alpha(\mathbf{x}', \omega) dV'.$$

Multiplication of (5.2) and (5.3) by test functions η_x and η_y respectively and integrating over the domain of interest Ω , gives

$$\int_{\Omega} E_x^{\text{inc}} \eta_x d\Omega = \int_{\Omega} \hat{E}_x \eta_x d\Omega - k_b^2 \int_{\Omega} S(\chi_e \hat{E}_x) \eta_x d\Omega - \int_{\Omega} \frac{\partial}{\partial x} (\nabla \cdot \mathbf{S}(\chi_e \hat{\mathbf{E}})) \eta_x d\Omega \quad (5.4)$$

$$\int_{\Omega} E_y^{\text{inc}} \eta_y d\Omega = \int_{\Omega} \hat{E}_y \eta_y d\Omega - k_b^2 \int_{\Omega} S(\chi_e \hat{E}_y) \eta_y d\Omega - \int_{\Omega} \frac{\partial}{\partial y} (\nabla \cdot \mathbf{S}(\chi_e \hat{\mathbf{E}})) \eta_y d\Omega. \quad (5.5)$$

Partial integrating and using Green's theorem, transforms the weak formulations (5.4) and (5.5) into

$$\int_{\Omega} E_x^{\text{inc}} \eta_x d\Omega = \int_{\Omega} E_x \eta_x d\Omega - k_b^2 \int_{\Omega} S(\chi_e E_x) \eta_x d\Omega + \int_{\Omega} \nabla \cdot \mathbf{S}(\chi_e \hat{\mathbf{E}}) \frac{\partial}{\partial x} \eta_x d\Omega - \int_{\partial\Omega} \nabla \cdot \mathbf{S}(\chi_e \hat{\mathbf{E}}) \eta_x n_x d\Gamma \quad (5.6)$$

$$\int_{\Omega} E_y^{\text{inc}} \eta_y d\Omega = \int_{\Omega} E_y \eta_y d\Omega - k_b^2 \int_{\Omega} S(\chi_e E_y) \eta_y d\Omega + \int_{\Omega} \nabla \cdot \mathbf{S}(\chi_e \hat{\mathbf{E}}) \frac{\partial}{\partial y} \eta_y d\Omega - \int_{\partial\Omega} \nabla \cdot \mathbf{S}(\chi_e \hat{\mathbf{E}}) \eta_y n_y d\Gamma, \quad (5.7)$$

where n_x and n_y are the components of the normal vector on the boundary of the domain. Both weak formulations can be used to discretize the system. The advantage of the second weak form is that one spatial derivative now acts on the test function and is easy to calculate. Moreover, the first derivative of the Green's function contains a singularity that is weaker than the singularity of the second derivative of the Green's function.

5.2. DISCRETIZATION

Now that the weak forms are known, the volume integral equation can be transformed into a discretized system of equations. This can be done in several ways. The first possibility is approximating the unknowns E_x and E_y by series

$$E_x^n(\mathbf{x}) = \sum_{j=1}^n e_{j,x} \phi_{j,x}(\mathbf{x}) \quad \text{and} \quad E_y^n(\mathbf{x}) = \sum_{j=1}^n e_{j,y} \phi_{j,y}(\mathbf{x})$$

that converge to E_x and E_y as $n \rightarrow \infty$. The second possibility is to expand not only the unknown electric field, but also the vector potential $\mathbf{S}(\chi_e \hat{\mathbf{E}})$ that operates on the unknown electric field. Additional substitutions

$$S_x^n(\mathbf{x}) = S^n(\chi_e E_x)(\mathbf{x}) = \sum_{j=1}^n s_{j,x} \phi_{j,x}(\mathbf{x}) \quad \text{and} \quad S_y^n(\mathbf{x}) = S^n(\chi_e E_y)(\mathbf{x}) = \sum_{j=1}^n s_{j,y} \phi_{j,y}(\mathbf{x})$$

are carried out in this case. The incident field can be expanded in the same way.

The first possibility, substitution of E_x^n and E_y^n in (5.6) and (5.7) respectively, results in

$$\begin{aligned} \sum_{j=1}^n e_{j,x}^{\text{inc}} \int_{\Omega} \phi_{j,x} \eta_{i,x} d\Omega &= \sum_{j=1}^n e_{j,x} \left\{ \int_{\Omega} \phi_{j,x} \eta_{i,x} d\Omega - k_b^2 \int_{\Omega} S(\chi_e \phi_{j,x}) \eta_{i,x} d\Omega \right. \\ &\quad \left. + \int_{\Omega} \frac{\partial}{\partial x} S(\chi_e \phi_{j,x}) \frac{\partial}{\partial x} \eta_{i,x} d\Omega - \int_{\partial\Omega} \eta_{i,x} \frac{\partial}{\partial x} S(\chi_e \phi_{j,x}) n_x d\Gamma \right\} \\ &\quad + \sum_{j=1}^n e_{j,y} \left\{ \int_{\Omega} \frac{\partial}{\partial y} S(\chi_e \phi_{j,y}) \frac{\partial}{\partial x} \eta_{i,x} d\Omega - \int_{\partial\Omega} \eta_{i,x} \frac{\partial}{\partial y} S(\chi_e \phi_{j,y}) n_x d\Gamma \right\} \quad i = 1, \dots, n \\ \sum_{j=1}^n e_{j,y}^{\text{inc}} \int_{\Omega} \phi_{j,y} \eta_{i,y} d\Omega &= \sum_{j=1}^n e_{j,x} \left\{ \int_{\Omega} \frac{\partial}{\partial x} S(\chi_e \phi_{j,x}) \frac{\partial}{\partial y} \eta_{i,y} d\Omega - \int_{\partial\Omega} \eta_{i,y} \frac{\partial}{\partial x} S(\chi_e \phi_{j,x}) n_y d\Gamma \right\} \\ &\quad + \sum_{j=1}^n e_{j,y} \left\{ \int_{\Omega} \phi_{j,y} \eta_{i,y} d\Omega - k_b^2 \int_{\Omega} S(\chi_e \phi_{j,y}) \eta_{i,y} d\Omega \right. \\ &\quad \left. + \int_{\Omega} \frac{\partial}{\partial y} S(\chi_e \phi_{j,y}) \frac{\partial}{\partial y} \eta_{i,y} d\Omega - \int_{\partial\Omega} \eta_{i,y} \frac{\partial}{\partial y} S(\chi_e \phi_{j,y}) n_y d\Gamma \right\} \quad i = 1, \dots, n. \end{aligned}$$

The second possibility, substitution of E_x^n , E_y^n , $S^n(\chi_e E_x)$ and $S^n(\chi_e E_y)$ in (5.6) and (5.7) results in

$$\begin{aligned} \sum_{j=1}^n e_{j,x}^{\text{inc}} \int_{\Omega} \phi_{j,x} \eta_{i,x} d\Omega &= \sum_{j=1}^n e_{j,x} \left\{ \int_{\Omega} \phi_{j,x} \eta_{i,x} d\Omega \right\} \\ &+ \sum_{j=1}^n s_{j,x} \left\{ -k_b^2 \int_{\Omega} \phi_{j,x} \eta_{i,x} d\Omega + \int_{\Omega} \frac{\partial}{\partial x} \phi_{j,x} \frac{\partial}{\partial x} \eta_{i,x} d\Omega - \int_{\partial\Omega} \eta_{i,x} \frac{\partial}{\partial x} \phi_{j,x} n_x d\Gamma \right\} \\ &+ \sum_{j=1}^n s_{j,y} \left\{ \int_{\Omega} \frac{\partial}{\partial y} \phi_{j,y} \frac{\partial}{\partial x} \eta_{i,x} d\Omega - \int_{\partial\Omega} \eta_{i,x} \frac{\partial}{\partial y} \phi_{j,y} n_x d\Gamma \right\} \quad i = 1, \dots, n \end{aligned} \quad (5.8)$$

$$\begin{aligned} \sum_{j=1}^n e_{j,y}^{\text{inc}} \int_{\Omega} \phi_{j,y} \eta_{i,y} d\Omega &= \sum_{j=1}^n e_{j,y} \left\{ \int_{\Omega} \phi_{j,y} \eta_{i,y} d\Omega \right\} \\ &+ \sum_{j=1}^n s_{j,x} \left\{ \int_{\Omega} \frac{\partial}{\partial x} \phi_{j,x} \frac{\partial}{\partial y} \eta_{i,y} d\Omega - \int_{\partial\Omega} \eta_{i,y} \frac{\partial}{\partial x} \phi_{j,x} n_y d\Gamma \right\} \quad i = 1, \dots, n \\ &+ \sum_{j=1}^n s_{j,y} \left\{ -k_b^2 \int_{\Omega} \phi_{j,y} \eta_{i,y} d\Omega + \int_{\Omega} \frac{\partial}{\partial y} \phi_{j,y} \frac{\partial}{\partial y} \eta_{i,y} d\Omega - \int_{\partial\Omega} \eta_{i,y} \frac{\partial}{\partial y} \phi_{j,y} n_y d\Gamma \right\} \end{aligned} \quad (5.9)$$

The coefficients $e_{j,x}$ and $s_{j,x}$ are related, just like the coefficients $e_{j,y}$ and $s_{j,y}$, via

$$\sum_{j=1}^n s_{j,\alpha} \phi_{j,\alpha}(\mathbf{x}) = S^n(\chi_e E_\alpha)(\mathbf{x}) \approx \int_{x'} \hat{g}(\mathbf{x} - \mathbf{x}') \chi_e(\mathbf{x}') E_\alpha(\mathbf{x}') dV' \approx \int_{x'} \hat{g}(\mathbf{x} - \mathbf{x}') \chi_e(\mathbf{x}') \sum_{j=1}^n e_{j,\alpha} \phi_{j,\alpha}(\mathbf{x}') dV'. \quad (5.10)$$

In some approaches where both the electric field and the vector potential have been expanded, one can make use of the fact that the vector potential is a convolution of the Green's function and the product of the contrast function and the electric field. The result of a convolution can be calculated with fast Fourier transforms (FFT). The big advantage is that the Green's function only has to be calculated in all the grid nodes once instead of in all possible combinations of differences between two grid points, as one would expect. This technique will be used later in Chapter 6.

After both the expansion procedures the resulting equations can generally be written as a system of size $2n \times 2n$, and of the form

$$\begin{bmatrix} A^a & A^b \\ A^c & A^d \end{bmatrix} \begin{bmatrix} \mathbf{e}^a \\ \mathbf{e}^b \end{bmatrix} = \begin{bmatrix} \mathbf{f}^a \\ \mathbf{f}^b \end{bmatrix} \quad (5.11)$$

where the elements of the subvectors \mathbf{e}^a and \mathbf{e}^b are defined by

$$\begin{aligned} e_j^a &= e_{j,x} & j &= 1, \dots, n \\ e_j^b &= e_{j,y} & j &= 1, \dots, n \end{aligned}$$

and the elements of the subvectors \mathbf{f}^a and \mathbf{f}^b by

$$\begin{aligned} f_i^a &= \int_{\Omega} \phi_{j,x} \eta_{i,x} d\Omega & i &= 1, \dots, n \\ f_i^b &= \int_{\Omega} \phi_{j,y} \eta_{i,y} d\Omega & i &= 1, \dots, n. \end{aligned}$$

The elements of the submatrices A^a , A^b , A^c and A^d depend on the choice of basis and test functions.

5.3. CHOICE OF TEST FUNCTIONS

In order to continue the discretization procedure test functions need to be chosen. There are numerous possibilities to choose the test functions. When constructing them, it is useful to keep in mind the type of function that needs to be approximated. A continuous function can be approximated with continuous or discontinuous test functions. A discontinuous function, however, is in general better approximated with discontinuous test functions. Overall, two choices of test functions are popular and result in different techniques: the point collocation method and Galerkin's method. Below both of the methods will be demonstrated.

5.3.1. GALERKIN'S METHOD

In Galerkin's method the test functions are chosen to be the same as the basis functions, so $\eta_x = \phi_{i,x}$ and $\eta_y = \phi_{i,y}$ for $i = 1, \dots, n$. The resulting equations

$$\begin{aligned} \sum_{j=1}^n e_{j,x}^{\text{inc}} \int_{\Omega} \phi_{j,x} \eta_{i,x} d\Omega &= \sum_{j=1}^n e_{j,x} \left\{ \int_{\Omega} \phi_{j,x} \phi_{i,x} d\Omega - k_b^2 \int_{\Omega} S(\chi_e \phi_{j,x}) \phi_{i,x} d\Omega + \int_{\Omega} \frac{\partial}{\partial x} S(\chi_e \phi_{j,x}) \frac{\partial}{\partial x} \phi_{i,x} d\Omega \right. \\ &\quad \left. - \int_{\partial\Omega} \frac{\partial}{\partial x} S(\chi_e \phi_{j,x}) \phi_{i,x} n_x d\Gamma \right\} \\ &\quad + \sum_{j=1}^n e_{j,y} \left\{ \int_{\Omega} \frac{\partial}{\partial y} S(\chi_e \phi_{j,y}) \frac{\partial}{\partial x} \phi_{i,x} d\Omega - \int_{\partial\Omega} \frac{\partial}{\partial y} S(\chi_e \phi_{j,y}) \phi_{i,x} n_x d\Gamma \right\}, \quad i = 1, \dots, n \\ \sum_{j=1}^n e_{j,y}^{\text{inc}} \int_{\Omega} \phi_{j,y} \eta_{i,y} d\Omega &= \sum_{j=1}^n e_{j,y} \left\{ \int_{\Omega} \phi_{j,y} \phi_{i,y} d\Omega - k_b^2 \int_{\Omega} S(\chi_e \phi_{j,y}) \phi_{i,y} d\Omega + \int_{\Omega} \frac{\partial}{\partial y} S(\chi_e \phi_{j,y}) \frac{\partial}{\partial y} \phi_{i,y} d\Omega \right. \\ &\quad \left. - \int_{\partial\Omega} \frac{\partial}{\partial y} S(\chi_e \phi_{j,y}) \phi_{i,y} n_y d\Gamma \right\} \\ &\quad + \sum_{j=1}^n e_{j,x} \left\{ \int_{\Omega} \frac{\partial}{\partial x} S(\chi_e \phi_{j,x}) \frac{\partial}{\partial y} \phi_{i,y} d\Omega - \int_{\partial\Omega} \frac{\partial}{\partial x} S(\chi_e \phi_{j,x}) \phi_{i,y} n_y d\Gamma \right\}, \quad i = 1, \dots, n. \end{aligned}$$

define the system in which the submatrices A^a, A^b, A^c and A^d in (5.11) are defined by

$$\begin{aligned} A_{ij}^a &= \int_{\Omega} \phi_{j,x} \phi_{i,x} d\Omega - k_b^2 \int_{\Omega} S(\chi_e \phi_{j,x}) \phi_{i,x} d\Omega + \int_{\Omega} \frac{\partial}{\partial x} S(\chi_e \phi_{j,x}) \frac{\partial}{\partial x} \phi_{i,x} d\Omega - \int_{\partial\Omega} \frac{\partial}{\partial x} S(\chi_e \phi_{j,x}) \phi_{i,x} n_x d\Gamma & i, j = 1, \dots, n \\ A_{ij}^b &= \int_{\Omega} \frac{\partial}{\partial y} S(\chi_e \phi_{j,y}) \frac{\partial}{\partial x} \phi_{i,x} d\Omega - \int_{\partial\Omega} \frac{\partial}{\partial y} S(\chi_e \phi_{j,y}) \phi_{i,x} n_x d\Gamma & i, j = 1, \dots, n \\ A_{ij}^c &= \int_{\Omega} \frac{\partial}{\partial x} S(\chi_e \phi_{j,x}) \frac{\partial}{\partial y} \phi_{i,y} d\Omega - \int_{\partial\Omega} \frac{\partial}{\partial x} S(\chi_e \phi_{j,x}) \phi_{i,y} n_y d\Gamma & i, j = 1, \dots, n \\ A_{ij}^d &= \int_{\Omega} \phi_{j,y} \phi_{i,y} d\Omega - k_b^2 \int_{\Omega} S(\chi_e \phi_{j,y}) \phi_{i,y} d\Omega + \int_{\Omega} \frac{\partial}{\partial y} S(\chi_e \phi_{j,y}) \frac{\partial}{\partial y} \phi_{i,y} d\Omega - \int_{\partial\Omega} \frac{\partial}{\partial y} S(\chi_e \phi_{j,y}) \phi_{i,y} n_y d\Gamma & i, j = 1, \dots, n. \end{aligned}$$

5.3.2. POINT COLLOCATION METHOD

In the point collocation method the test functions are chosen to be the Dirac delta functions, $\eta_{x,i} = \delta(x - x_i)$ for $i = 1, \dots, n$. This means that the weak form that was used in Galerkin's method would give problems here, because the derivative of the Dirac delta function would appear in the formulation. Therefore (5.4) and (5.5) are used to demonstrate the point collocation method. In this case the equations

$$\begin{aligned} e_{i,x}^{\text{inc}} &= \sum_{j=1}^n e_{j,x} \left\{ \phi_{j,x}(\mathbf{x}_i) - k_b^2 S(\chi_e \phi_{j,x})(\mathbf{x}_i) - \frac{\partial}{\partial x} \frac{\partial}{\partial x} S(\chi_e \phi_{j,x})(\mathbf{x}_i) \right\} \\ &\quad - \sum_{j=1}^n e_{j,y} \left\{ \frac{\partial}{\partial x} \frac{\partial}{\partial y} S(\chi_e \phi_{j,y})(\mathbf{x}_i) \right\} \quad i = 1, \dots, n \\ e_{i,y}^{\text{inc}} &= \sum_{j=1}^n e_{j,y} \left\{ \phi_{j,y}(\mathbf{x}_i) - k_b^2 S(\chi_e \phi_{j,y})(\mathbf{x}_i) - \frac{\partial}{\partial y} \frac{\partial}{\partial y} S(\chi_e \phi_{j,y})(\mathbf{x}_i) \right\} \\ &\quad - \sum_{j=1}^n e_{j,x} \left\{ \frac{\partial}{\partial y} \frac{\partial}{\partial x} S(\chi_e \phi_{j,x})(\mathbf{x}_i) \right\} \quad i = 1, \dots, n \end{aligned}$$

define the system in which the submatrices A^a, A^b, A^c and A^d in (5.11) are defined by

$$\begin{aligned} A_{ij}^a &= \phi_{j,x}(\mathbf{x}_i) - k_b^2 S(\chi_e \phi_{j,x})(\mathbf{x}_i) - \frac{\partial}{\partial x} \frac{\partial}{\partial x} S(\chi_e \phi_{j,x})(\mathbf{x}_i) & i, j = 1, \dots, n \\ A_{ij}^b &= -\frac{\partial}{\partial x} \frac{\partial}{\partial y} S(\chi_e \phi_{j,y})(\mathbf{x}_i) & i, j = 1, \dots, n \\ A_{ij}^c &= -\frac{\partial}{\partial y} \frac{\partial}{\partial x} S(\chi_e \phi_{j,x})(\mathbf{x}_i) & i, j = 1, \dots, n \\ A_{ij}^d &= \phi_{j,y}(\mathbf{x}_i) - k_b^2 S(\chi_e \phi_{j,y})(\mathbf{x}_i) - \frac{\partial}{\partial y} \frac{\partial}{\partial y} S(\chi_e \phi_{j,y})(\mathbf{x}_i) & i, j = 1, \dots, n. \end{aligned}$$

The choice of test functions makes the integral over the domain of the test functions disappear. This is computationally more efficient than Galerkin's method, where the integration over the domain of the test function often results in matrices that connect neighboring elements. However, a drawback of the point collocation

method is that the test function does not take into account the boundary conditions that were described in Section 3.2, whereas in Galerkin's method it is possible to choose the test and basis functions so that they do take into account the boundary conditions. For this reason, and to be able to compare with existing schemes, Galerkin's method will be chosen as discretization method in the rest of this thesis.

5.4. CHOICE OF BASIS FUNCTIONS

Ideally the basis functions are chosen such that they have the same continuity behavior as the unknown function that they represent. This implies that the basis functions are smooth enough to satisfy the differential operators in the weak formulation. There are, however, more factors that have to be taken into account. The basis functions live on a certain mesh, and the combination of the mesh and the basis function affects the computation time of the scattering problem. Moreover, it is desirable that the resulting integrals in the method of moments are relatively easy to evaluate.

A frequently used combination is the combination of piecewise linear basis functions and a triangular mesh with grid nodes located at the three vertices of each triangle. This option can be extended to 3D with a tetrahedral mesh instead of a triangular mesh. Other possibilities are piecewise constant basis functions on square cells or cubic voxels and vertices located at cell or voxel centers. More advanced functions are the so-called Schaubert-Wilton-Glisson (SWG) basis functions. [23]

6

MODEL

In the previous chapter the steps in the method of moments were discussed. Within these steps there is a lot of freedom in finalizing an optimal method for solving the scattering problem. First of all, a mesh needs to be chosen. Second, test functions and basis functions need to be defined. In this chapter one type of basis and test functions is chosen and two types of meshes are studied. These choices result in three different models,

- EVIE model on a non-staggered grid
- DVIE model on a non-staggered grid
- DVIE model on a staggered grid,

that will be derived in this chapter. At the end of this chapter variations on those models are derived by adjusting the numerical scheme for the mixed derivative terms in (5.4) and (5.5).

6.1. MESH

Two different mesh types are studied. The first mesh has square-shaped cells with grid nodes located in the cell centers. The second mesh also uses square-shaped cells, but the grid nodes correspond with a staggered grid and are located on the cell boundaries. In this case the x -directional grid nodes and the y -directional grid nodes have been shifted from each other. The result of this shift in grid nodes is found in the terms where the x -component and the y -component of the basis and test functions interact. The size of both meshes is defined by the number of cells in x -direction (M) and the number of cells in y -direction (N). In order to be able to approximate the derivatives at the boundaries of the domain, the mesh is extended with one surrounding row of cells so that the final grid has size $(M + 2) \times (N + 2)$.

The introduction of a staggered grid involves some additional actions compared with the non-staggered grid. First of all, the incident field has to be approximated on the staggered grid instead of on the non-staggered grid. Second, in order to evaluate the vector potential, the contrast has to be transformed from the non-staggered grid to the staggered grid. This is done via interpolation:

$$\chi_{e,m,n}^x \approx \frac{\chi_{e,m+\frac{1}{2},n} + \chi_{e,m-\frac{1}{2},n}}{2} \quad \text{and} \quad \chi_{e,m,n}^y \approx \frac{\chi_{e,m,n+\frac{1}{2}} + \chi_{e,m,n-\frac{1}{2}}}{2}.$$

Furthermore, in order to transform the approximated electric displacement current from the staggered grid back to the non-staggered grid, the same interpolation rule is used for the electric displacement:

$$D_{c,m,n}^x \approx \frac{D_{c,m+\frac{1}{2},n} + D_{c,m-\frac{1}{2},n}}{2} \quad \text{and} \quad D_{c,m,n}^y \approx \frac{D_{c,m,n+\frac{1}{2}} + D_{c,m,n-\frac{1}{2}}}{2}.$$

After this, the electric fields are derived from the electric displacement currents by dividing by the complex permittivity. One could also choose to first derive the electric fields on the staggered grid by dividing the electric displacement on the staggered grid by the complex permittivity on the staggered grid, and subsequently

transforming the result back to the non-staggered grid. The reason why the first option is preferred is explained by the fact that the electric displacement is approximated with continuous functions in the direction of interpolation, whereas the electric field satisfies the reverse boundary conditions and is supposed to be continuous over material interfaces in the opposite direction.

6.2. ROOFTOP BASIS AND TEST FUNCTIONS

Galerkin's discretization technique is used, which means that the test functions are chosen the same as the basis functions. Basis functions $\phi_{m,n}$ and test functions $\phi_{p,q}$ will be defined on each node.

It is important to note that in (5.8) a first derivative with respect to the x -direction acts on the x -directional basis function and on the x -directional test function. A first derivative with respect to the y -direction acts on the y -directional basis function and on the y -directional test function. The same holds for (5.9). For this reason, the basis functions for the x -component should be piecewise differentiable with respect to x and the basis functions for the y -component should be piecewise differentiable with respect to y . Basis functions that satisfy this condition are

$$\phi_{m,n}^x(\mathbf{x}) = \Lambda_m(x)\Pi_n(y)$$

for the x component and

$$\phi_{m,n}^y(\mathbf{x}) = \Pi_n(x)\Lambda_m(y)$$

for the y component, where

$$\Lambda_m(x) = \begin{cases} 1 - \frac{1}{\Delta x}|x - x_m| & |x - x_m| \leq \Delta x \\ 0 & |x - x_m| > \Delta x \end{cases}$$

and

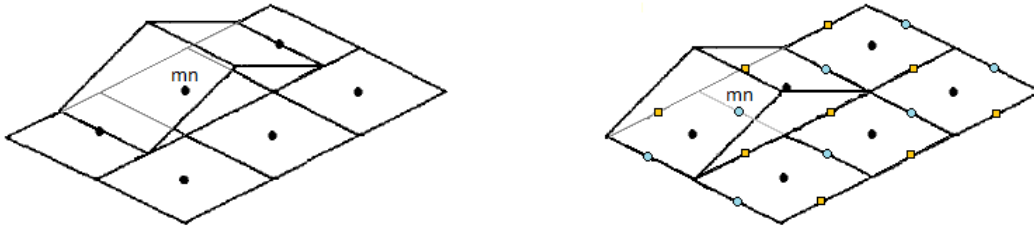
$$\Pi_n(y) = \begin{cases} 1 & y_{n-\frac{1}{2}} < y < y_{n+\frac{1}{2}} \\ \frac{1}{2} & y = y_{n-\frac{1}{2}} \vee y = y_{n+\frac{1}{2}} \\ 0 & y > y_{n-\frac{1}{2}} \vee y > y_{n+\frac{1}{2}} \end{cases}$$

Furthermore, in order to eliminate the integral over the boundary of the domain, it is preferable to position the basis functions in such a way that the test functions for the internal nodes vanish on the boundary of the domain. However, to be able to fully eliminate the boundary integral the integrand of the boundary integral should also vanish on the boundary for the boundary nodes. The divergence of the vector potential \mathbf{S} does not satisfy a homogeneous Dirichlet boundary condition in general and therefore in theory there is a contribution of the boundary nodes. However, in previous work and therefore also in this work, the contribution of the boundary term is neglected. It should be noted that the implicitly used Dirichlet boundary condition for the divergence of the vector potential will introduce errors on the boundaries of the domain. Also, boundary conditions for the fields and fluxes are needed to properly perform the weighting procedure for all nodes. Homogeneous Dirichlet boundary conditions are chosen for the electric field $\hat{\mathbf{E}}$ and for the complex electric displacement $\hat{\mathbf{D}}_c$.

Figure 6.1a schematically shows the behavior of the basis function corresponding to node m, n . Figure 6.1b schematically shows the behavior of the basis function corresponding to node m, n for a staggered grid. The y -directional basis function is shown with as blue nodes the y -directional grid nodes.

This particular choice of basis functions takes into account the material boundary conditions in the following way. The y -nodes are located on edges of cells on which the normal vector points in y -direction. A continuous basis function is used in y -direction to approximate the y -component of the field, so the normal component of the electric displacement is approximated with continuous functions. The x -nodes are located on edges of cells on which the tangential component points in y -direction as well. A discontinuous basis function is used in x -direction to approximate the y -component of the field, so the tangential component is approximated with discontinuous functions.

For the x -directional field the normal components on cell boundaries point in x -direction, and in x -direction a continuous function is used to approximate the x -component. The tangential component in x -direction is measured in the y -nodes, which are approximated with a discontinuous function.



(a) Rooftop basis function corresponding to node m, n on a non-staggered grid. (b) Rooftop basis function corresponding to node m, n on a staggered grid.

Figure 6.1: Basis functions on a staggered and on a non-staggered grid.

6.3. THE EVIE MODEL

The EVIE model solves

$$\hat{\mathbf{E}}^{\text{inc}} = \hat{\mathbf{E}} - (\mathbf{k}_b^2 + \nabla \nabla \cdot) \mathbf{S}(\chi_e \hat{\mathbf{E}}) \quad (6.1)$$

via expanding the fields and the vector potential as

$$\begin{aligned} E_\alpha &\approx \sum_{m=1}^M \sum_{n=1}^N e_{m,n}^\alpha \phi_{m,n}^\alpha, \\ S_\alpha &\approx \sum_{m=1}^M \sum_{n=1}^N s_{m,n}^\alpha \phi_{m,n}^\alpha, \\ E_\alpha^{\text{inc}} &\approx \sum_{m=1}^M \sum_{n=1}^N e_{m,n}^{\text{inc},\alpha} \phi_{m,n}^\alpha. \end{aligned}$$

Next to expanding the electric field and the vector potential, also the electric incident field is expanded. In case of a simple incident field and simple test functions one could also choose for analytically calculating the weighting on the incident field without expanding it. However, the incident field usually is a smooth function on which the weighting procedure would not have much effect, so either option works.

X-COMPONENT

Substitution of the basis functions and the test functions in the weak form for the x -component, gives

$$\begin{aligned} &\sum_{m=1}^M \sum_{n=1}^N e_{m,n}^x \left\{ \int_{\Omega} \Lambda_m(x) \Pi_n(y) \Lambda_p(x) \Pi_q(y) d\Omega \right\} - \\ &\sum_{m=1}^M \sum_{n=1}^N s_{m,n}^x \left\{ \int_{\Omega} k_b^2 \Lambda_m(x) \Pi_n(y) \Lambda_p(x) \Pi_q(y) d\Omega - \int_{\Omega} \frac{\partial}{\partial x} [\Lambda_m(x) \Pi_n(y)] \frac{\partial}{\partial x} [\Lambda_p(x) \Pi_q(y)] d\Omega \right\} + \\ &\sum_{m=1}^M \sum_{n=1}^N s_{m,n}^y \left\{ \int_{\Omega} \frac{\partial}{\partial y} [\Pi_m(x) \Lambda_n(y)] \frac{\partial}{\partial x} [\Lambda_p(x) \Pi_q(y)] d\Omega \right\} = \\ &\sum_{m=1}^M \sum_{n=1}^N e_{m,n}^{\text{inc},x} \left\{ \int_{\Omega} \Lambda_m(x) \Pi_n(y) \Lambda_p(x) \Pi_q(y) d\Omega \right\} \quad (6.2) \end{aligned}$$

for $p = 1, \dots, M$ and $q = 1, \dots, N$ with M the number of nodes in x -direction and N the number of nodes in y -direction. Each of the integrals can be evaluated making use of the fact that all integrands can be written as a product of functions of x and functions of y .

$$\begin{aligned} \int_{\Omega} \Lambda_m(x) \Pi_n(y) \Lambda_p(x) \Pi_q(y) d\Omega &= \int_x \Lambda_m(x) \Lambda_p(x) dx \int_y \Pi_n(y) \Pi_q(y) dy \\ &= \delta_{n,q} \Delta y \int_x \Lambda_m(x) \Lambda_p(x) dx \\ &= \frac{1}{6} \delta_{n,q} \Delta x \Delta y (\delta_{m,p-1} + 4\delta_{m,p} + \delta_{m,p+1}) \quad (6.3) \end{aligned}$$

$$\int_{\Omega} k_b^2 \Lambda_m(x) \Pi_n(y) \Lambda_p(x) \Pi_q(y) d\Omega = \frac{1}{6} k_b^2 \delta_{n,q} \Delta x \Delta y (\delta_{m,p-1} + 4\delta_{m,p} + \delta_{m,p+1}) \quad (6.4)$$

$$\begin{aligned} \int_{\Omega} \frac{\partial}{\partial y} [\Pi_m(x) \Lambda_n(y)] \frac{\partial}{\partial x} [\Lambda_p(x) \Pi_q(y)] d\Omega &= \int_x \left[\frac{\partial}{\partial x} \Lambda_p(x) \right] \Pi_m(x) dx \int_y \left[\frac{\partial}{\partial y} \Lambda_n(y) \right] \Pi_q(y) dy \\ &= -\frac{1}{2} (\delta_{m,p+1} - \delta_{m,p-1}) \frac{1}{2} (\delta_{n,q+1} - \delta_{n,q-1}) \end{aligned} \quad (6.5)$$

$$\begin{aligned} \int_{\Omega} \frac{\partial}{\partial x} [\Lambda_m(x) \Pi_n(y)] \frac{\partial}{\partial x} [\Lambda_p(x) \Pi_q(y)] d\Omega &= \int_x \frac{\partial}{\partial x} \Lambda_m(x) \frac{\partial}{\partial x} \Lambda_p(x) dx \int_y \Pi_n(y) \Pi_q(y) dy \\ &= -\delta_{n,q} \frac{1}{\Delta x} \Delta y (\delta_{m,p-1} - 2\delta_{m,p} + \delta_{m,p+1}) \end{aligned} \quad (6.6)$$

Substitution of (6.3), (6.4), (6.5) and (6.6) in (6.2) and deviding by $\Delta x \Delta y$ finally gives

$$\begin{aligned} \frac{1}{6} (e_{p-1,q}^x + 4e_{p,q}^x + e_{p+1,q}^x) - \frac{1}{6} k_b^2 (s_{p-1,q}^x + 4s_{p,q}^x + s_{p+1,q}^x) - \frac{1}{\Delta x^2} (s_{p-1,q}^x - 2s_{p,q}^x + s_{p+1,q}^x) \\ - \frac{1}{4\Delta x \Delta y} (s_{p+1,q+1}^y - s_{p-1,q+1}^y - s_{p+1,q-1}^y + s_{p-1,q-1}^y) = \frac{1}{6} (e_{p-1,q}^{\text{inc},x} + 4e_{p,q}^{\text{inc},x} + e_{p+1,q}^{\text{inc},x}) \end{aligned} \quad (6.7)$$

for $p = 1, \dots, M$ and $q = 1, \dots, N$.

Y-COMPONENT

Substitution of the basis functions and the test functions in the weak form for the y -component, gives

$$\begin{aligned} \sum_{m=1}^M \sum_{n=1}^N e_{m,n}^y \left\{ \int_{\Omega} \Pi_m(x) \Lambda_n(y) \Pi_p(x) \Lambda_q(y) d\Omega \right\} - \\ \sum_{m=1}^M \sum_{n=1}^N s_{m,n}^y \left\{ \int_{\Omega} k_b^2 \Pi_m(x) \Lambda_n(y) \Pi_p(x) \Lambda_q(y) d\Omega - \int_{\Omega} \frac{\partial}{\partial y} [\Pi_m(x) \Lambda_n(y)] \frac{\partial}{\partial y} [\Pi_p(x) \Lambda_q(y)] d\Omega \right\} + \\ \sum_{m=1}^M \sum_{n=1}^N s_{m,n}^x \left\{ \int_{\Omega} \frac{\partial}{\partial x} [\Lambda_m(x) \Pi_n(y)] \frac{\partial}{\partial y} [\Pi_p(x) \Lambda_q(y)] d\Omega \right\} = \\ \sum_{m=1}^M \sum_{n=1}^N e_{m,n}^{\text{inc},y} \left\{ \int_{\Omega} \Pi_m(x) \Lambda_n(y) \Pi_p(x) \Lambda_q(y) d\Omega \right\} \end{aligned} \quad (6.8)$$

for $p = 1, \dots, M$ and $q = 1, \dots, N$ with M the number of nodes in x -direction and N the number of nodes in y -direction. The integrals can be calculated in the same way as for the x -component. The results are given by

$$\int_{\Omega} \Pi_m(x) \Lambda_n(y) \Pi_p(x) \Lambda_q(y) d\Omega = \frac{1}{6} \delta_{m,p} \Delta x \Delta y (\delta_{n,q-1} + 4\delta_{n,q} + \delta_{n,q+1}) \quad (6.9)$$

$$\int_{\Omega} k_b^2 \Pi_m(x) \Lambda_n(y) \Pi_p(x) \Lambda_q(y) d\Omega = \frac{1}{6} k_b^2 \delta_{m,p} \Delta x \Delta y (\delta_{n,q-1} + 4\delta_{n,q} + \delta_{n,q+1}) \quad (6.10)$$

$$\int_{\Omega} \frac{\partial}{\partial x} [\Lambda_m(x) \Pi_n(y)] \frac{\partial}{\partial y} [\Pi_p(x) \Lambda_q(y)] d\Omega = -\frac{1}{2} (\delta_{m,p+1} - \delta_{m,p-1}) \frac{1}{2} (\delta_{n,q+1} - \delta_{n,q-1}) \quad (6.11)$$

$$\int_{\Omega} \frac{\partial}{\partial y} [\Pi_m(x) \Lambda_n(y)] \frac{\partial}{\partial y} [\Pi_p(x) \Lambda_q(y)] d\Omega = -\delta_{m,p} \Delta x \frac{1}{\Delta y} (\delta_{n,q-1} - 2\delta_{n,q} + \delta_{n,q+1}). \quad (6.12)$$

Substitution of (6.9), (6.10), (6.11) and (6.12) in (6.8) and deviding by $\Delta x \Delta y$ gives

$$\begin{aligned} \frac{1}{6} (e_{p,q-1}^y + 4e_{p,q}^y + e_{p,q+1}^y) - \frac{1}{6} k_b^2 (s_{p,q-1}^y + 4s_{p,q}^y + s_{p,q+1}^y) - \frac{1}{\Delta y^2} (s_{p,q-1}^y - 2s_{p,q}^y + s_{p,q+1}^y) \\ - \frac{1}{4\Delta x \Delta y} (s_{p+1,q+1}^x - s_{p-1,q+1}^x - s_{p+1,q-1}^x + s_{p-1,q-1}^x) = \frac{1}{6} (e_{p,q-1}^{\text{inc},y} + 4e_{p,q}^{\text{inc},y} + e_{p,q+1}^{\text{inc},y}) \end{aligned} \quad (6.13)$$

for $p = 1, \dots, M$ and $q = 1, \dots, N$.

Next, (6.7) and (6.13) can be written as a system like (5.11), but of reduced size because the expressions only depend on the number of test functions and not on the number of the basis functions. In this model the complete system can be calculated quickly by defining central difference matrices. The result is

$$\begin{aligned} B_N E^x R_N^T - k_b^2 B_N S^x R_N^T - L_{xx} S^x R_N^T - L_x S^y L_y &= B_N E^{\text{inc},x} R_N^T \\ R_M E^y B_M^T - k_b^2 R_M S^y B_M^T - R_M S^y L_y^T - L_x S^x L_y &= R_M E^{\text{inc},y} B_M^T \end{aligned}$$

where

$$B_M^{(M \times M+2)} = \frac{1}{6} \begin{bmatrix} 1 & 4 & 1 & & & \\ & \ddots & \ddots & \ddots & & \\ & & 0 & \ddots & \ddots & \\ & & & & 1 & 4 & 1 \\ & & & & & & & & & & \end{bmatrix} \quad \text{and} \quad B_N^{(N \times N+2)} = \frac{1}{6} \begin{bmatrix} 1 & 4 & 1 & & & \\ & \ddots & \ddots & \ddots & & \\ & & 0 & \ddots & \ddots & \\ & & & & 1 & 4 & 1 \\ & & & & & & & & & & \end{bmatrix}.$$

The finite difference matrices are written as

$$\begin{aligned} L_{xx}^{(M \times M+2)} &= \frac{1}{\Delta x^2} \begin{bmatrix} 1 & -2 & 1 & & & \\ & \ddots & \ddots & \ddots & & \\ & & 0 & \ddots & \ddots & \\ & & & & 1 & -2 & 1 \\ & & & & & & & & & & \end{bmatrix} \quad \text{and} \quad L_{yy}^{(N \times N+2)} = \frac{1}{\Delta y^2} \begin{bmatrix} 1 & -2 & 1 & & & \\ & \ddots & \ddots & \ddots & & \\ & & 0 & \ddots & \ddots & \\ & & & & 1 & -2 & 1 \\ & & & & & & & & & & \end{bmatrix}, \\ L_x^{(M \times M+2)} &= \frac{1}{2\Delta x} \begin{bmatrix} -1 & 0 & 1 & & & \\ & \ddots & \ddots & \ddots & & \\ & & 0 & \ddots & \ddots & \\ & & & & -1 & 0 & 1 \\ & & & & & & & & & & \end{bmatrix} \quad \text{and} \quad L_y^{(N \times N+2)} = \frac{1}{2\Delta y} \begin{bmatrix} -1 & 0 & 1 & & & \\ & \ddots & \ddots & \ddots & & \\ & & 0 & \ddots & \ddots & \\ & & & & -1 & 0 & 1 \\ & & & & & & & & & & \end{bmatrix}. \end{aligned}$$

Finally, the matrices

$$R_M^{(M \times M+2)} = \begin{bmatrix} 0 & 1 & & & 0 \\ \vdots & & \ddots & & \vdots \\ \vdots & & & 0 & \vdots \\ \vdots & & & & \vdots \\ 0 & & & & 1 & 0 \end{bmatrix} \quad \text{and} \quad R_N^{(N \times N+2)} = \begin{bmatrix} 0 & 1 & & & 0 \\ \vdots & & \ddots & & \vdots \\ \vdots & & & 0 & \vdots \\ \vdots & & & & \vdots \\ 0 & & & & 1 & 0 \end{bmatrix}$$

strip the first and the last row or column of matrices respectively.

The matrices S^x and S^y are constructed in a couple of steps. First note that (6.1) consists of three layered equations:

- $\hat{\mathbf{E}}^{\text{inc}} = \hat{\mathbf{E}} - (k_b^2 + \nabla \nabla \cdot) \mathbf{S}(\hat{\mathbf{J}})$
- $\mathbf{S}(\hat{\mathbf{J}}) = \int_{\mathbf{x}'} \hat{g}(\mathbf{x} - \mathbf{x}') \hat{\mathbf{J}} d\mathbf{x}'$
- $\hat{\mathbf{J}} = \chi_e \hat{\mathbf{E}}$.

In the first equation $\hat{\mathbf{E}}$, $\hat{\mathbf{E}}^{\text{inc}}$ and $\mathbf{S}(\hat{\mathbf{J}})$ are all expanded in rooftop basis functions. In the second equation, $\mathbf{S}(\hat{\mathbf{J}})$ and $\hat{\mathbf{J}}$ are both expanded in pulse times pulse basis functions so that the vector potential is eventually approximated following the midpoint rule. In the third equation, $\hat{\mathbf{J}}$ and $\hat{\mathbf{E}}$ are also both expanded in pulse times pulse basis functions. After applying the weighting procedure to $\hat{\mathbf{J}} = \chi_e \hat{\mathbf{E}}$, the coefficients j_{mn}^α can be determined and used to find the coefficients s_{mn}^α .

$$\begin{aligned} S(J_\alpha)(\mathbf{x}) &= \int_{\mathbf{x}'} \hat{g}(\mathbf{x} - \mathbf{x}') J_\alpha(\mathbf{x}') d\mathbf{x}' \\ &= \int_{\mathbf{x}'} \hat{g}(\mathbf{x} - \mathbf{x}') \sum_{m=1}^M \sum_{n=1}^N j_{m,n} \Pi_m(x') \Pi_n(y') d\mathbf{x}' \\ &= \sum_{m=1}^M \sum_{n=1}^N j_{m,n} \hat{g}(\mathbf{x} - \mathbf{x}_{m,n}) \Delta x \Delta y \end{aligned} \tag{6.14}$$

and

$$\begin{aligned}
\int_{\Omega} \sum_k \sum_l s_{kl} \Pi_k(x) \Pi_l(y) \Pi_p(x) \Pi_q(y) d\Omega &= \int_{\Omega} \sum_m \sum_n j_{m,n}^{\alpha} \hat{\mathbf{g}}(\mathbf{x} - \mathbf{x}_{m,n}) \Delta x \Delta y \Pi_p(x) \Pi_q(y) d\Omega \Leftrightarrow \\
\sum_k \sum_l s_{k,l} \delta_{k,p} \delta_{l,q} \Delta x \Delta y &= \sum_m \sum_n j_{m,n}^{\alpha} \Delta x \Delta y \int_{\Omega} \hat{\mathbf{g}}(\mathbf{x} - \mathbf{x}_{m,n}) \Pi_p(x) \Pi_q(y) d\Omega \Rightarrow \\
s_{p,q} &\approx \sum_m \sum_n j_{m,n}^{\alpha} \hat{\mathbf{g}}(\mathbf{x}_{p,q} - \mathbf{x}_{m,n}) \Delta x \Delta y. \tag{6.15}
\end{aligned}$$

Furthermore, the weighting procedure applied to $\hat{\mathbf{J}} = \chi_e \hat{\mathbf{E}}$ determines the coefficients $j_{m,n}^{\alpha}$. It follows that

$$\begin{aligned}
\int_{\Omega} \sum_m \sum_n j_{m,n}^{\alpha} \Pi_m(x) \Pi_n(y) \Pi_p(x) \Pi_q(y) d\Omega &= \int_{\Omega} \chi_e \sum_m \sum_n e_{m,n}^{\alpha} \Pi_m(x) \Pi_n(y) \Pi_p(x) \Pi_q(y) d\Omega \Leftrightarrow \\
j_{p,q}^{\alpha} \Delta x \Delta y &= \sum_m \sum_n e_{m,n}^{\alpha} \int_{\Omega} \chi_e \Pi_m(x) \Pi_n(y) \Pi_p(x) \Pi_q(y) d\Omega \Rightarrow \\
j_{p,q}^{\alpha} &\approx \chi_{e,p,q} e_{p,q}^{\alpha} \tag{6.16}
\end{aligned}$$

where in the last step the contrast function is assumed to be constant within each voxel.

Substituting (6.16) in (6.15) gives the final expression for the coefficients of the matrices S^x and S^y . The first possibility is to compute each coefficient separately by evaluating (6.15) for each node p, q . The second possibility is to recognise a convolution in (6.14) and compute the result with fast fourier transforms (FFT). In practise the second option will always be used, because it reduces the computation time considerably.

6.4. THE DVIE MODEL

The DVIE model solves

$$\hat{\mathbf{E}}^{\text{inc}} = \frac{1}{\varepsilon_c} \hat{\mathbf{D}}_c - (\mathbf{k}_b^2 + \nabla \nabla \cdot) \mathbf{S} \left(\frac{\chi_e}{\varepsilon_c} \hat{\mathbf{D}}_c \right) \tag{6.17}$$

via expanding the fields and the vector potential as

$$\begin{aligned}
D_{c,\alpha} &\approx \varepsilon_0 \sum_{m=1}^M \sum_{n=1}^N d_{m,n}^{\alpha} \phi_{m,n}^{\alpha}, \\
S_{\alpha} &\approx \sum_{m=1}^M \sum_{n=1}^N s_{m,n}^{\alpha} \phi_{m,n}^{\alpha}, \\
E_{\alpha}^{\text{inc}} &\approx \sum_{m=1}^M \sum_{n=1}^N e_{m,n}^{\text{inc},\alpha} \phi_{m,n}^{\alpha}.
\end{aligned}$$

X-COMPONENT

Substitution of the basis functions and the test functions in the weak form for the x -component, gives

$$\begin{aligned}
&\sum_{m=1}^M \sum_{n=1}^N d_{m,n}^x \left\{ \int_{\Omega} \frac{\varepsilon_0}{\varepsilon_c(x,y)} \Lambda_m(x) \Pi_n(y) \Lambda_p(x) \Pi_q(y) d\Omega \right\} - \\
&\sum_{m=1}^M \sum_{n=1}^N s_{m,n}^x \left\{ \int_{\Omega} k_b^2 \Lambda_m(x) \Pi_n(y) \Lambda_p(x) \Pi_q(y) d\Omega - \int_{\Omega} \frac{\partial}{\partial x} [\Lambda_m(x) \Pi_n(y)] \frac{\partial}{\partial x} [\Lambda_p(x) \Pi_q(y)] d\Omega \right\} + \\
&\sum_{m=1}^M \sum_{n=1}^N s_{m,n}^y \left\{ \int_{\Omega} \frac{\partial}{\partial y} [\Pi_m(x) \Lambda_n(y)] \frac{\partial}{\partial x} [\Lambda_p(x) \Pi_q(y)] d\Omega \right\} = \\
&\sum_{m=1}^M \sum_{n=1}^N e_{m,n}^{\text{inc},x} \left\{ \int_{\Omega} \Lambda_m(x) \Pi_n(y) \Lambda_p(x) \Pi_q(y) d\Omega \right\} \tag{6.18}
\end{aligned}$$

for $p = 1, \dots, M$ and $q = 1, \dots, N$.

Following the same procedure as in the derivation of the EVIE discretized model, the volume integrals in (6.18) can be calculated analytically. Only the first integral gives a difference in the final discretized equation:

$$\begin{aligned}
& \int_{\Omega} \frac{\varepsilon_0}{\varepsilon_c(x,y)} \Lambda_m(x) \Pi_n(y) \Lambda_p(x) \Pi_q(y) d\Omega = \varepsilon_0 \int_x \Lambda_m(x) \Lambda_p(x) \int_y \frac{1}{\varepsilon_c(x,y)} \Pi_n(y) \Pi_q(y) dy dx \\
& = \delta_{n,q} \Delta y \varepsilon_0 \int_x \frac{1}{\varepsilon_c(x,y_q)} \Lambda_m(x) \Lambda_p(x) dx \\
& = \frac{1}{12} \delta_{n,q} \Delta x \Delta y \varepsilon_0 \left(\delta_{m,p-1} \left(\frac{1}{\varepsilon_{c,m,n}} + \frac{1}{\varepsilon_{c,m+1,n}} \right) + \frac{1}{2} \delta_{m,p} \left(\frac{1}{\varepsilon_{c,m-1,n}} + \frac{14}{\varepsilon_{c,m,n}} + \frac{1}{\varepsilon_{c,m+1,n}} \right) + \delta_{m,p+1} \left(\frac{1}{\varepsilon_{c,m-1,n}} + \frac{1}{\varepsilon_{c,m,n}} \right) \right).
\end{aligned}$$

With this result the discretized equation for the x -component becomes

$$\begin{aligned}
& \frac{1}{12} \varepsilon_0 \left(\left(\frac{1}{\varepsilon_{c,p-1,q}} + \frac{1}{\varepsilon_{c,p,q}} \right) d_{p-1,q}^x + \frac{1}{2} \left(\frac{1}{\varepsilon_{c,p-1,q}} + \frac{14}{\varepsilon_{c,p,q}} + \frac{1}{\varepsilon_{c,p+1,q}} \right) d_{p,q}^x + \left(\frac{1}{\varepsilon_{c,p,q}} + \frac{1}{\varepsilon_{c,p+1,q}} \right) d_{p+1,q}^x \right) - \\
& \frac{1}{6} k_b^2 \left(s_{p-1,q}^x + 4s_{p,q}^x + s_{p+1,q}^x \right) - \frac{1}{\Delta x^2} \left(s_{p-1,q}^x - 2s_{p,q}^x + s_{p+1,q}^x \right) - \frac{1}{4\Delta x \Delta y} \left(s_{p+1,q+1}^y - s_{p-1,q+1}^y - s_{p+1,q-1}^y + s_{p-1,q-1}^y \right) = \\
& \frac{1}{6} \left(e_{p-1,q}^{\text{inc},x} + 4e_{p,q}^{\text{inc},x} + e_{p+1,q}^{\text{inc},x} \right)
\end{aligned}$$

for $p = 1, \dots, M$ and $q = 1, \dots, N$. The coefficients for the vectorpotentials $s_{m,n}^\alpha$ are now related to the unknown coefficients $d_{m,n}^\alpha$ in a different way from how the coefficients $s_{m,n}^\alpha$ are related to the unknown coefficients $e_{m,n}^\alpha$. The result will be given at the end of this section.

Y-COMPONENT

Substitution of the basis functions and the test functions in the weak form for the y -component, gives

$$\begin{aligned}
& \sum_{m=1}^M \sum_{n=1}^N d_{m,n}^y \left\{ \int_{\Omega} \frac{\varepsilon_0}{\varepsilon_c(x,y)} \Pi_m(x) \Lambda_n(y) \Pi_p(x) \Lambda_q(y) d\Omega \right\} - \\
& \sum_{m=1}^M \sum_{n=1}^N s_{m,n}^y \left\{ \int_{\Omega} k_b^2 \Pi_m(x) \Lambda_n(y) \Pi_p(x) \Lambda_q(y) d\Omega - \int_{\Omega} \frac{\partial}{\partial y} [\Pi_m(x) \Lambda_n(y)] \frac{\partial}{\partial y} [\Pi_p(x) \Lambda_q(y)] d\Omega \right\} + \\
& \sum_{m=1}^M \sum_{n=1}^N s_{m,n}^x \left\{ \int_{\Omega} \frac{\partial}{\partial x} [\Lambda_m(x) \Pi_n(y)] \frac{\partial}{\partial y} [\Pi_p(x) \Lambda_q(y)] d\Omega \right\} = \\
& \sum_{m=1}^M \sum_{n=1}^N e_{m,n}^{\text{inc},y} \left\{ \int_{\Omega} \Pi_m(x) \Lambda_n(y) \Pi_p(x) \Lambda_q(y) d\Omega \right\} \quad (6.19)
\end{aligned}$$

for $p = 1, \dots, M$ and $q = 1, \dots, N$.

The first integral in (6.19) is calculated as

$$\begin{aligned}
& \int_{\Omega} \frac{\varepsilon_0}{\varepsilon_c(x,y)} \Pi_m(x) \Lambda_n(y) \Pi_p(x) \Lambda_q(y) d\Omega = \\
& \frac{1}{12} \delta_{m,p} \Delta x \Delta y \varepsilon_0 \left(\delta_{n,q-1} \left(\frac{1}{\varepsilon_{c,m,n}} + \frac{1}{\varepsilon_{c,m,n+1}} \right) + \frac{1}{2} \delta_{n,q} \left(\frac{1}{\varepsilon_{c,m,n-1}} + \frac{14}{\varepsilon_{c,m,n}} + \frac{1}{\varepsilon_{c,m,n+1}} \right) + \delta_{n,q+1} \left(\frac{1}{\varepsilon_{c,m,n-1}} + \frac{1}{\varepsilon_{c,m,n}} \right) \right)
\end{aligned}$$

for $p = 1, \dots, M$ and $q = 1, \dots, N$. Therefore the final expression for the discretized equation is

$$\begin{aligned}
& \frac{1}{12} \varepsilon_0 \left(\left(\frac{1}{\varepsilon_{c,p,q-1}} + \frac{1}{\varepsilon_{c,p,q}} \right) d_{p,q-1}^y + \frac{1}{2} \left(\frac{1}{\varepsilon_{c,p,q-1}} + \frac{14}{\varepsilon_{c,p,q}} + \frac{1}{\varepsilon_{c,p,q+1}} \right) d_{p,q}^y + \left(\frac{1}{\varepsilon_{c,p,q}} + \frac{1}{\varepsilon_{c,p,q+1}} \right) d_{p,q+1}^y \right) - \\
& \frac{1}{6} k_b^2 \left(s_{p,q-1}^y + 4s_{p,q}^y + s_{p,q+1}^y \right) - \frac{1}{\Delta y^2} \left(s_{p,q-1}^y - 2s_{p,q}^y + s_{p,q+1}^y \right) - \frac{1}{4\Delta x \Delta y} \left(s_{p+1,q+1}^x - s_{p-1,q+1}^x - s_{p+1,q-1}^x + s_{p-1,q-1}^x \right) = \\
& \frac{1}{6} \left(e_{p,q-1}^{\text{inc},y} + 4e_{p,q}^{\text{inc},y} + e_{p,q+1}^{\text{inc},y} \right)
\end{aligned}$$

for $p = 1, \dots, M$ and $q = 1, \dots, N$.

The coefficients of the vectorpotential are related to the flux coefficients via

$$s_{p,q}^\alpha = \sum_{m=1}^M \sum_{n=1}^N d_{m,n}^\alpha \frac{\chi_{e,m,n}}{\varepsilon_{c,m,n}} \hat{g}(\mathbf{x} - \mathbf{x}_{m,n}) \Delta x \Delta y.$$

6.5. THE DVIE MODEL ON A STAGGERED GRID

The DVIE method on a staggered grid involves one grid for the x -component and one grid for the y -component. In the grid for the x -component the number of grid nodes in x -direction is increased by one, and in the grid for the y -component the number of grid nodes in y -direction is increased by one. This leads to the expansions

$$\begin{aligned} D_{c,x} &\approx \epsilon_0 \sum_{m=1}^{M+1} \sum_{n=1}^N d_{m,n}^x \phi_{m,n}^x, \\ S_x &\approx \sum_{m=1}^{M+1} \sum_{n=1}^N s_{m,n}^x \phi_{m,n}^x, \\ E_x^{\text{inc}} &\approx \sum_{m=1}^{M+1} \sum_{n=1}^N e_{m,n}^{\text{inc},x} \phi_{m,n}^x \end{aligned}$$

and

$$\begin{aligned} D_{c,y} &\approx \epsilon_0 \sum_{m=1}^M \sum_{n=1}^{N+1} d_{m,n}^y \phi_{m,n}^y, \\ S_y &\approx \sum_{m=1}^M \sum_{n=1}^{N+1} s_{m,n}^y \phi_{m,n}^y, \\ E_y^{\text{inc}} &\approx \sum_{m=1}^M \sum_{n=1}^{N+1} e_{m,n}^{\text{inc},y} \phi_{m,n}^y. \end{aligned}$$

The DVIE formulation on the staggered grid shown in Figure 6.1b requires a couple of changes compared to the DVIE formulation on a non-staggered grid. The basis function covers two entire cells now, which means that the weighting procedure results in a weighting with only two permittivity values instead of three. Therefore evaluation of the first integral in (6.18) results in

$$\int_{\Omega} \frac{\epsilon_0}{\epsilon_c(x,y)} \Lambda_m(x) \Pi_n(y) \Lambda_p(x) \Pi_q(y) d\Omega = \frac{1}{6} \delta_{n,q} \Delta x \Delta y \epsilon_0 \left(\delta_{m,p-1} \frac{1}{\epsilon_{c,m,n}} + 2\delta_{m,p} \left(\frac{1}{\epsilon_{c,m-1,n}} + \frac{1}{\epsilon_{c,m,n}} \right) + \delta_{m,p+1} \frac{1}{\epsilon_{c,m-1,n}} \right)$$

for the x -component for $p = 1, \dots, M+1$ and $q = 1, \dots, N$ and in

$$\int_{\Omega} \frac{\epsilon_0}{\epsilon_c(x,y)} \Pi_m(x) \Lambda_n(y) \Pi_p(x) \Lambda_q(y) d\Omega = \frac{1}{6} \delta_{m,p} \Delta x \Delta y \epsilon_0 \left(\delta_{n,q-1} \frac{1}{\epsilon_{c,m,n}} + 2\delta_{n,q} \left(\frac{1}{\epsilon_{c,m,n-1}} + \frac{1}{\epsilon_{c,m,n}} \right) + \delta_{n,q+1} \frac{1}{\epsilon_{c,m,n-1}} \right)$$

for the y -component for $p = 1, \dots, M$ and $q = 1, \dots, N+1$. Also the expression corresponding with the integral that contains mixed derivatives changes now, because the grid nodes for the y -directional basis functions are shifted from the grid nodes for the x -directional basis functions. Therefore,

$$\int_{\Omega} \frac{\partial}{\partial y} [\Pi_m(x)^y \Lambda_n(y)^y] \frac{\partial}{\partial x} [\Lambda_p(x)^x \Pi_q(y)^x] d\Omega = -(\delta_{m,p} - \delta_{m,p-1}) (\delta_{n,q+1} - \delta_{n,q})$$

for the x -component for $p = 1, \dots, M+1$ and $q = 1, \dots, N$ and

$$\int_{\Omega} \frac{\partial}{\partial x} [\Lambda_m(x) \Pi_n(y)] \frac{\partial}{\partial y} [\Pi_p(x) \Lambda_q(y)] d\Omega = -(\delta_{m,p+1} - \delta_{m,p}) (\delta_{n,q} - \delta_{n,q-1})$$

for the y -component for $p = 1, \dots, M$ and $q = 1, \dots, N+1$.

The final discretized equation for the x -component therefore becomes

$$\begin{aligned} &\frac{1}{6} \epsilon_0 \left(\frac{1}{\epsilon_{c,p-1,q}} d_{p-1,q}^x + 2 \left(\frac{1}{\epsilon_{c,p-1,q}} + \frac{1}{\epsilon_{c,p,q}} \right) d_{p,q}^x + \frac{1}{\epsilon_{c,p,q}} d_{p+1,q}^x \right) - \\ &\frac{1}{6} k_b^2 \left(s_{p-1,q}^x + 4s_{p,q}^x + s_{p+1,q}^x \right) - \frac{1}{\Delta x^2} \left(s_{p-1,q}^x - 2s_{p,q}^x + s_{p+1,q}^x \right) - \frac{1}{\Delta x \Delta y} \left(s_{p,q+1}^y - s_{p-1,q+1}^y - s_{p,q}^y + s_{p-1,q}^y \right) = \\ &\frac{1}{6} \left(e_{p-1,q}^{\text{inc},x} + 4e_{p,q}^{\text{inc},x} + e_{p+1,q}^{\text{inc},x} \right) \end{aligned}$$

for $p = 1, \dots, M+1$ and $q = 1, \dots, N$ and the final discretized equation for the y -component becomes

$$\frac{1}{6} \varepsilon_0 \left(\frac{1}{\varepsilon_{c,p,q-1}} d_{p,q-1}^y + 2 \left(\frac{1}{\varepsilon_{c,p,q-1}} + \frac{1}{\varepsilon_{c,p,q}} \right) d_{p,q}^y + \frac{1}{\varepsilon_{c,p,q}} d_{p,q+1}^y \right) - \frac{1}{6} k_b^2 (s_{p,q-1}^y + 4s_{p,q}^y + s_{p,q+1}^y) - \frac{1}{\Delta y^2} (s_{p,q-1}^y - 2s_{p,q}^y + s_{p,q+1}^y) - \frac{1}{\Delta x \Delta y} (s_{p+1,q}^x - s_{p+1,q-1}^x - s_{p,q}^x + s_{p,q-1}^x) = \frac{1}{6} (e_{p,q-1}^{\text{inc},y} + 4e_{p,q}^{\text{inc},y} + e_{p,q+1}^{\text{inc},y})$$

for $p = 1, \dots, M$ and $q = 1, \dots, N+1$.

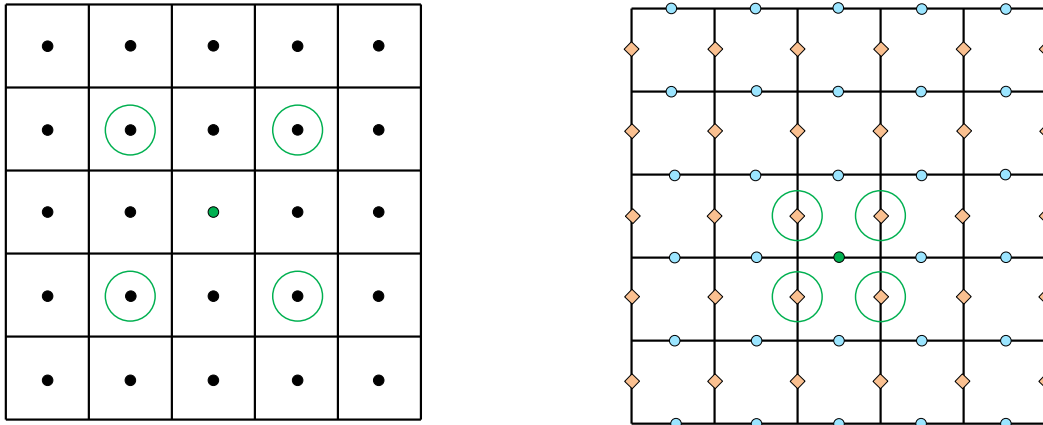
The coefficients are again related via

$$s_{p,q}^x = \sum_{m=1}^{M+1} \sum_{n=1}^N d_{m,n}^x \frac{\chi_{e,m,n}}{\varepsilon_{c,m,n}} \hat{g}(\mathbf{x} - \mathbf{x}_{m,n}) \Delta x \Delta y$$

and

$$s_{p,q}^y = \sum_{m=1}^M \sum_{n=1}^{N+1} d_{m,n}^y \frac{\chi_{e,m,n}}{\varepsilon_{c,m,n}} \hat{g}(\mathbf{x} - \mathbf{x}_{m,n}) \Delta x \Delta y.$$

Figure 6.2 clarifies the main difference between the DVIE method and the DVIE method on a staggered grid. The green encircled nodes are the nodes that are used in the approximation of the mixed derivative in the green filled node. The approximation of the mixed derivative on a non-staggered grid uses nodes that are positioned further away than in the staggered case.



(a) Non-staggered grid.

(b) Staggered grid.

Figure 6.2: The green encircled nodes are used in the second order approximation of the mixed derivative term in the green filled node.

6.6. HIGHER ORDER DIFFERENCE SCHEMES

The two considered equations (5.2) and (5.3) are coupled via the mixed derivative terms and therefore the mixed derivative terms have a big effect on the scattering pattern: it is responsible for scattering in multiple directions. Even though the above derived schemes are a nice result of the rooftop expansion and weighting procedure, it might be interesting to study different discretization schemes for the mixed derivative terms. The schemes that have been constructed are second order central difference schemes. In this section fourth order central difference schemes are derived for staggered as well as for non-staggered grids. Since higher order difference schemes require more grid nodes, extra boundary conditions are needed for grid nodes located on the boundary domain. In order to circumvent extra boundary conditions the original second order difference scheme is applied for nodes located on the boundary.

6.6.1. FOURTH ORDER CENTRAL DIFFERENCE SCHEME FOR A NON-STAGGERED GRID

The fourth order central difference scheme for a non-staggered grid can be derived by repeatedly applying a fourth order central difference scheme on the first derivatives, as in

$$\frac{\partial^2 f}{\partial x \partial y} \Big|_{p,q} = \frac{\partial}{\partial x} \frac{\partial f}{\partial y} \Big|_{p,q} = \frac{1}{12\Delta y} \left(\frac{\partial}{\partial x} f_{\cdot, q-2} \Big|_{p, q-2} - 8 \frac{\partial}{\partial x} f_{\cdot, q-1} \Big|_{p, q-1} + 8 \frac{\partial}{\partial x} f_{\cdot, q+1} \Big|_{p, q+1} - \frac{\partial}{\partial x} f_{\cdot, q+2} \Big|_{p, q+2} \right) + \mathcal{O}(\Delta y^4).$$

Completing the above procedure gives an expression for the y -directional mixed derivative,

$$\begin{aligned} \frac{\partial^2 S^y}{\partial y \partial x} \Big|_{p,q} &\approx \frac{1}{144\Delta x \Delta y} \left[\left(s_{p-2, q-2}^x - 8s_{p-1, q-2}^x + 8s_{p+1, q-2}^x - s_{p+2, q-2}^x \right) \right. \\ &\quad - 8 \left(s_{p-2, q-1}^x - 8s_{p-1, q-1}^x + 8s_{p+1, q-1}^x - s_{p+2, q-1}^x \right) \\ &\quad + 8 \left(s_{p-2, q+1}^x - 8s_{p-1, q+1}^x + 8s_{p+1, q+1}^x - s_{p+2, q+1}^x \right) \\ &\quad \left. - \left(s_{p-2, q+2}^x - 8s_{p-1, q+2}^x + 8s_{p+1, q+2}^x - s_{p+2, q+2}^x \right) \right], \end{aligned}$$

and for the x -directional mixed derivative,

$$\begin{aligned} \frac{\partial^2 S^x}{\partial x \partial y} \Big|_{p,q} &\approx \frac{1}{144\Delta x \Delta y} \left[\left(s_{p-2, q-2}^y - 8s_{p-1, q-2}^y + 8s_{p+1, q-2}^y - s_{p+2, q-2}^y \right) \right. \\ &\quad - 8 \left(s_{p-2, q-1}^y - 8s_{p-1, q-1}^y + 8s_{p+1, q-1}^y - s_{p+2, q-1}^y \right) \\ &\quad + 8 \left(s_{p-2, q+1}^y - 8s_{p-1, q+1}^y + 8s_{p+1, q+1}^y - s_{p+2, q+1}^y \right) \\ &\quad \left. - \left(s_{p-2, q+2}^y - 8s_{p-1, q+2}^y + 8s_{p+1, q+2}^y - s_{p+2, q+2}^y \right) \right]. \end{aligned}$$

6.6.2. FOURTH ORDER CENTRAL DIFFERENCE SCHEME FOR A STAGGERED GRID

The fourth order central difference scheme for a staggered grid can be derived by repeatedly applying a fourth order central difference scheme on the first derivatives, with

$$\frac{\partial f}{\partial y} \Big|_{\cdot, q} = \frac{1}{\Delta y} \left(\frac{3}{2} f_{\cdot, q+\frac{1}{2}} - \frac{1}{6} f_{\cdot, q+\frac{3}{2}} - \frac{3}{2} f_{\cdot, q-\frac{1}{2}} + \frac{1}{6} f_{\cdot, q-\frac{3}{2}} \right) + \mathcal{O}(\Delta y^4).$$

and

$$\frac{\partial f}{\partial x} \Big|_{p, \cdot} = \frac{1}{\Delta x} \left(\frac{3}{2} f_{p+\frac{1}{2}, \cdot} - \frac{1}{6} f_{p+\frac{3}{2}, \cdot} - \frac{3}{2} f_{p-\frac{1}{2}, \cdot} + \frac{1}{6} f_{p-\frac{3}{2}, \cdot} \right) + \mathcal{O}(\Delta x^4).$$

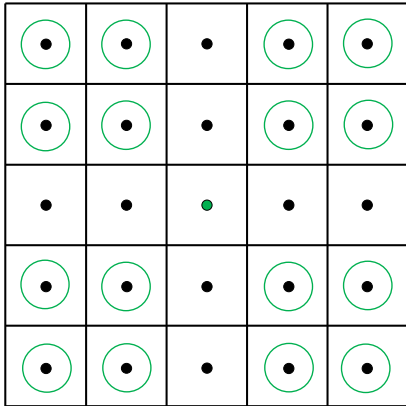
On a staggered grid, this transforms to an expression for the y -directional mixed derivative,

$$\begin{aligned} \frac{\partial^2 S^y}{\partial x \partial y} \Big|_{p,q} &\approx \frac{1}{\Delta x \Delta y} \left[\frac{1}{4} \left(9s_{p+1, q}^x - s_{p+2, q}^x - 9s_{p, q}^x + s_{p-1, q}^x \right) \right. \\ &\quad - \frac{1}{36} \left(9s_{p+1, q+1}^x - s_{p+2, q+1}^x - 9s_{p, q+1}^x + s_{p-1, q+1}^x \right) \\ &\quad - \frac{1}{4} \left(9s_{p+1, q-1}^x - s_{p+2, q-1}^x - 9s_{p, q-1}^x + s_{p-1, q-1}^x \right) \\ &\quad \left. + \frac{1}{36} \left(9s_{p+1, q-2}^x - s_{p+2, q-2}^x - 9s_{p, q-2}^x + s_{p-1, q-2}^x \right) \right], \end{aligned}$$

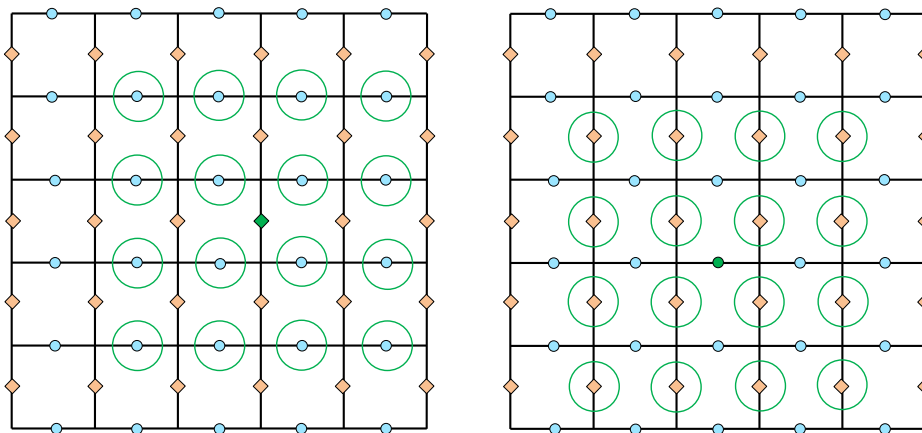
and an expression for the x -directional mixed derivative,

$$\begin{aligned} \frac{\partial^2 S^x}{\partial x \partial y} \Big|_{p,q} &\approx \frac{1}{\Delta x \Delta y} \left[\frac{1}{4} \left(9s_{p, q+1}^y - s_{p+1, q+1}^y - 9s_{p-1, q+1}^y + s_{p-2, q+1}^y \right) \right. \\ &\quad - \frac{1}{36} \left(9s_{p, q+2}^y - s_{p+1, q+2}^y + 9s_{p-1, q+2}^y + s_{p-2, q+2}^y \right) \\ &\quad - \frac{1}{4} \left(9s_{p, q}^y - s_{p+1, q}^y - 9s_{p-1, q}^y + s_{p-2, q}^y \right) \\ &\quad \left. + \frac{1}{36} \left(9s_{p, q-1}^y - s_{p+1, q-1}^y - 9s_{p-1, q-1}^y + s_{p-2, q-1}^y \right) \right]. \end{aligned}$$

Figure 6.3 shows the nodes that are used in the fourth order approximation of the mixed derivative terms for the staggered and the non-staggered grids.



(a) Non-staggered grid.



(b) Staggered grid.

Figure 6.3: The green encircled nodes are used in the fourth order approximation of the mixed derivative term in the green filled node.

7

ITERATIVE SOLVERS

The discretized systems derived in Chapter 6 can be solved with several numerical solution methods. The choice of solver depends among other characteristics on the structure of the system matrix and the problem size. Smaller systems are usually solved with a direct solution method like LU decomposition or Cholesky decomposition. For larger systems iterative solution methods are much more efficient. Iterative schemes can also be used in combination with fast Fourier transform (FFT) methods to accelerate matrix-vector product evaluations. Moreover, iterative methods can be terminated after any tolerance value, which gives the user the opportunity to choose the accuracy of the obtained solution.

Two groups of iterative methods are the basic iterative methods (BIM's) and Krylov subspace methods. Basic iterative methods form the basis of the more advanced Krylov subspace methods. Krylov subspace methods solve the system $A\mathbf{x} = \mathbf{b}$ and are based on the idea that the iterated solution \mathbf{x}^i is an element of $\mathcal{K}^i(A; \mathbf{r}^0)$, where

$$\mathcal{K}^i(A; \mathbf{r}^0) = \text{span}\{\mathbf{r}^0, A\mathbf{r}^0, \dots, A^{i-1}\mathbf{r}^0\}.$$

For systems with a Hermitian and positive definite (HPD) system matrix A the conjugate gradient method is the method of choice. This Krylov subspace method has two attractive properties:

1. $\|\mathbf{x} - \mathbf{x}^i\|_A$ is minimal
2. the algorithm is based on short recurrences.

There is no Krylov subspace method for general matrices that has both properties. Therefore, if the corresponding matrix is Hermitian and positive definite, then there is no reason to choose for more advanced methods constructed for non-Hermitian matrices. Bi-CG, Bi-CGSTAB, GMRES and IDR(s) are examples of methods for general matrices. In this chapter it will be shown that the scattering operator is indeed non-Hermitian and therefore the conjugate gradient method can not be used. Next, GMRES and IDR(s) will be introduced briefly as solvers for systems with non-HPD matrices.

7.1. A NON-HERMITIAN OPERATOR

An operator \mathcal{A} is Hermitian if it satisfies

$$\langle \mathbf{u}, \mathcal{A}\mathbf{v} \rangle = \langle \mathcal{A}\mathbf{u}, \mathbf{v} \rangle \quad \forall \mathbf{u}, \mathbf{v} \in \mathbb{C}^n, \quad (7.1)$$

with the inner product for two-dimensional vectorial functions defined as

$$\langle \mathbf{u}, \mathbf{v} \rangle = \int \langle \mathbf{u}(\mathbf{x}), \mathbf{v}(\mathbf{x}) \rangle d\mathbf{x} = \int u_x(\mathbf{x}) \overline{v_x(\mathbf{x})} + u_y(\mathbf{x}) \overline{v_y(\mathbf{x})} d\mathbf{x}.$$

In this case the operator \mathcal{A} is defined as $\mathcal{A}\mathbf{u} = \mathbf{u} - (k_b^2 + \nabla \nabla \cdot) \mathbf{S}(\chi_e \mathbf{u})$ with $\mathbf{u} \in \mathbb{C}^2$.

With the above definition of the inner product, the left-hand side of (7.1) gives

$$\begin{aligned} \langle \mathbf{u}, \mathcal{A}\mathbf{v} \rangle &= \int u_x(\mathbf{x}) \left(\overline{v_x(\mathbf{x})} - k_b^2 \overline{S_x(\chi_e v_x)} - \left(\frac{\partial}{\partial x} \frac{\partial}{\partial x} \overline{S_x(\chi_e v_x)} + \frac{\partial}{\partial x} \frac{\partial}{\partial y} \overline{S_y(\chi_e v_y)} \right) \right) \\ &\quad + u_y(\mathbf{x}) \left(\overline{v_y(\mathbf{x})} - k_b^2 \overline{S_y(\chi_e v_y)} - \left(\frac{\partial}{\partial y} \frac{\partial}{\partial x} \overline{S_x(\chi_e v_x)} + \frac{\partial}{\partial y} \frac{\partial}{\partial y} \overline{S_y(\chi_e v_y)} \right) \right) d\mathbf{x}, \end{aligned}$$

while the right-hand side of (7.1) gives

$$\begin{aligned} \langle \mathcal{A}\mathbf{u}, \mathbf{v} \rangle &= \int \overline{v_x(\mathbf{x})} \left(u_x(\mathbf{x}) - k_b^2 S_x(\chi_e u_x) - \left(\frac{\partial}{\partial x} \frac{\partial}{\partial x} S_x(\chi_e u_x) + \frac{\partial}{\partial x} \frac{\partial}{\partial y} S_y(\chi_e u_y) \right) \right) \\ &\quad + \overline{v_y(\mathbf{x})} \left(u_y(\mathbf{x}) - k_b^2 S_y(\chi_e u_y) - \left(\frac{\partial}{\partial y} \frac{\partial}{\partial x} S_x(\chi_e u_x) + \frac{\partial}{\partial y} \frac{\partial}{\partial y} S_y(\chi_e u_y) \right) \right) d\mathbf{x}. \end{aligned}$$

Since the equality has to hold for all vectors in \mathbb{C}^2 , it suffices to give one combination of vectors for which the equality does not hold. Now choose $\mathbf{u} = \begin{bmatrix} x \\ 0 \end{bmatrix}$ and $\mathbf{v} = \begin{bmatrix} 0 \\ 1 \end{bmatrix}$ for $x, y \in \Omega$. Then

$$\langle \mathbf{u}, \mathcal{A}\mathbf{v} \rangle = \int -x \frac{\partial}{\partial x} \frac{\partial}{\partial y} \overline{S_y(\chi_e)} d\mathbf{x},$$

and

$$\langle \mathcal{A}\mathbf{u}, \mathbf{v} \rangle = \int -\frac{\partial}{\partial y} \frac{\partial}{\partial x} S_x(\chi_e x) d\mathbf{x}.$$

But $\int x \frac{\partial}{\partial x} \frac{\partial}{\partial y} \overline{S_y(\chi_e)} d\mathbf{x} \neq \int \frac{\partial}{\partial y} \frac{\partial}{\partial x} S_x(\chi_e x) d\mathbf{x}$, which proves that the operator \mathcal{A} is not Hermitian and a Krylov method for general matrices has to be chosen to solve the system.

7.2. GMRES

The generalized minimal residual method (GMRES) is a well-known iteration method for systems where the conjugate gradient method can not be applied. The corresponding algorithm consists of two main steps. In the first step Arnoldi's method is used to construct an orthogonal basis for the Krylov subspace method. In the second step the solution is approximated such that the residual is minimized over the Krylov subspace, i.e.

$$\|\mathbf{r}^i\|_2 = \|\mathbf{b} - A\mathbf{x}^i\|_2 = \min_{\mathbf{z} \in \mathcal{K}^i(A; \mathbf{r}^0)} \|\mathbf{r}^0 - A\mathbf{z}\|_2, \quad (7.2)$$

where the first residual is calculated by $\mathbf{r}^0 = \mathbf{b} - A\mathbf{x}^0$ and \mathbf{x}^0 a chosen starting vector. This means that the residual in iteration i is orthogonal to $A\mathcal{K}^i(A; \mathbf{r}^0)$. The Arnoldi process produces a Hessenberg matrix H_i that represents the projection of matrix A_i on the orthogonal basis with corresponding matrix V_i . The first column of V_i is given by the vector $\mathbf{v}_1 = \frac{\mathbf{r}^0}{\|\mathbf{r}^0\|}$. The choice $\mathbf{z} = V_i \mathbf{y}$ transforms (7.2) into

$$\|\mathbf{r}^i\|_2 = \min_{\mathbf{y} \in \mathbb{R}^n} \|\mathbf{r}^0 - AV_i \mathbf{y}\|_2 = \min_{\mathbf{y} \in \mathbb{R}^n} \|\beta \mathbf{v}_1 - AV_i \mathbf{y}\|_2,$$

where $\beta = \|\mathbf{r}^0\|$. The relation

$$AV_i = V_{i+1} H_i$$

gives a least squares problem

$$\|\mathbf{r}^i\|_2 = \min_{\mathbf{y} \in \mathbb{R}^n} \|V_{i+1}(\beta \mathbf{e}_1 - H_i \mathbf{y})\|_2 = \min_{\mathbf{y} \in \mathbb{R}^n} \|\beta \mathbf{e}_1 - H_i \mathbf{y}\|_2 \quad (7.3)$$

that is equivalent with (7.2). In each iteration the solution is approximated with $\mathbf{x}_i = \mathbf{x}_0 + V_i \mathbf{y}_i$. [24]

GMRES has optimal convergence properties because it minimizes the residual in least-squares sense. The method converges in at most n iterations, where n is the size of the system matrix. GMRES is a stable method with superlinear convergence in many cases. However, GMRES is also an example of a method with long recurrences, which means that the work per iteration and memory requirements increase with the iteration number. More specifically, the computation time is $\mathcal{O}(ni^2)$ after i iterations. A solution to this problem is to restart GMRES after a certain number of iterations with the last approximate solution as a starting vector. Drawbacks of this approach are that optimality and superlinear convergence are lost.

7.3. IDR(s)

The Induced Dimension Reduction method (IDR(s)) is a relatively new method that can also be used to solve large nonsymmetric or non-Hermitian systems. The idea behind the method is based on the IDR theorem of which a generalized version has been published in [25]:

Theorem 1. *Let A be any matrix in $\mathbb{C}^{n \times n}$, let \mathbf{v}_0 be any nonzero vector in \mathbb{C}^n , and let \mathcal{G}_0 be the full Krylov space $\mathcal{K}^n(A, \mathbf{v}_0)$. Let \mathcal{S} denote any (proper) subspace of \mathbb{C}^n such that \mathcal{S} and \mathcal{G}_0 do not share a nontrivial invariant subspace of A , and define the sequence \mathcal{G}_j , $j = 1, 2, \dots$, as*

$$\mathcal{G}_j = (I - \omega_j A)(\mathcal{G}_{j-1} \cap \mathcal{S}),$$

where the ω_j 's are nonzero scalars. Then the following hold:

- i) $\mathcal{G}_j \subset \mathcal{G}_{j-1} \forall j > 0$.
- ii) $\mathcal{G}_j = \{\mathbf{0}\}$ for some $j \leq n$.

In the IDR(s) algorithm the residuals \mathbf{r}^i are forced to be elements of the nested subspaces \mathcal{G}_j . These subspaces are decreasing in dimension, which means that there is a residual \mathbf{r}_m that is an element of $\mathcal{G}_m = \{\mathbf{0}\}$. Once this residual is obtained, the algorithm stops. This happens in at most $\frac{n}{s}(s+1)$ matrix vector products. [26] For $s = 1$ the method converges in at most $2n$ iterations, as opposed to n iterations for GMRES.

When using IDR(s) it is good to have some knowledge of the role of s in the algorithm. From $\frac{n}{s}(s+1) = n + \frac{n}{s}$ it can be seen that an increase in s decreases the number of iterations. An increase in s also involves more memory storage and therefore it is not efficient to choose s too large. In practice values like 4 or 8 usually give good results. [26]

The computation time is $\mathcal{O}(ni)$, where i is again the iteration number. This is a useful property of the IDR(s) method, because it means that although IDR(s) does not minimize the residual and therefore lacks optimal convergence, for larger systems the computation time obtained with IDR(s) may win from the computation time obtained with GMRES, that is $\mathcal{O}(ni^2)$.

7.4. PRECONDITIONING

In order to accelerate convergence, both sides of the equation $A\mathbf{x} = \mathbf{b}$ can be multiplied with a preconditioner M . By doing this, a new system with system matrix $M^{-1}A$ arises. By choosing the preconditioner wisely, the spectrum of the new system matrix can become much more favorable (clustered around 1) which in turn results in faster convergence. Ideally the matrix M would be equal to A , but the computation of A^{-1} is very expensive for systems that are being solved iteratively. A preconditioner equal to the identity matrix would result in a fast computation of $M^{-1}A$, but then the spectrum of the system matrix does not improve. In practice the preconditioner is a compromise between the two.

In this thesis the equation that needs to be solved is expressed in operator form, which makes it more difficult to use existing preconditioners that are constructed via linear algebra techniques. However, in Chapter 8 it will become clear that the effect of preconditioning will be limited for the methods discussed in this research.

8

NUMERICAL SIMULATIONS AND RESULTS

With the models presented in Chapter 6 and the iterative solvers discussed in Chapter 7 numerical simulations can be performed. The first part of this chapter will elaborate on the accuracy of the derived methods. The second part will investigate the efficiency of two iterative solvers. The results shown in this chapter have been obtained using MATLAB's GMRES implementation, unless stated otherwise. All iterative methods have been chosen to terminate when the relative residual drops below the tolerance of $1 \cdot 10^{-8}$.

Table 8.1 gives an overview of the parameters used in the MATLAB codes. The permittivity and conductivity values are chosen such that the outer layer of the two-layer cylinder consists of fat tissue and the inner layer consists of muscle tissue. The frequency is chosen such that it is close to the frequency of 128 MHz that is used in MRI scans with a magnetic field strength of 3T. The same test case has been studied in [7] and [2]. The values in Table 8.1 are used for all simulations, except for the simulations performed in Section 8.1.2 and Section 8.2.2 where contrast dependence is studied.

The number of grid nodes that is required for obtaining a solution with reasonable accuracy is motivated by the wavelength. The wavelength in vacuum is given by $\lambda_0 = \frac{2\pi}{k_b}$ and with $k_b = \sqrt{-\eta_0 \zeta_0}$ as in Table 8.1 this formula gives $\lambda_0 = 3$ meters. Once an electromagnetic wave travels inside an object, the wave number is given by $k = \sqrt{-\eta \zeta_0}$ which results in a wavelength of $\lambda = \frac{2\pi}{\text{Re}(k)}$. This means that for the two-layer cylinder test case ($\epsilon_{r2} = 72$ and $\sigma_2 = 0.9$ S/m) the wavelength shrinks from $\lambda_0 = 3$ meters in vacuum to $\lambda = 0.27$ meter inside the inner layer of the object. In order to obtain an accurate solution, it is advised to use at least 15 grid nodes per wave length. In the two-layer cylinder test case the computational domain is chosen to have a width and a length of 0.3 meters, which is almost the same as the shortest wavelength. Therefore, the domain could in theory be discretized with 15 cells in each direction. However, to be on the safe side the domain is discretized with at least the double amount of cells in each direction.

For the test cases in Section 8.1.2 the material parameters are chosen to have a maximum value of $\epsilon_r = 80$

Symbol	Value	Symbol	Value
c_0	299792458	μ_0	$4\pi \cdot 10^{-7} \approx 1.2566 \cdot 10^{-6}$
f	$100 \cdot 10^6$	μ_{r0}	1
ω	$2\pi f \approx 6.2832 \cdot 10^8$	μ_{r1}	1
k_b	$\sqrt{-\eta_0 \zeta_0} \approx 2.0958$	μ_{r2}	1
ϵ_0	$\frac{1}{c_0^2 \mu_0} \approx 8.8542 \cdot 10^{-12}$	σ_0	0
ϵ_{r0}	1	σ_1	0.048
ϵ_{r1}	7.5	σ_2	0.9
ϵ_{r2}	72	H_0	$-\sqrt{\frac{\epsilon_0}{\mu_0}} \approx -0.0027$
a_1	0.15	a_2	0.079

Table 8.1: Simulation parameters.

and $\sigma = 0$ S/m. The corresponding shortest wavelength for these material parameters is given by 0.34 meter, so also in this case a 30×30 grid should be sufficient to numerically solve the volume integral equation. In order to demonstrate the difference between the different discretization schemes, however, a 50×50 grid is used instead of a 30×30 grid.

8.1. ACCURACY OF THE SOLUTION

In Chapter 6 two different discretizations of the volume integral formulation have been derived. The corresponding models are called the EVIE model and the DVIE model. Both have been derived on a uniform non-staggered grid and the DVIE model has also been derived on a staggered grid.

The accuracy of the three methods will be compared using the analytical solution as benchmark. The analytical solution is a series representation and therefore MATLAB requires termination after a fixed number of terms. The first terms are dominant, which motivates that it is sufficient to sum 21 (zero order, ten positive ordered and ten negative ordered) terms.

After the accuracy of each method has been studied, a method to improve the accuracy is investigated for the most accurate discretization resulting from Section 8.1.1.

8.1.1. COMPARISON OF ACCURACY

Figures 8.1a and 8.1b show the x - and the y -component of the electric field for the three derived methods. In all methods the domain has been divided into 30 cells in each direction. Figures 8.2a and 8.2b show the spatial errors for both components. Two observations can be made here. First, the biggest errors are located on the boundaries of the cylinder layers. Second, the DVIE method on a staggered grid shows the smallest errors for the internal fields (i.e. fields inside the cylinder layers, away from the boundaries). As the grid becomes finer, the bigger errors become more and more local and the internal fields converge to the same fields. Figure 8.3 confirms the local behavior of the error for finer grids.

It is good news that the internal fields of all methods converge to the analytical internal fields. However, regarding memory and time limitations it is necessary that even with coarser grids accurate solutions can be obtained, and it turns out not all methods are capable of doing that. Figure 8.1b illustrates the problem. Both in the EVIE results and in the DVIE results the red areas would predict more heat production than realistic. Also in Figure 8.1a the EVIE and the DVIE methods result in a larger red area than the analytical solution predicts. These false heat predictions can have severe consequences. The question is: what is causing the inaccuracies in the obtained solutions?

Two types of inaccuracies are considered. The first type is the strong inaccuracy on the boundaries of the cylinder layers and the second type is the inaccuracy in the internal fields. Inaccuracies of the latter type decrease as the grid becomes finer, whereas inaccuracies of the first type do not. The strongly local behavior of the inaccuracies of the first type, shown in Figure 8.4a, gives rise to the idea that they are an effect of the so-called 'staircasing', in which curved boundaries are approximated with rectangular cells. [27] To investigate this idea further, the same methods are studied on a square-shaped object instead of on a circular object.

Figure 8.5 shows the x - and the y -component of the electric field for the derived methods on a square-shaped two-layer cylinder. It is important to note that the corners of the squares scatter, as they should. [28] Intuitively, it seems therefore not surprising that the corners of each square cell that is located on the object boundary introduce errors in the case of a curved object boundary. More interesting is Figure 8.4b, which shows the x -component of the electric field along the y -axis for the different methods. The tangential component of the electric field does not show any discontinuous behavior anymore in the absence of a curved boundary. This confirms the idea that the large peaks found in Figure 8.4a are caused by staircasing.

Even though there is no analytical solution to compare with, the comparison of the different methods provides useful information regarding the cause of the inaccuracies in the internal fields. From Figure 8.6a it can be seen that also in the case of a rectangular shaped object the EVIE and the DVIE method on a 30×30 grid differ considerably from the DVIE method on a 30×30 staggered grid, which is assumed to perform best for internal fields. The main difference between the staggered and the non-staggered methods is the way of treating the mixed derivative terms in (5.2) and (5.3). On a non-staggered grid the second order central difference scheme results in an approximation with grid nodes that are positioned further away from the grid node in which the mixed derivative is being approximated. How would other finite difference schemes perform here?

A fourth order central difference scheme for the mixed derivative has been integrated in the EVIE method. The green line in Figure 8.6b shows that the performance of this higher order scheme is almost as good as the performance of the DVIE method on a staggered grid. On the other hand, a fourth order central difference scheme for the DVIE method on a staggered grid decreases the accuracy.

Also for the cylinder configuration the fourth order central difference scheme for the EVIE method improves the accuracy in comparison to the accuracy obtained with the original EVIE method. The performance of the higher order scheme for the DVIE method on a staggered grid is again worse than the performance of the original DVIE method on a staggered grid. The total fields are shown in Figures 8.7a and 8.7b together with their errors in Figures 8.8a and 8.8b. The reason why higher order schemes can deteriorate the accuracy may be found in the fact that higher order schemes require the function to be multiply differentiable. In case of a circular object domain, grid nodes along the object boundary have neighbors with zero contrast both in x - and in y - direction, whereas in case of a rectangular object domain, grid nodes along the object boundary have neighbors with zero contrast only in one direction. This may explain the fact that the EVIE method with a fourth order mixed derivative scheme performs worse on a cylinder than on a square in comparison to the DVIE method on a staggered grid.

The above results prove that the treatment of the mixed derivative has a significant influence on the accuracy of the studied methods. They also suggest that the DVIE method on a staggered grid performs best for curved objects. An error study will be performed to provide a conclusive answer.

In order to derive a global error value for each of the methods, ℓ^1 -norms are computed next to maximum norms. Corrections are made for the number of grid nodes, so that the norms are finally defined as

$$\|E_x - E_{x,\text{analytical}}\|_1 = \frac{\sum_{m,n=1}^{M,N} |E_{x,m,n} - E_{x,\text{analytical},m,n}|}{MN}$$

and

$$\|E_x - E_{x,\text{analytical}}\|_\infty = \max_{m,n} \left\{ |E_{x,m,n} - E_{x,\text{analytical},m,n}| \right\},$$

where M is the number of cells in x -direction and N is the number of cells in y -direction. In order to exclude the contribution of the errors due to the wrong boundary conditions, only the errors in the internal fields are considered by setting the error outside the object equal to zero.

The convergence behavior of the errors for each of the methods can be found in Figure 8.9. For all methods the norm-1 errors decrease as the grid becomes finer, which shows that the internal fields converge to the analytical solution. The non-decreasing behavior of the maximum errors can be explained by the fact that the increase in the number of cells will not change the presence of corners in each square cell. It can even be explained that the maximum errors increase, since scattering patterns around corners can be measured more accurately with smaller cells.

Figure 8.10a shows the same norm-1 errors on loglog scale. All error curves follow the h trend line quite well, which indicates that the accuracy for the internal fields is of order h . Scattering on a square-shaped cylinder gives the results in Figure 8.10b, where the numerical results have been compared with a high resolution solution on a 640×640 grid. There is not much difference between the methods in this case, which can possibly be explained by the fact that the solutions are not affected by staircasing. A higher resolution benchmark solution should be obtained and more grids need to be examined in order to give a conclusive answer, but also in case of scattering on a square-shaped cylinder the accuracy seems to be of order h . The observation that the accuracy of both the circular domain and the square-shaped domain are of order h shows that the staircasing error has negligible effect on the accuracy of the numerical scheme.

As expected, the DVIE method on a staggered grid results in the smallest norm-1 error as well as in the smallest maximum error for all studied grid sizes and it therefore is the most accurate candidate.

8.1.2. THE EFFECT OF THE CONTRAST ON THE ACCURACY

So far the solution has only been studied for one particular test case. The operator \mathcal{A} in $\mathcal{A}\mathbf{u} = \mathbf{f}$, however, is highly dependent on the permittivity and conductivity values of the studied object. It is therefore expected that the accuracy of the methods also depends on the contrast values. In order to investigate how the accuracy is affected by the contrast, a fixed grid of 50×50 cells has been used. A one-layer cylinder without conduction is chosen, so that the permittivity of the cylinder is the only changing factor. The analytical solution for a one-layer cylinder is easily derived from the analytical solution for a two-layer cylinder by choosing the inner

circle radius equal to the outer circle radius. The domain is extended with 0.05 meter in x - and in y -direction. This gives a better global view on the scattering pattern.

Figure 8.11 shows the performance of each method for different permittivity values. Especially for relative permittivity values over 20 the DVIE method on a staggered grid follows the analytical solution much better than the DVIE method and the EVIE method. For a relative permittivity of 4, which corresponds with the material plastic, there is hardly any difference between the studied methods. Relative permittivities smaller than 1 do not exist in nature and will therefore not be considered. These results suggest that especially in applications with high permittivity materials it is important to choose the discretization method wisely and the DVIE method on a staggered grid is the best candidate among the studied schemes for all permittivities.

8.1.3. ERROR REDUCTION

The results from Section 8.1.1 and Section 8.1.2 showed that the DVIE method on a staggered grid produces the most accurate solution for all permittivity values. However, the approximated solution still contains large inaccuracies for the two-layer cylinder test case and one should be careful with neglecting the remaining strong localized jumps. In this section a smoothing method is proposed to remove the jumps. The test case for this problem is again the two-layer cylinder.

The smoothing process is performed by applying a built-in averaging MATLAB filter to the complex relative permittivity matrix. The size of the filter is fixed for all grid sizes and chosen to be a 4×4 matrix, so that the smoothed complex permittivity is defined as

$$\tilde{\epsilon}_{c_{m,n}} = \sum_{R(m,n)} \frac{1}{16} \epsilon_{c_{p,q}}$$

where $R(m, n)$ is a voxelized square with center m, n and containing sixteen nodes p, q . The smoothed complex permittivity defines the contrast by

$$\chi_e = \frac{\eta - \eta_0}{\eta_0} = \frac{\tilde{\epsilon}_c - \tilde{\epsilon}_0}{\epsilon_0}.$$

The effect of the averaging filter can be seen in Figure 8.12, where the electric fields are computed with and without filter on an 80×80 grid. The fields near the permittivity interfaces have become smooth and Figure 8.13 confirms that the averaging filter eliminates the jumps.

Although the smoothing procedure shows good performance regarding the local large peaks, two undesirable effects show up. First of all, coarser grids do not suffice in the smoothed case anymore as the global fields differ too much from the analytical solution for coarse grids. Figure 8.14 shows the effect of different filter sizes on the global fields and on the local peaks, from which it becomes clear that smaller filter sizes do not perform satisfactory. Second, from Figure 8.15 it can be seen that also for fine grids the norm-1 error is bigger when smoothing. Only for very fine grids ($> 1000 \times 1000$) the smoothed method is expected to have better accuracy than the non-smoothed method. One should balance the computation time and the accuracy of the solution to decide whether or not to apply the averaging filter.

8.2. EFFICIENCY OF THE ITERATIVE SOLVER

After the accuracy of all methods has been studied, it is interesting to make an assertion about the method with the shortest computation time. Ideally, the method that results in the most accurate solution is obtained with the shortest computation time, but in practice there is no guarantee for this. If the most accurate solution does not result in the shortest computation time, then it is worthwhile to find efficient ways to speed up the process. This can be done by choosing different solvers for example. Here IDR(s) will be studied as alternative. Details on the IDR(s) implementation have been described in [29].

First, the performance of IDR(s) will be compared with the performance of GMRES by studying the computation times and the number of iterations required for convergence. This is done for all discretizations. Next, in order to determine how the computation times of the solvers change for different objects and therefore different contrast values, a contrast study is performed in Section 8.2.2. Since in this stage it is unknown which discretization results in the shortest computation time, s is set to the default value 4 in this part. After this, the discretization that results in the most accurate solution and is obtained fast is used to find the optimal value for s . Simulations have been performed on a HP ZBook 14 Mobile Workstation using CPU only.

8.2.1. COMPARISON OF IDR(4) AND GMRES

Figure 8.16 shows the convergence behavior obtained with the iterative solvers GMRES and IDR(4) for all methods. The first result that attracts attention is that the convergence of the DVIE method is faster than the convergence of the EVIE method, while both methods use a non-staggered grid and second order finite difference schemes. Apparently, the deviation by ε_c in (3.44) acts as a natural preconditioner. The staggered grid partly cancels out the effect of the natural preconditioner, but still obtains faster convergence than the EVIE method. DVIE staggered with a higher order central difference scheme needs a lot more iterations and is therefore least suitable.

In general, for all methods the convergence behavior corresponding to IDR(4) is similar to the convergence behavior corresponding to GMRES. IDR(4) needs more iterations until convergence, but the IDR(s) graph will move towards the GMRES graph as s increases. The fact that already for $s = 4$ the IDR(s) convergence trend is not much different from the GMRES convergence trend seems promising, since for small s IDR(s) is computationally cheap per iteration. A convergence study will elaborate on the efficiency of IDR(4) with respect to GMRES for different grid sizes and for different contrast values.

Table 8.3 gives an overview of the convergence history for GMRES as well as for IDR(4). For all discretizations and for all grid sizes IDR(4) proves to be beneficial in reducing the computation time of the scattering problem. The last column shows that the improvement factor F , which is the factor between the computation times obtained with GMRES and IDR(4), can reach values up to over 16. For coarser grids, IDR(4) applied to the DVIE and the DVIE method on a staggered grid shows major improvement. For finer grids, the improvement factors for DVIE and DVIE staggered are of the same order as the improvement factor for the EVIE method, but the EVIE method still results in larger computation times for all grids. Therefore DVIE and DVIE staggered seem to be the most efficient methods for the scattering problem.

IDR(4) performed on the EVIE method with a higher order difference scheme decreases the computation time, but the improvement factors are not as good as the improvement factors corresponding with the other formulations. Although they seem to increase where other improvement factors decrease, potential gain can only be expected for unrealistically fine grids. The improvement factors for IDR(4) performed on DVIE staggered with higher order differences turn out to be relatively high, but the corresponding computation times as well as the required number of iterations drastically increase for finer grids. For this reason, results obtained with the DVIE method on a staggered grid with higher order central differences will be left out in further analysis.

Overall, the improvement factors are very high for all discretization schemes. A possible explanation for this could be the use of fast Fourier transforms to evaluate matrix-vector products, so that in the end the overhead of the iterative schemes makes the difference.

The most surprising observation from Table 8.3 is that the number of iterations until convergence for the first four discretizations increases very slowly or does not increase at all. For most finite element problems the number of iterations increases with the number of unknowns, which is why preconditioning techniques are applied. One main difference between finite element systems and method of moment systems is the contribution of the integral term in the latter system. This integral term connects each grid node with all other grid nodes in the contrast domain, while in finite element systems each grid node is only connected with a small number of grid nodes. The coupling with the entire domain (and therefore the increased amount of information in each iteration) could be an explanation for the slow increase in iteration numbers. The fact that the number of iterations seems hardly dependent of the grid size also indicates that the effect of preconditioning will be limited. The integral term seemed a drawback in the beginning because of its computational costs, but it might actually be an advantage for iterative solvers.

Figure 8.17 summarizes the findings from Table 8.3. It illustrates that the computation time corresponding with IDR(4) grows linearly, where the computation time corresponding with GMRES grows faster. This shows that especially for larger systems it is beneficial to use IDR(s) to solve the scattering problem instead of GMRES.

8.2.2. THE EFFECT OF THE CONTRAST ON THE CONVERGENCE BEHAVIOR

Earlier studies brought forward that the contrast does not only affect the accuracy of the solution as explained in Section 8.1.2, but it also affects the convergence behavior of the iterative method. [4] This is not surprising, since the convergence of an iterative method depends on the properties of the operator \mathcal{A} in $\mathcal{A}\mathbf{u} = \mathbf{f}$. Hence, the choice of the most efficient solver may change for different materials. Scattering on the same one-layer homogeneous cylinder as in Section 8.1.2 is studied to find the effect of permittivity values on the number of

iterations until convergence.

Figure 8.18 shows the number of iterations as a function of relative permittivity, both for GMRES and IDR(4). A relative permittivity of $\varepsilon_r = 1$ corresponds with the permittivity in vacuum, which means that in this case the incoming wave is not affected by the object and the total field is equal to the incident field. Numerical schemes will converge fastest to the desired tolerance for this simplified equation. Some iterations are still needed, partly because the default initial MATLAB guess is equal to the zero vector. For larger relative permittivities the convergence behavior of GMRES is slightly less affected by the change in contrast compared with IDR(4), but the difference is so small that it should not be a reason to choose for GMRES over IDR(s). None of the discretization methods distinguishes itself by a remarkably small increase in number of iterations. However, DVIE on a staggered grid wins from DVIE on a non-staggered grid for relative permittivities above 50. This can be explained by the fact that for low contrast the scattered field has a lower intensity, which results in a smaller error when approximating the derivative of a discontinuous function than for high contrast.

8.2.3. THE CHOICE OF THE PARAMETER s IN IDR(s)

The default value $s = 4$ usually gives good results, but until other values are studied it is unclear what the optimal value for s is. In Section 8.1.1 the DVIE method on a staggered grid came forward as the most accurate solution on low resolution. The results in Section 8.2.1 and Section 8.2.2 showed that the DVIE method and the DVIE method on a staggered grid both result in a short computation time with respect to the other discretizations. The DVIE method on a staggered grid meets both the requirements of providing an accurate solution and obtaining it fast, and therefore this discretization will be used to perform a study on the choice of s in IDR(s). For this study three different grid sizes are studied to investigate whether the choice of s is independent of the number of unknowns. The chosen grids have dimensions 30×30 , 80×80 and 200×200 . Also for this part the two-layer cylinder test case with fat-muscle structure is used.

Table 8.2 shows the computation time per grid for different values of s . The blue cells highlight the values for s that correspond with the shortest computation times. For the 30×30 grid and the 80×80 grid the optimal value for s is eight, whereas for the 200×200 grid and the 800×800 grid the optimal value for s is seven. For coarse grids the differences in computation times are very small which makes it difficult to draw a well-grounded conclusion on the optimal value for s . However, the values for s on finer grids do indicate that it is safe to say that for small as well as for reasonably large systems corresponding with the scattering problem the value $s = 7$ gives a shorter computation time than most other values for s . This is why it is advised to use $s = 7$ when solving the scattering problem with IDR(s) in combination with the method of moments rooftop procedure.

30 × 30 grid		80 × 80 grid		200 × 200 grid		800 × 800 grid	
s	Time (s)	s	Time (s)	s	Time (s)	s	Time (s)
1	0.5549	1	2.1514	1	15.6920	1	365.5334
4	0.4682	4	1.8960	4	12.0853	4	264.1190
6	0.4737	6	1.9066	6	11.4244	6	263.6863
7	0.4619	7	1.8344	7	11.2148	7	256.4527
8	0.4529	8	1.7562	8	11.3874	8	269.2184
9	0.4796	9	1.8654	9	11.5593	9	302.6396
10	0.4740	10	1.9637	10	12.0675	10	295.7552
12	0.4905	12	1.9741	12	12.3798	12	288.8659

Table 8.2: Computation times for different grids and different values for s .

Grid	GMRES			IDR(4)			F
	# Iterations	Time [s]	Time/iteration [s]	# Iterations	Time [s]	Time/iteration [s]	
30 × 30	147	4.9228	0.0334	197	0.3155	0.0016	15.6
60 × 60	156	9.3871	0.0602	201	1.1129	0.0055	8.4
120 × 120	158	21.7316	0.1375	204	3.2255	0.0158	6.78
240 × 240	155	85.2705	0.5501	198	17.5570	0.0887	4.9
480 × 480	153	488.2831	3.1914	217	104.5597	0.4818	4.7

(a) Iterations for DVIE staggered.

Grid	GMRES			IDR(4)			F
	# Iterations	Time [s]	Time/iteration [s]	# Iterations	Time [s]	Time/iteration [s]	
30 × 30	97	2.9593	0.0305	120	0.1805	0.0015	16.4
60 × 60	129	7.7442	0.0600	159	1.3083	0.0082	5.9
120 × 120	149	19.9902	0.1342	164	2.7245	0.0166	7.3
240 × 240	157	85.2475	0.5430	179	14.5188	0.0811	5.9
480 × 480	157	505.0779	3.2171	192	97.1587	0.5060	5.2

(b) Iterations for DVIE.

Grid	GMRES			IDR(4)			F
	# Iterations	Time [s]	Time/iteration [s]	# Iterations	Time [s]	Time/iteration [s]	
30 × 30	198	3.0578	0.0154	254	0.4883	0.0019	6.3
60 × 60	221	9.1985	0.0416	295	2.3579	0.0080	3.9
120 × 120	227	25.1534	0.1108	293	5.8537	0.0200	4.3
240 × 240	226	129.4374	0.5727	294	31.5180	0.1072	4.1
480 × 480	223	827.6930	3.7116	295	166.5502	0.5646	5.0

(c) Iterations for EVIE.

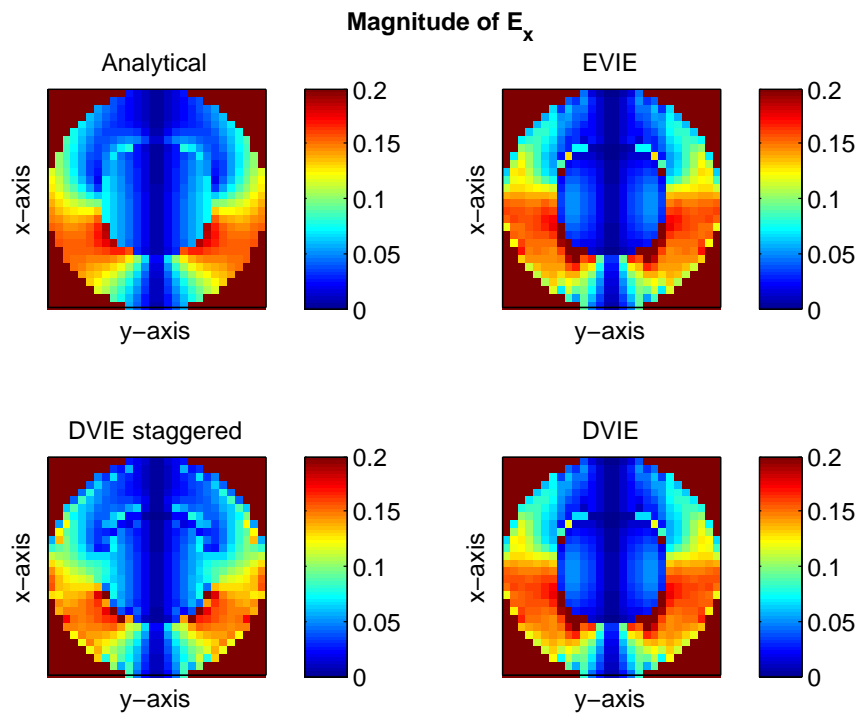
Grid	GMRES			IDR(4)			F
	# Iterations	Time [s]	Time/iteration [s]	# Iterations	Time [s]	Time/iteration [s]	
30 × 30	204	1.5560	0.0076	270	0.9746	0.0036	1.6
60 × 60	235	8.1297	0.0346	320	4.5508	0.0142	1.8
120 × 120	236	27.6812	0.1173	300	14.3996	0.0480	1.9
240 × 240	232	145.1201	0.6255	321	71.9152	0.2240	2.0
480 × 480	227	960.5907	4.2317	263	306.0926	1.1639	3.1

(d) Iterations for EVIE with HOD.

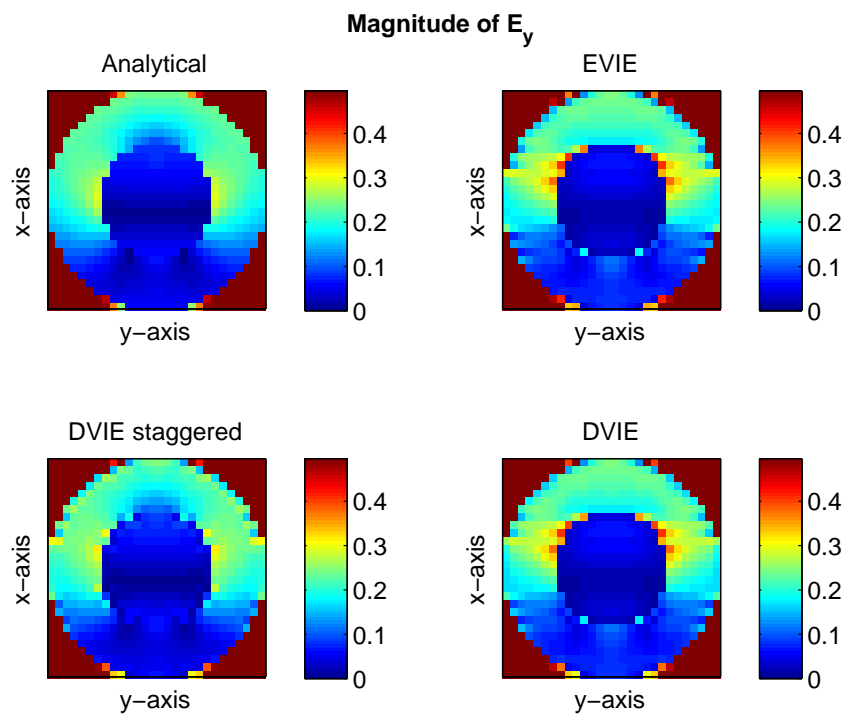
Grid	GMRES			IDR(4)			F
	# Iterations	Time [s]	Time/iteration [s]	# Iterations	Time [s]	Time/iteration [s]	
30 × 30	479	15.7654	0.0329	709	2.2209	0.0031	7.1
60 × 60	820	95.4705	0.1164	1000	11.9696	0.0120	8.0
120 × 120	1121	758.4675	0.4320	1568	65.6008	0.0418	11.6
240 × 240	1270	6599.2	5.1962	1792	373.4804	0.2084	17.7
480 × 480	O.o.m.	O.o.m.	O.o.m.	1864	1985.6	1.0652	-

(e) Iterations for DVIE staggered with HOD.

Table 8.3: Number of iterations until convergence for different numerical schemes. O.o.m. = out of memory.

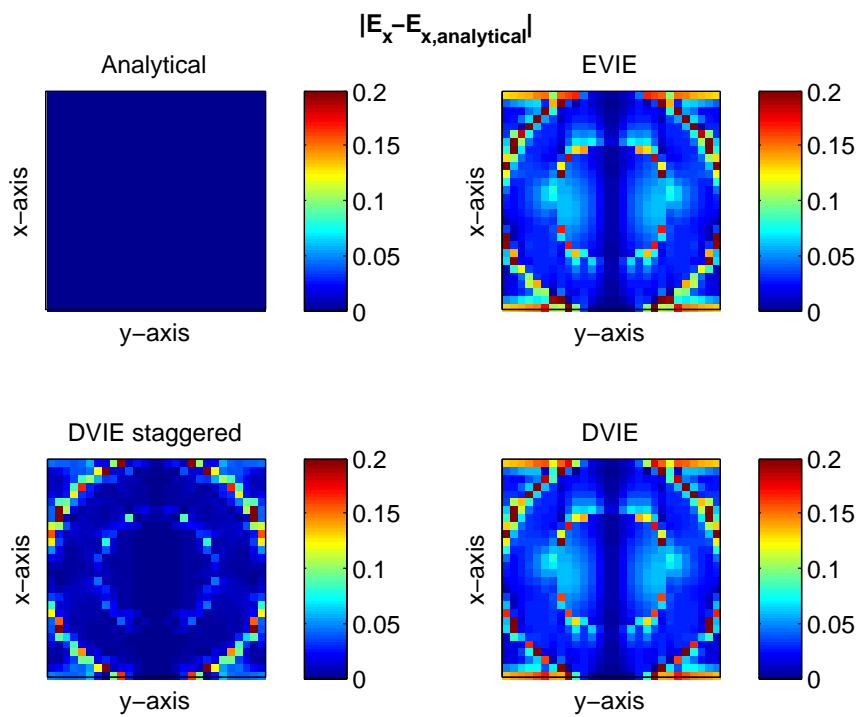
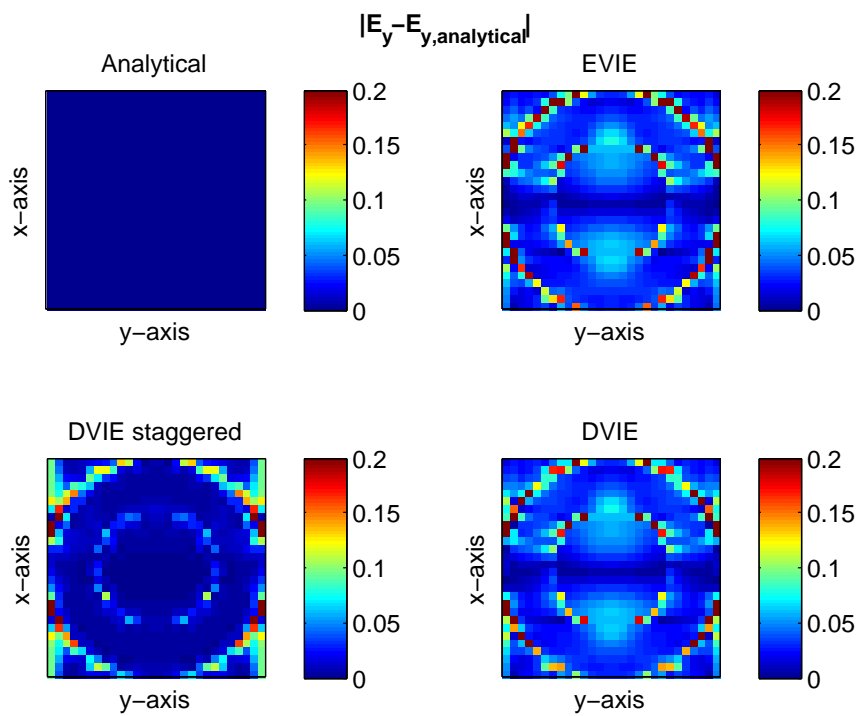


(a) The magnitude of E_x [V/m].



(b) The magnitude of E_y [V/m].

Figure 8.1: The magnitude of the electric field calculated with the different methods on a 30×30 grid.

(a) The absolute error [V/m] for the x -component.(b) The absolute error [V/m] for the y -component.Figure 8.2: The magnitude of the electric field calculated with the different methods on a 30×30 grid.

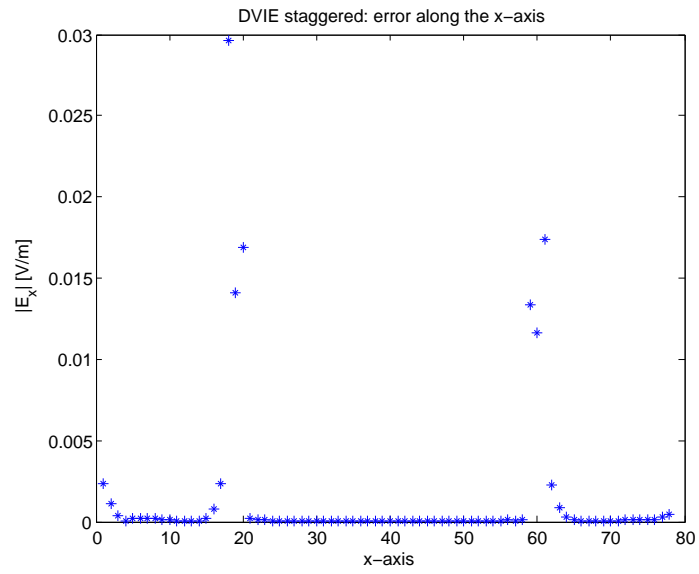
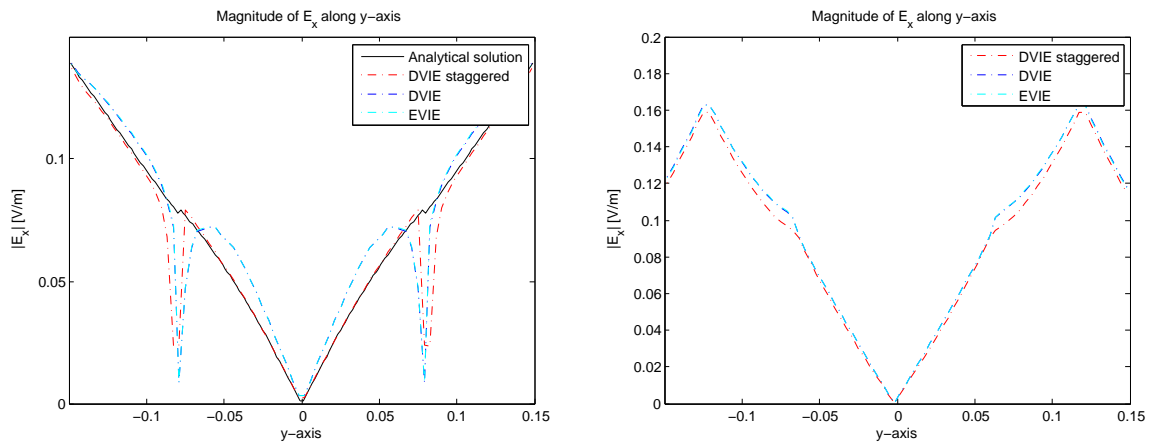


Figure 8.3: The absolute error on a 80×80 grid for E_x along the x -axis on an 80×80 grid.



(a) Scattering on a circular cylinder.

(b) Scattering on a square-shaped cylinder.

Figure 8.4: The magnitude of E_x along the y -axis calculated on a 80×80 grid for different geometries.

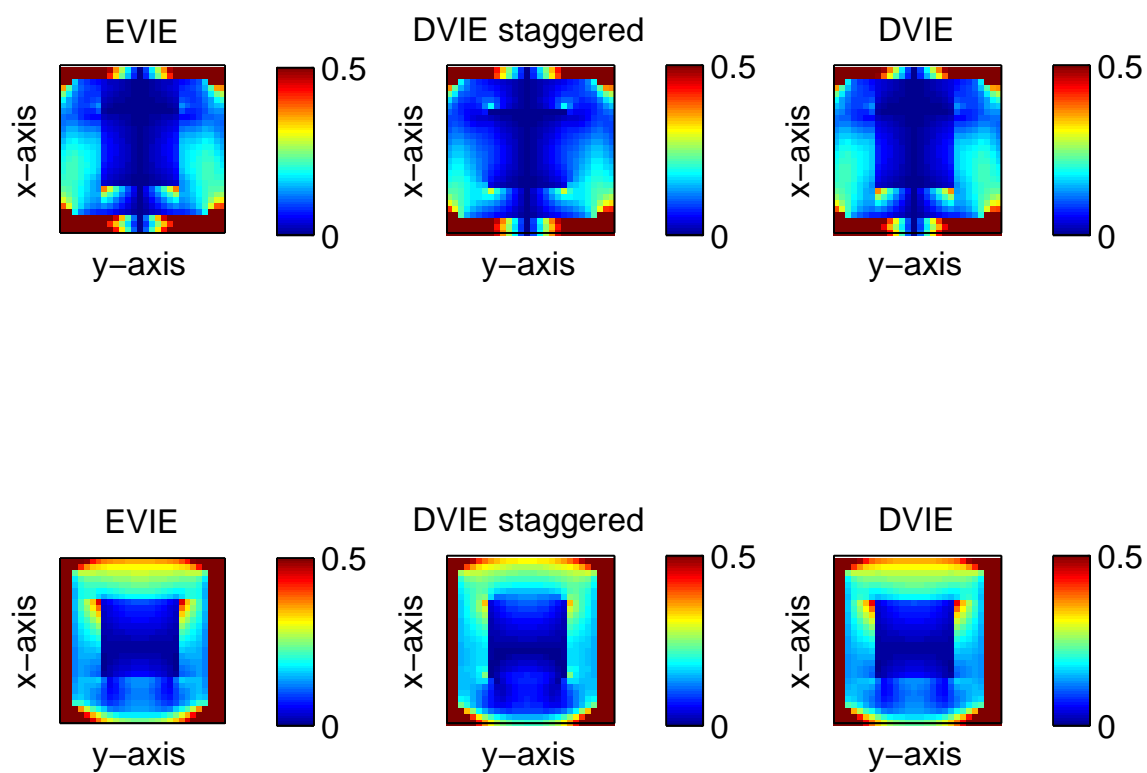
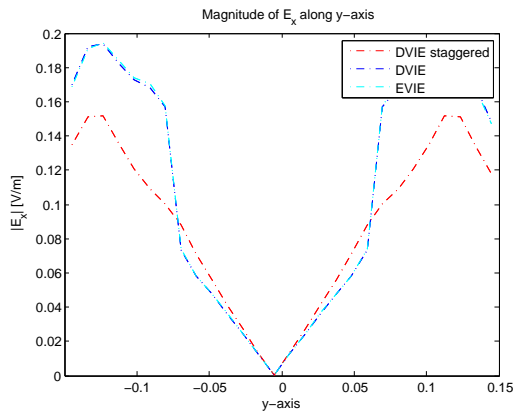
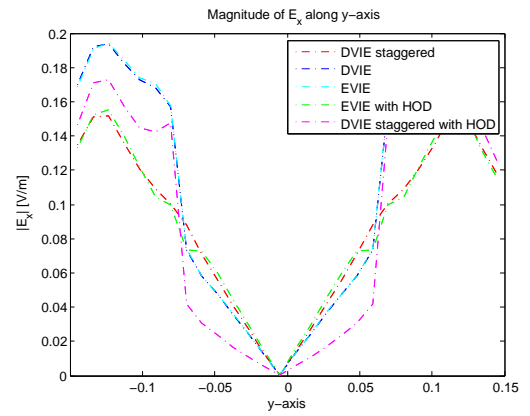


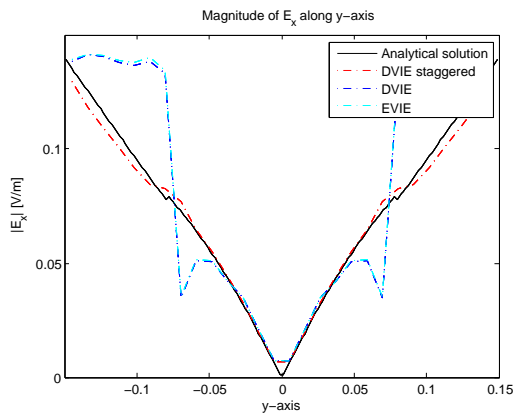
Figure 8.5: E_x [V/m] and E_y [V/m] for scattering on a square-shaped cylinder, calculated with the different methods on a 30×30 grid.



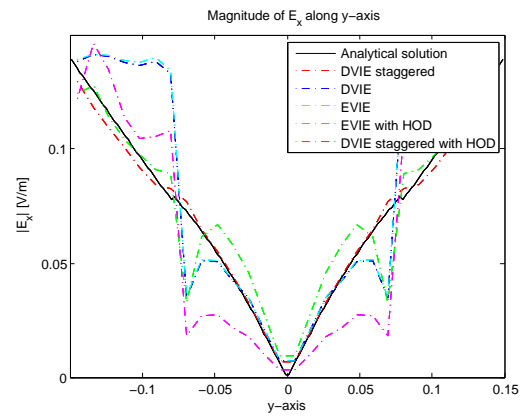
(a) Scattering on a square-shaped cylinder.



(b) Scattering on a square-shaped cylinder.

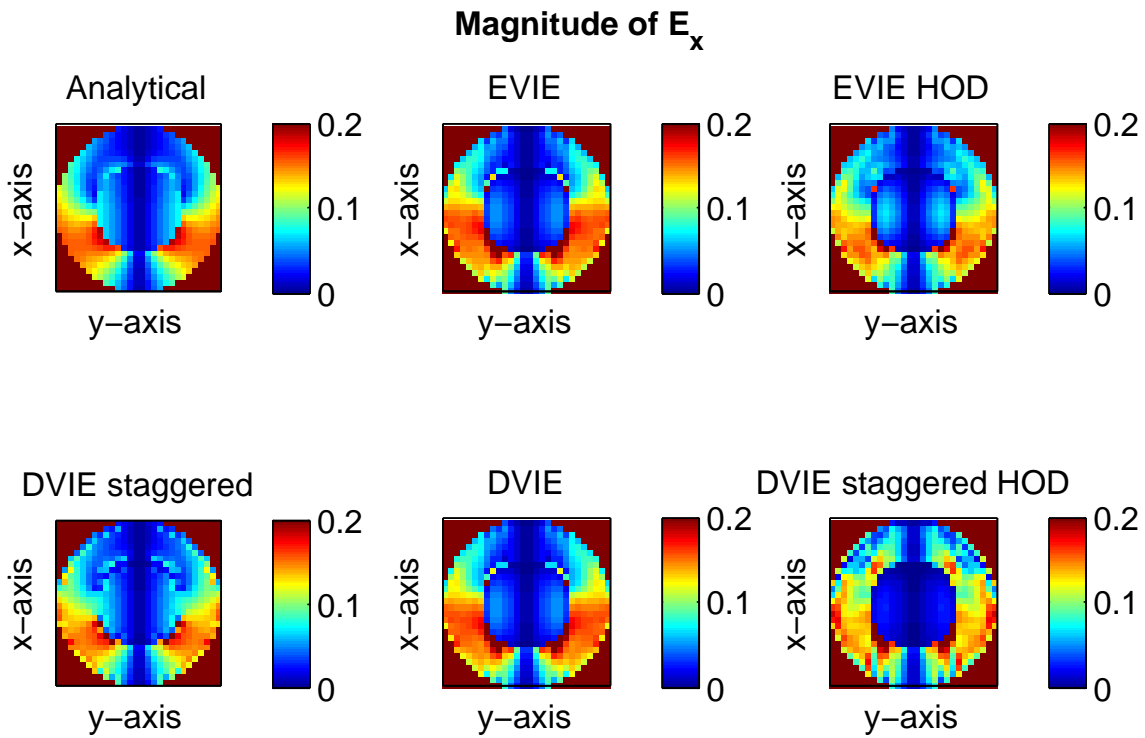
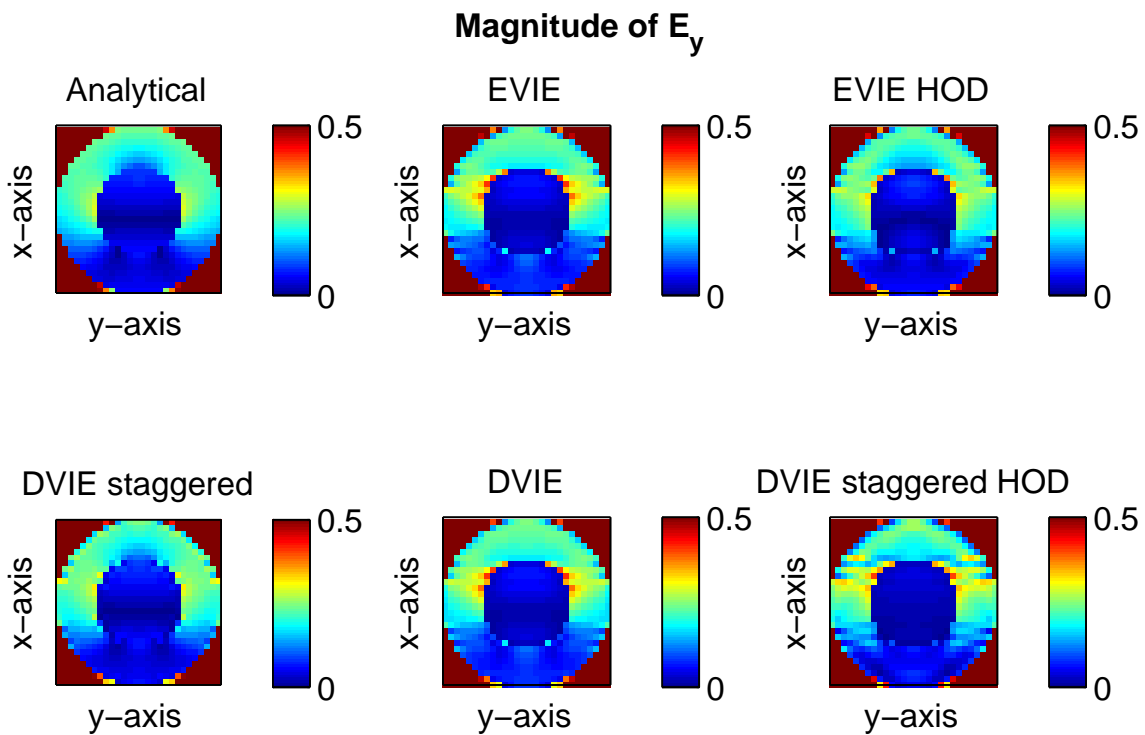


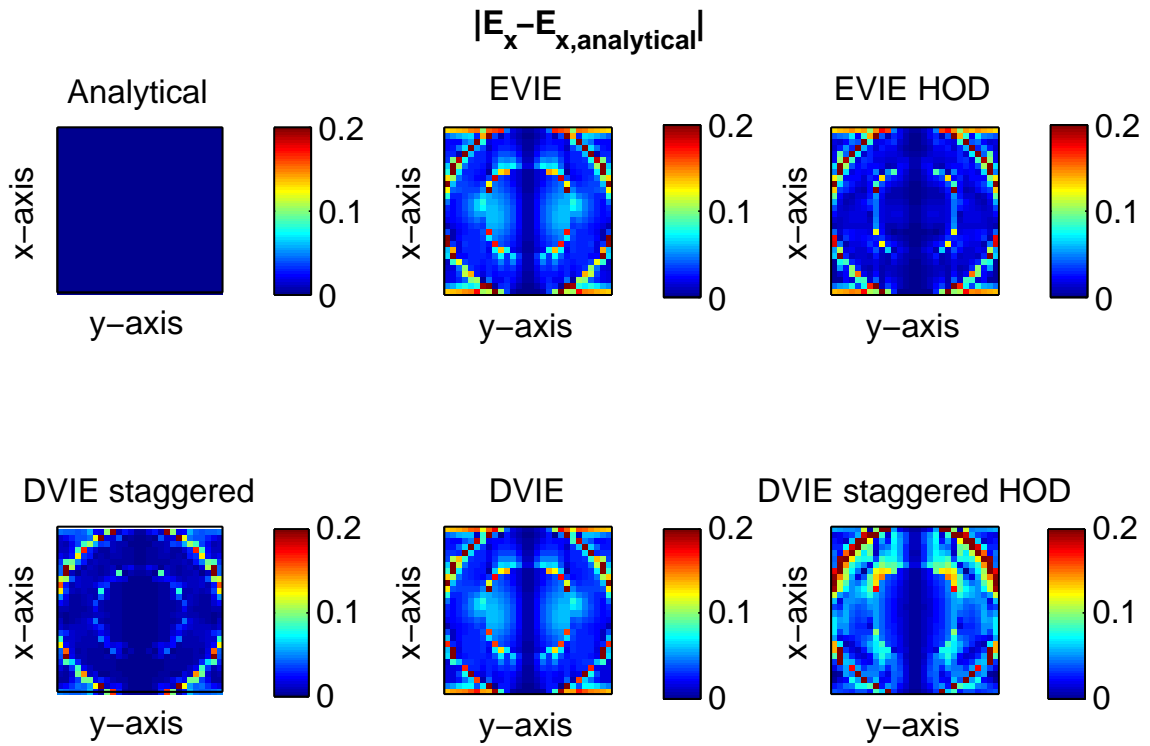
(c) Scattering on a circular cylinder.



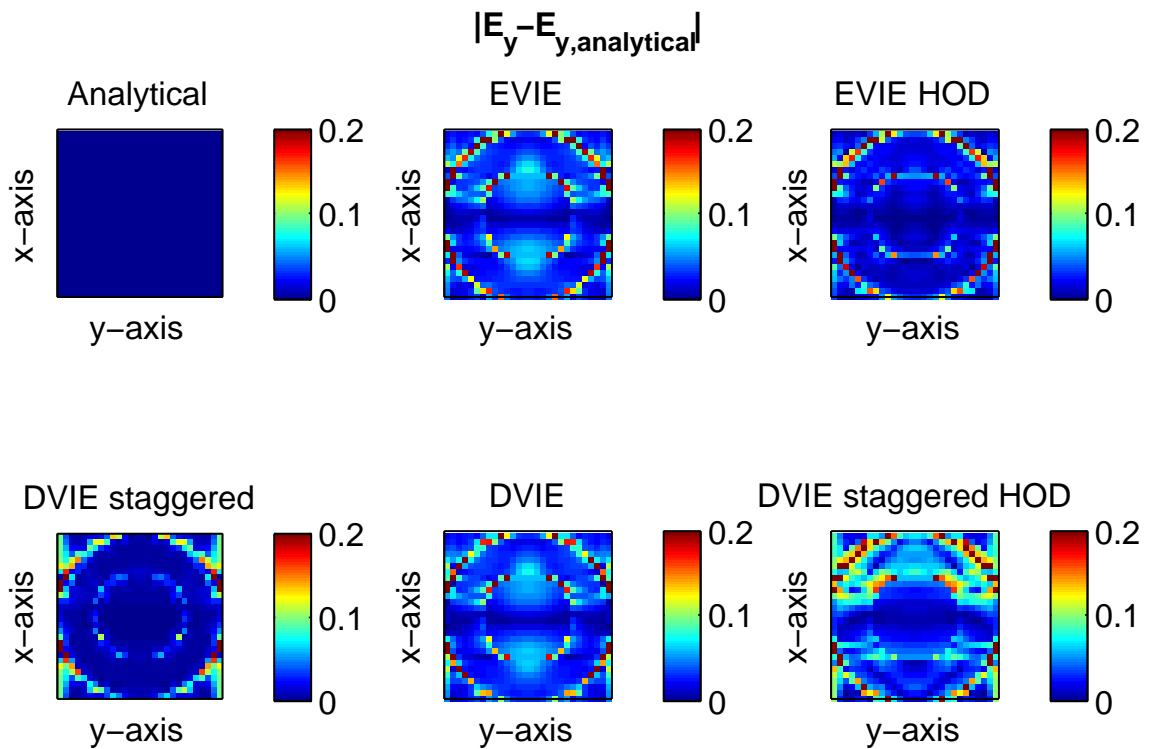
(d) Scattering on a circular cylinder.

Figure 8.6: The magnitude of the x -component of the electric field along the y -axis calculated with the different methods on a 30×30 grid.

(a) The magnitude of E_x [V/m].(b) The magnitude of E_y [V/m].Figure 8.7: Scattering on a circular cylinder, calculated with the different methods on a 30×30 grid.



(a) The absolute error [V/m] for the x -component.



(b) The absolute error [V/m] for the y -component.

Figure 8.8: The absolute error calculated with the different methods on a 30×30 grid.

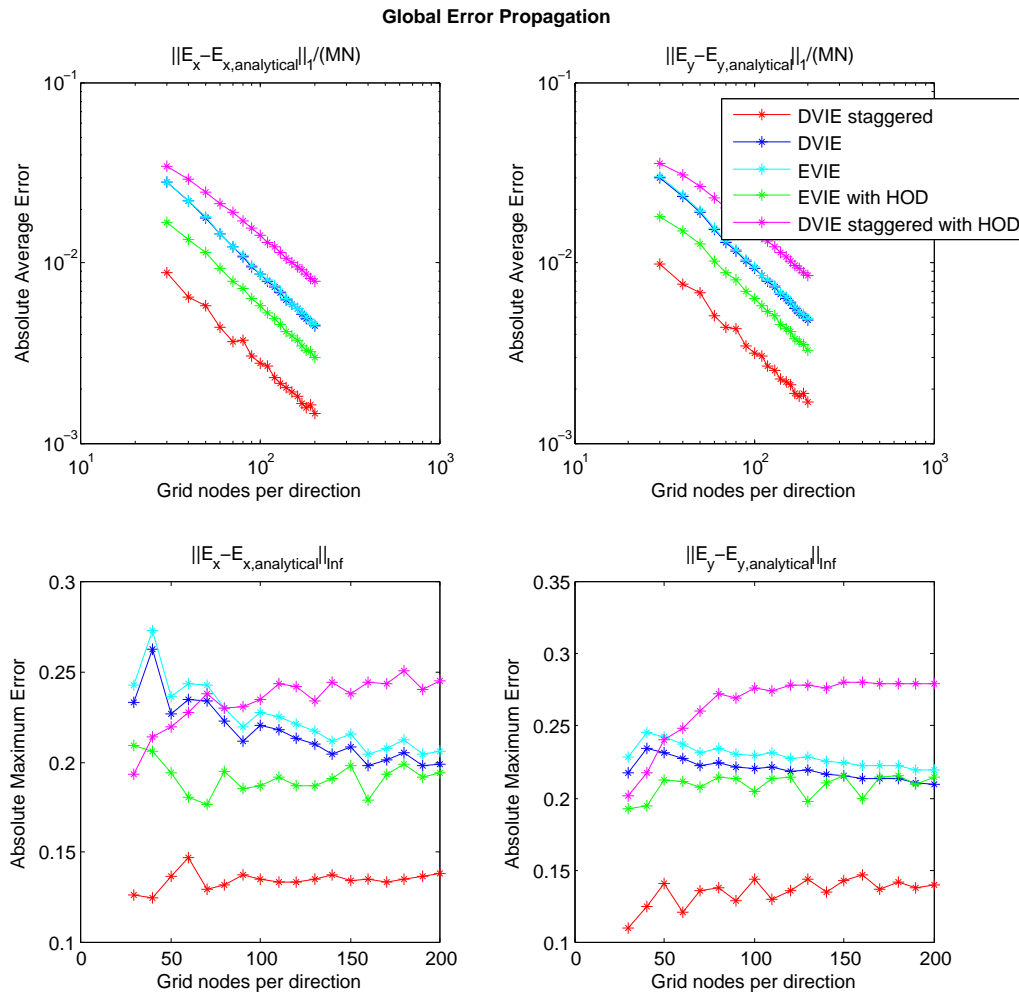
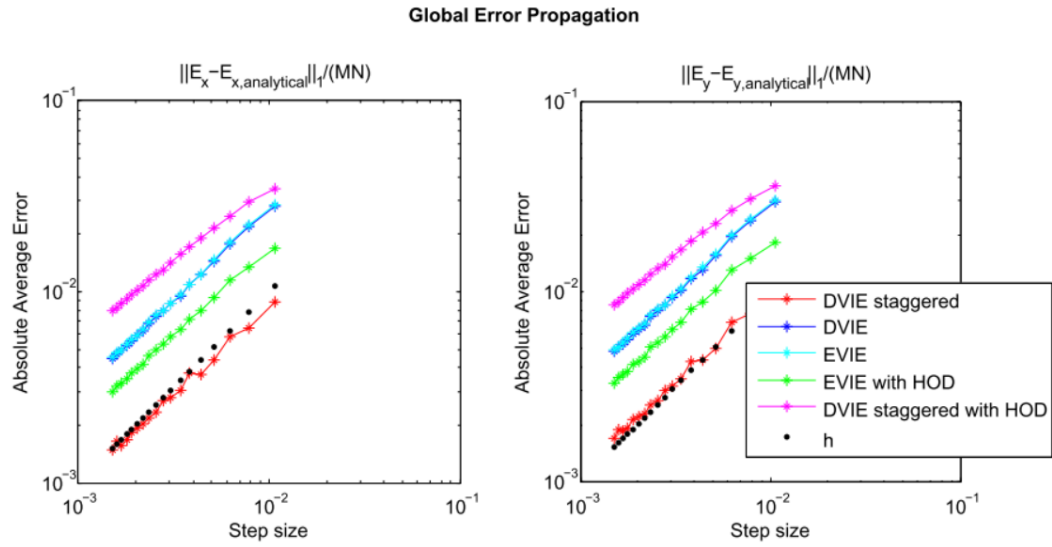
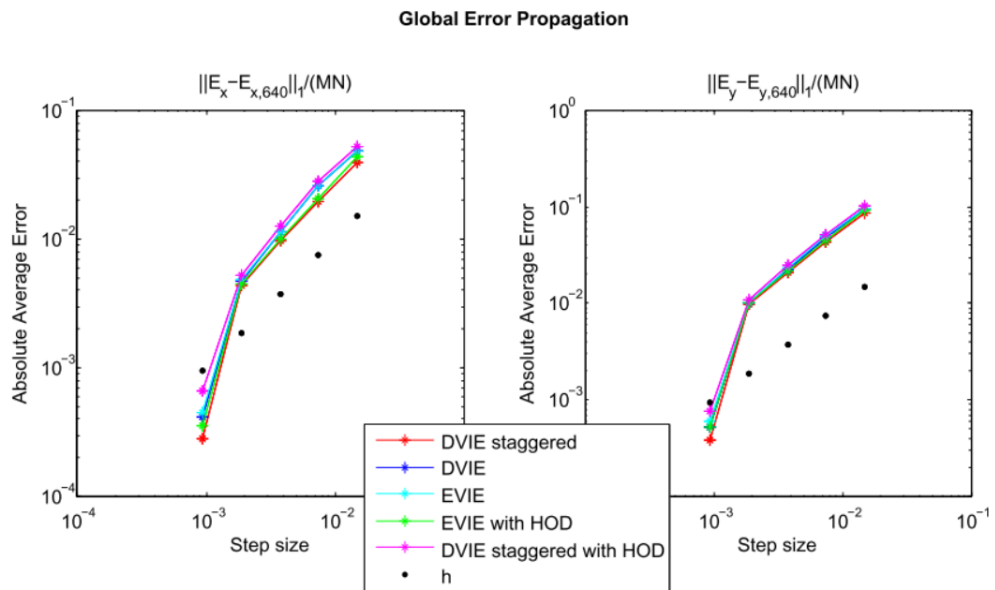


Figure 8.9: The norm-1 errors and maximum errors [V/m] as a function of grid size.

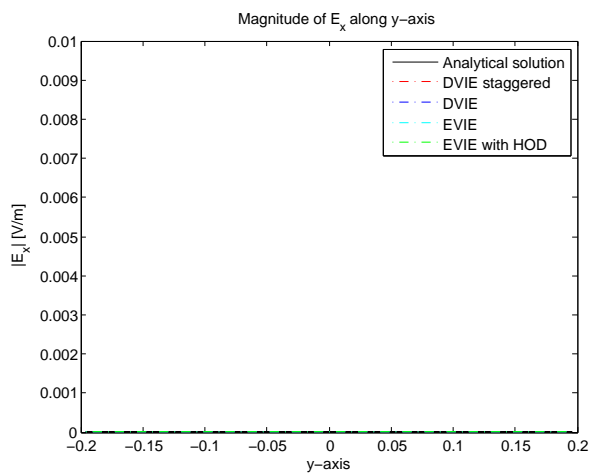


(a) Scattering on a circular cylinder.

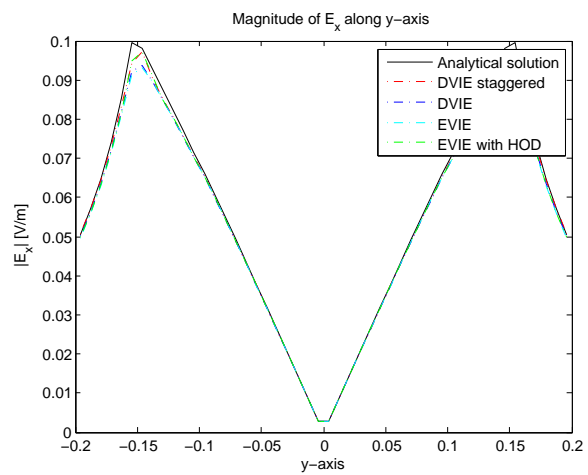


(b) Scattering on a square-shaped cylinder.

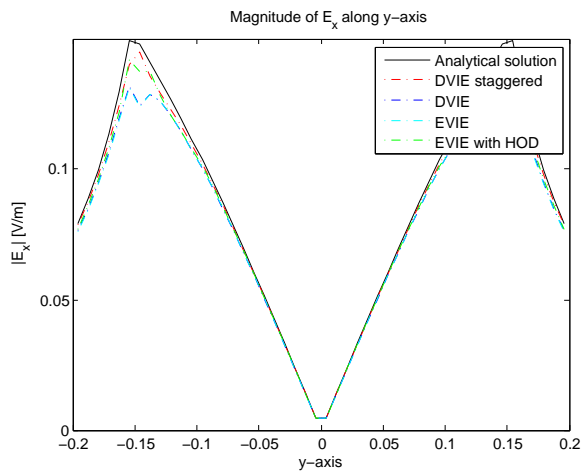
Figure 8.10: The norm-1 errors [V/m] as a function of grid size for different geometries.



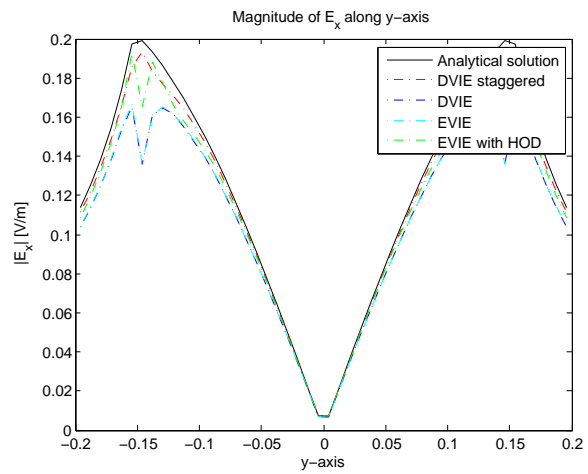
(a) $\epsilon_r = 1, \sigma = 0$



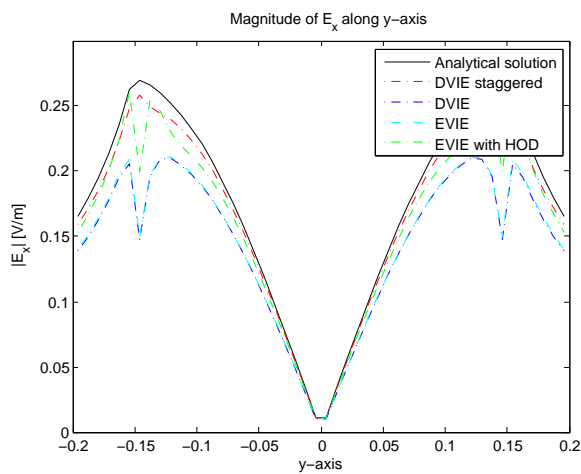
(b) $\epsilon_r = 4, \sigma = 0$



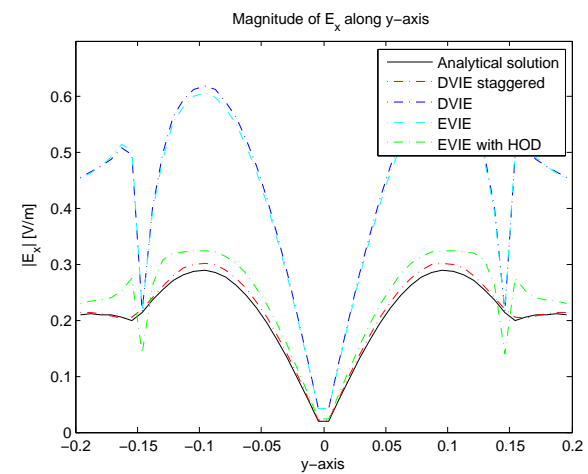
(c) $\epsilon_r = 10, \sigma = 0$



(d) $\epsilon_r = 20, \sigma = 0$

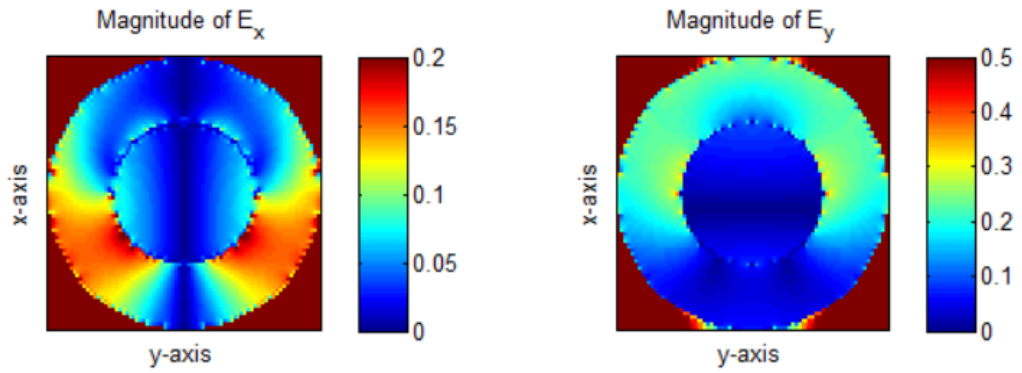


(e) $\epsilon_r = 30, \sigma = 0$

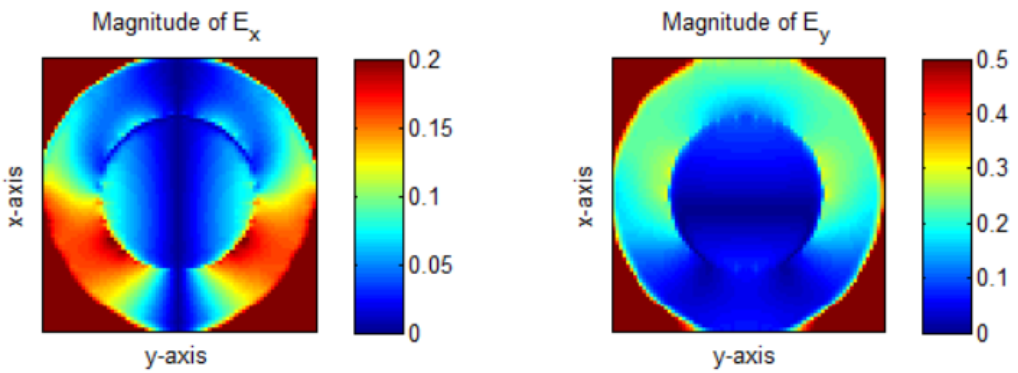


(f) $\epsilon_r = 80, \sigma = 0$

Figure 8.11: Scattering on a single layer cylinder on a 50×50 grid.

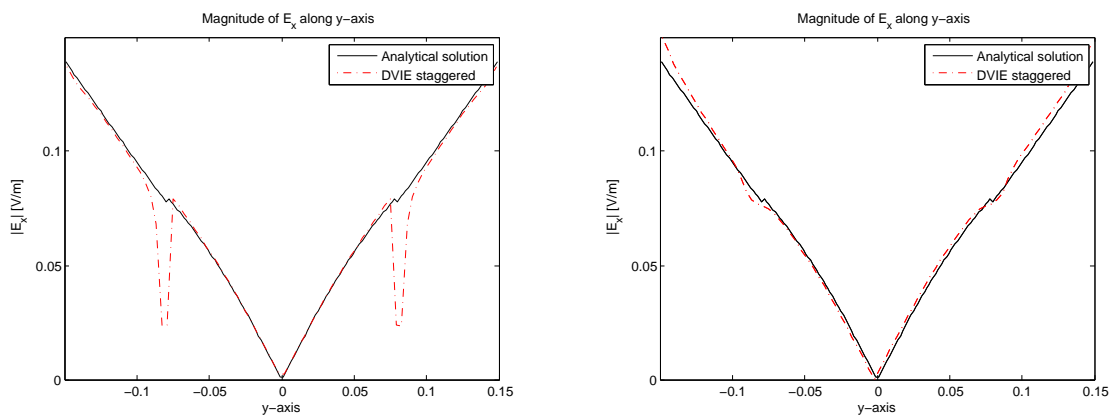


(a) The magnitude of E_x [V/m] and E_y [V/m] for scattering on a circular cylinder.



(b) The magnitude of E_x [V/m] and E_y [V/m] for scattering on a circular cylinder with smoothed contrast.

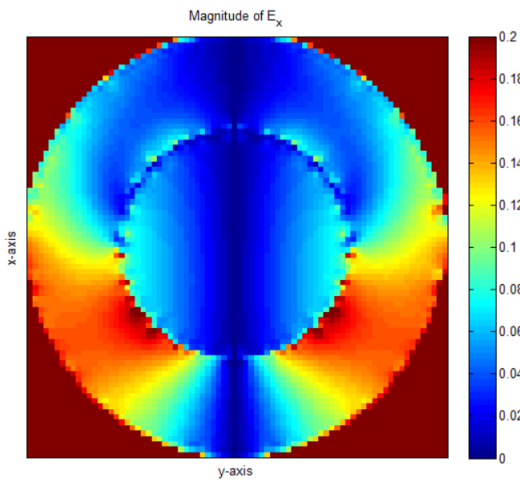
Figure 8.12: Scattering on a circular cylinder calculated with DVIE staggered on an 80×80 grid.



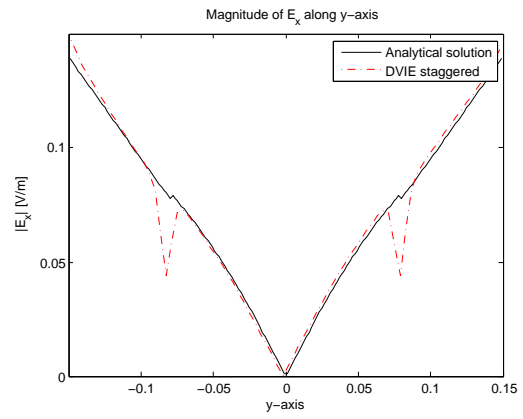
(a) Scattering on a circular cylinder.

(b) Scattering on a circular cylinder with smoothed contrast.

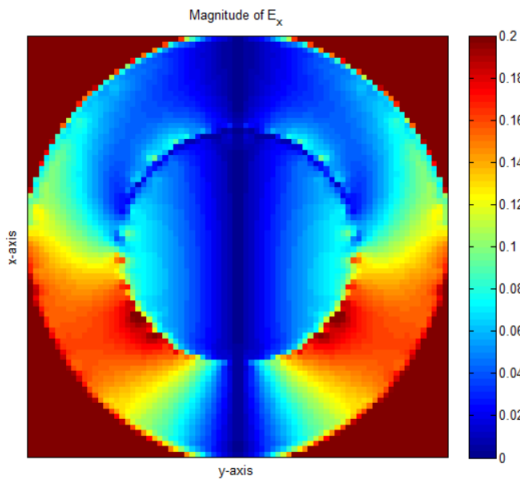
Figure 8.13: The magnitude of E_x along the y -axis calculated with DVIE staggered on an 80×80 grid .



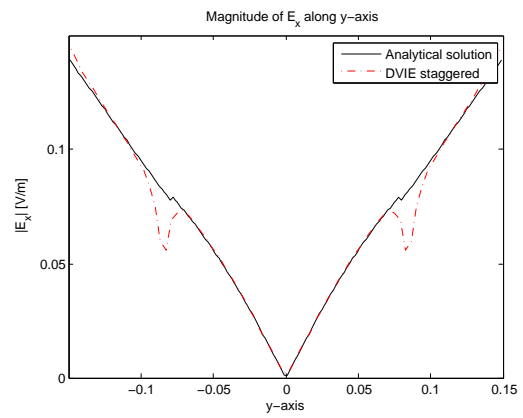
(a) 2×2 filter



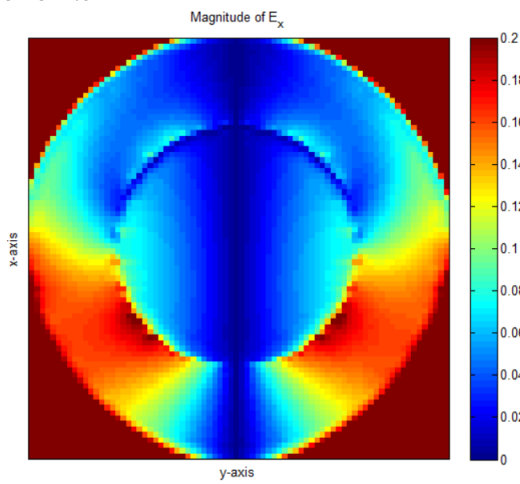
(b) 2×2 filter



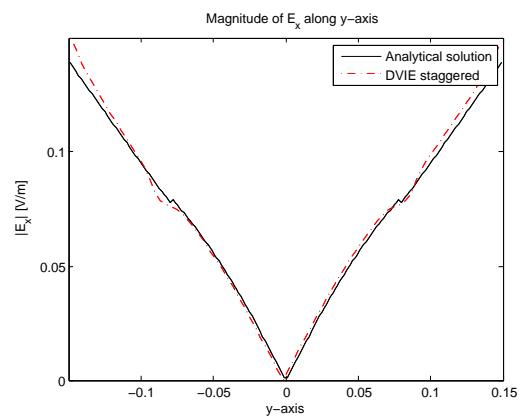
(c) 3×3 filter



(d) 3×3 filter



(e) 4×4 filter



(f) 4×4 filter

Figure 8.14: The effect of smoothing with DVIE staggered on an 80×80 grid.

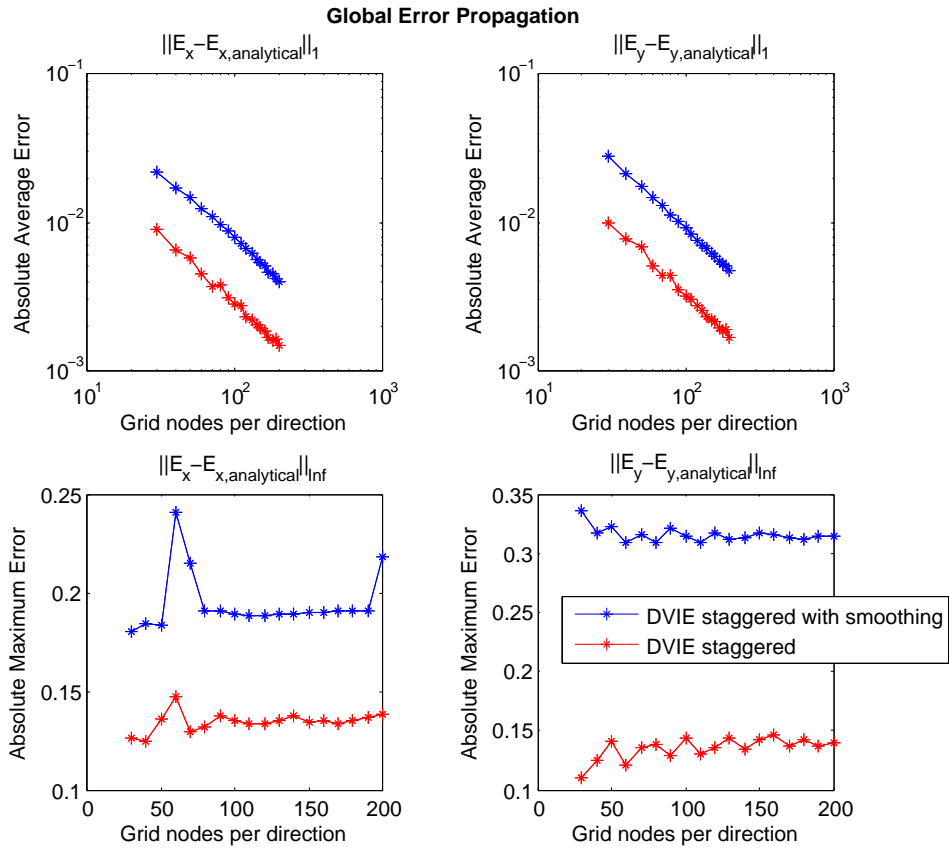


Figure 8.15: The effect of smoothing for the DVIE method on a staggered grid.

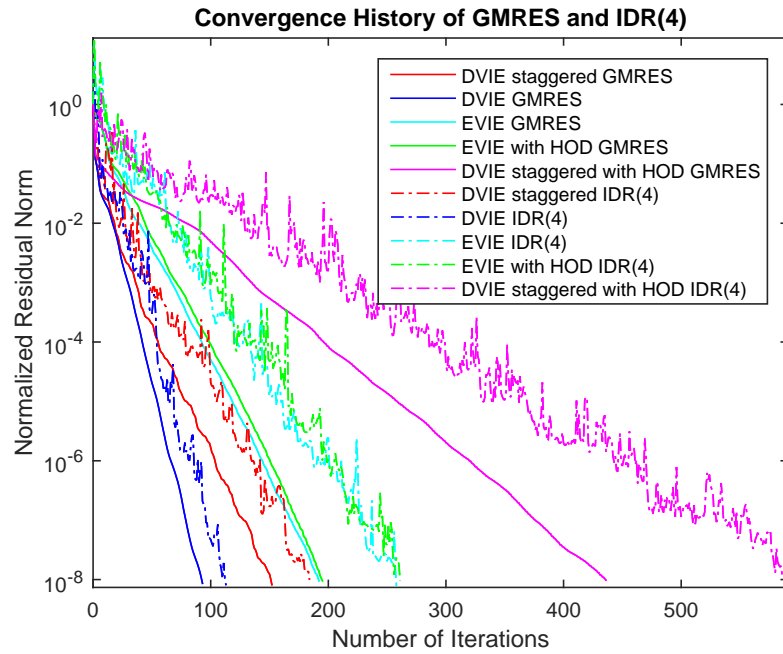
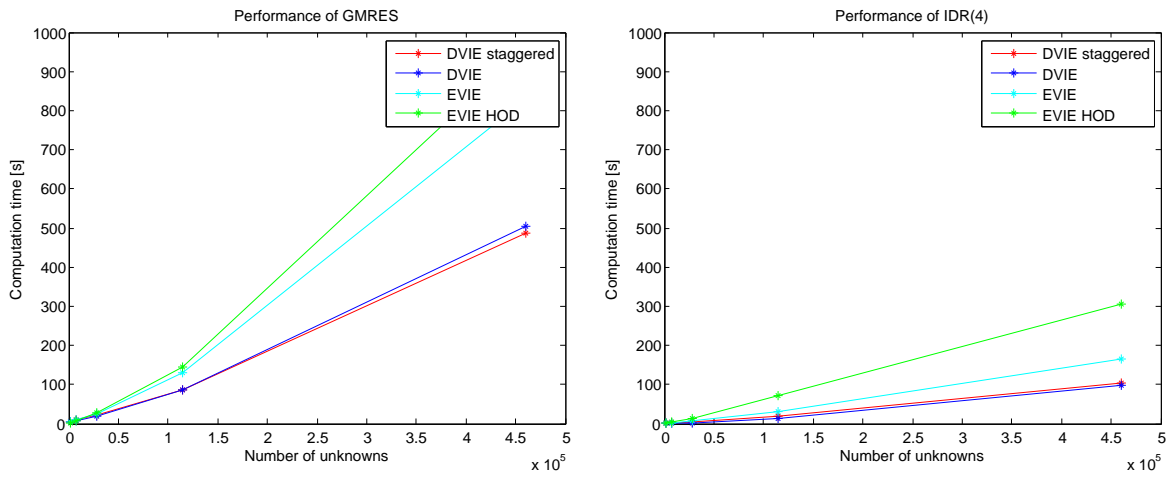


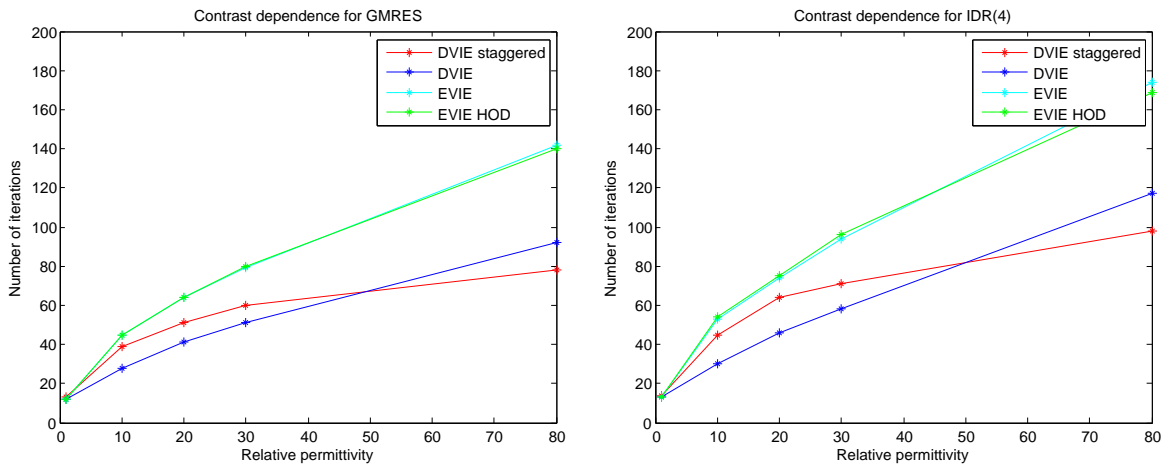
Figure 8.16: Convergence behavior of GMRES and IDR(4).



(a) GMRES

(b) IDR(4)

Figure 8.17: The computation time as a function of the number of unknowns for the different solvers.



(a) GMRES

(b) IDR(4)

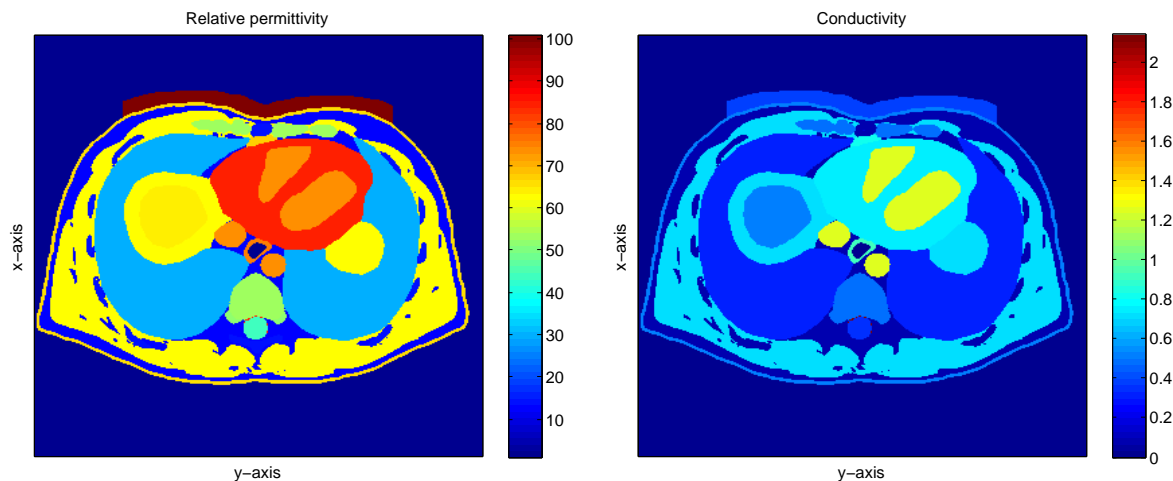
Figure 8.18: Contrast dependence for the different solvers.

9

BACK TO REALITY

The previous part of this research focused on a simple benchmark problem to study the accuracy of different methods. From this, two types of errors came forward in Chapter 8. Since the actual goal is to accurately model the human body with dielectric pads, which is an even stronger inhomogeneous medium with relative permittivities that can reach values over 300, it is interesting to study the effect of the errors on human body simulations. This chapter will take a closer look at this effect.

The many different organs and tissue types make the human body a strongly inhomogeneous medium. The electromagnetic properties of the tissue types have been studied years ago and are stored in a family of body models. Figure 9.1 shows the permittivity and conductivity values for one slice of the male 'Duke' body model on high resolution (332×332 grid). The relative permittivity values in this slice vary between 0 and 90 and the conductivity values between 0 S/m and 1.3 S/m, which is enough to expect erroneous behavior. But how bad are these errors in practice? In this stadium it is difficult to simulate entirely realistic situations, because MRI involves scattering in three dimensions and therefore 3D mathematical models. To take the first step toward reality, a pad with a relative permittivity value of 100 and conductivity of 0.4 S/m has been placed on the breast of the body model 'Duke'. In this way the effect of high permittivity materials on the accuracy of the derived methods can be studied.



(a) Permittivity values in space.

(b) Conductivity values in space.

Figure 9.1: Material properties of the human body with a dielectric pad placed on the breast.

Clearly, there is no way to find an expression for the analytical solution of scattering on a human body model. Therefore high resolution (332×332) images have been provided in Figure 9.2a and Figure 9.2b to give the

reader a good idea of how the fields are supposed to propagate. Results have been obtained with the DVIE method on a staggered grid with a plane wave propagating in the x -direction (downward) incident on the body. IDR(7) has been used as iterative solver as Chapter 8 advises.

It should be noted that, although a realistic frequency of 100 MHz has been used in the simulations, the incident field in the simulations is not realistic since in a real MRI scan the incident field arrives from multiple angles. However, for the purpose of this chapter it is sufficient to study a plane wave that is approaching from one angle.

9.1. ACCURACY

Along the boundaries of tissue types a dotted pattern can be recognized that looks like the scattering pattern on the boundary of cylinder layers in Chapter 8. It has been discussed that these types of errors remain very local (around three cells), and seem therefore not very alarming. The other types of errors, which have an effect on the internal fields in media, are demonstrated in Figures 9.2c-9.2f. Where the DVIE method on a low resolution staggered grid follows the high resolution result quite well, the DVIE method on a low resolution non-staggered grid does not provide reliable results. Similar results can be expected with the EVIE method on a non-staggered grid, because the EVIE and the DVIE method on non-staggered grids showed inaccurate results for the two-layer cylinder test case. The inaccurate behavior of the non-staggered discretizations on low resolution can lead to wrongly predicted specific absorption rates, and this again brings forward that extreme caution should be taken when choosing a discretization scheme.

In Chapter 8 a smoothing procedure has been proposed to eliminate the local jumps in the two-layer cylinder test case. This smoothing procedure can be used to improve the overall view of the scattering patterns in human body simulations. Figures 9.3e and 9.3f show the results after smoothing the contrast with a 2×2 filter. Figures 9.3c and 9.3d show the same fields as in Figures 9.2c and 9.2d, but the encircled areas additionally show the areas that have improved most. The main advantage of the smoothing procedure is that the smoothed figures are less noisy, but also some detail is lost. The loss of detail intensifies for larger filter sizes.

9.2. COMPUTATION TIME

Chapter 8 already showed that IDR(s) reduces the computation time considerably and that the shortest computation times can be expected with $s = 7$ for the DVIE method on a staggered grid.

In order to calculate the low resolution solution in Figure 9.2a and Figure 9.2b with IDR(7), MATLAB takes 1.19 seconds on a HP ZBook 14 Mobile Workstation. This computation time is so small that extensions to 3D simulations for low resolutions are unlikely to cause troubles. Low resolution images can be used to predict the location of high intensity fields.

If the goal is not to predict the location of high intensity fields but to analyze the fields in more detail, then finer grids are needed. In order to calculate the high resolution solution in Figure 9.2c and Figure 9.2d with IDR(7), MATLAB takes 99 seconds. However, in practice grids somewhere in between already predict the solution sufficiently accurate. Extensions to 3D simulations for high resolution images is a bigger challenge than for low resolution images, but with the help of GPU clusters and efficient programming techniques there is a good chance of keeping the computation time within bounds.

In the end, both the smoothed and the non-smoothed figures can be used to analyze the electric fields in the human body and the iterative solver IDR(s) produces the results within a reasonable amount of time. The most important lesson that should be learned from the human body simulations is that straightforward non-staggered grids do not perform satisfactory in combination with the rooftop weighting procedure for medical simulations. A staggered grid has a very good effect on the accuracy of the solutions and performs well even on low resolution.

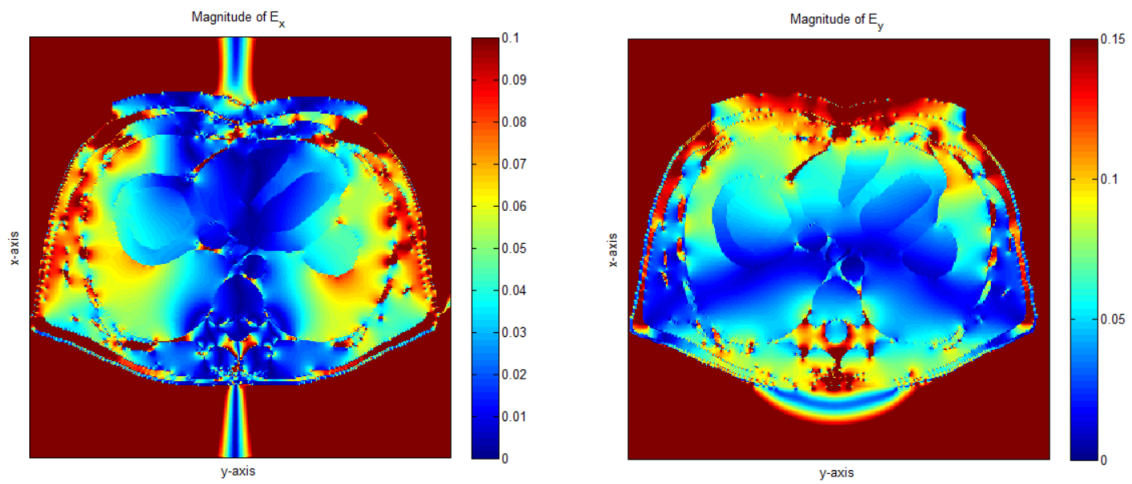
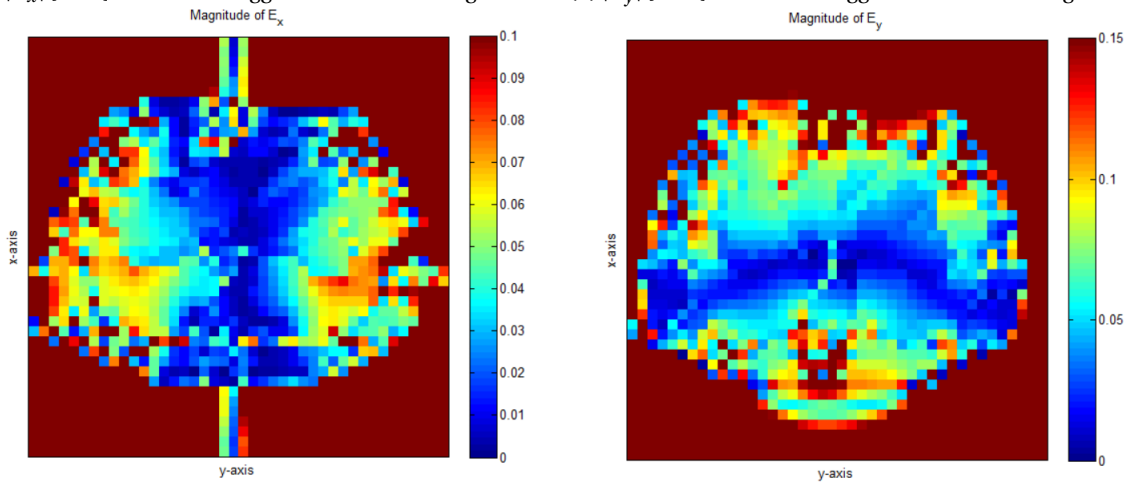
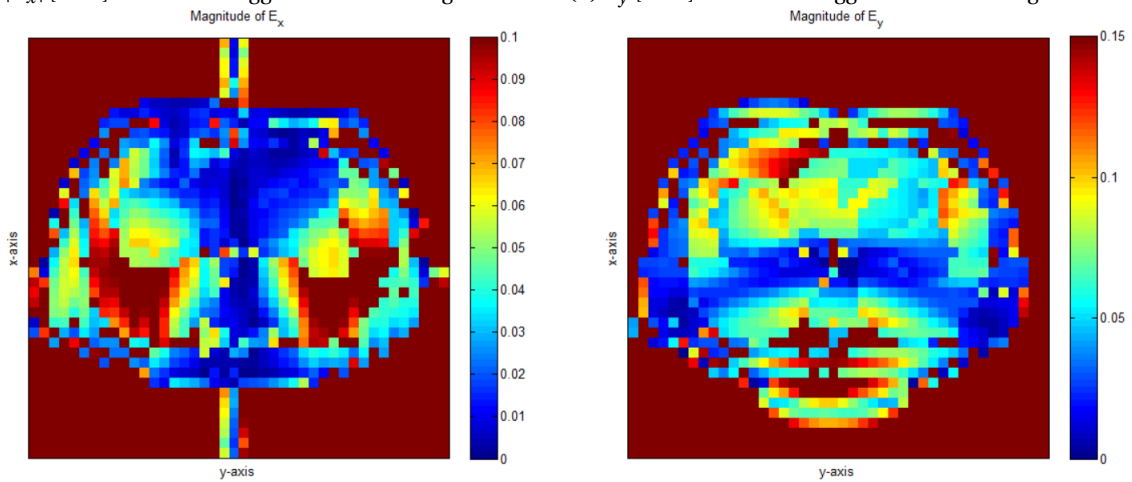
(a) $|E_x|$ [V/m] with DVIE staggered on a 332×332 grid.(b) $|E_y|$ [V/m] with DVIE staggered on a 332×332 grid.(c) $|E_x|$ [V/m] with DVIE staggered on a 42×42 grid.(d) E_y [V/m] with DVIE staggered on a 42×42 grid.(e) $|E_x|$ [V/m] with DVIE on a 42×42 grid.(f) $|E_y|$ [V/m] with DVIE on a 42×42 grid.

Figure 9.2: Scattering on one slice of the human body model 'Duke'.

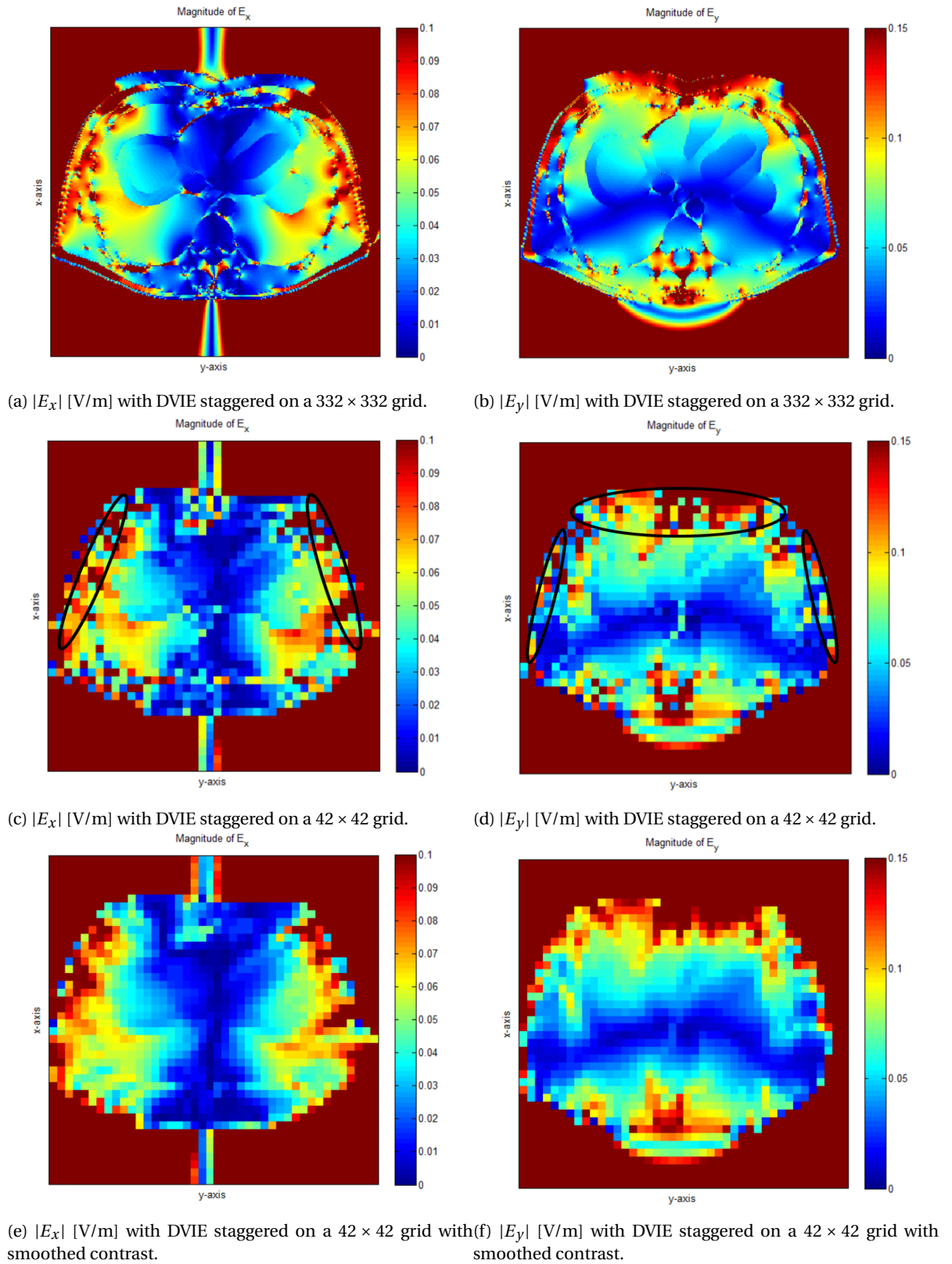


Figure 9.3: Comparison between the smoothed and the original fields.

10

CONCLUSION

The aim of this research was to find an accurate solution of Maxwell's equations that is obtained within short computation time. To this end different discretization schemes have been compared and higher order difference schemes have been implemented to find possible improvements on the existing schemes. A smoothing procedure has been proposed for eliminating strongly local large jumps and finally, the findings have been verified by testing on a human body model 'Duke'.

In order to shorten the computation time of the scattering problem, the more recent method IDR(s) has been compared with the more commonly known method GMRES.

Two types of errors have been found while studying the accuracy of different discretization schemes. Errors of the first type have a strongly local behavior for fine grids and they do not vanish in the limit. That these local large peaks are completely gone in the case of scattering on a square-shaped object seems to indicate that errors of the first type are caused by staircasing.

Errors of the second type are visible in the internal fields as well and decrease with the space between grid nodes. These errors vanish eventually and it turned out that the speed with which this happens depends largely on the approximation scheme for the mixed derivative term.

All studied methods suffer from both types of errors, but in varying degrees. The staggered grid is very efficient in reducing the errors of the second type. It also shows smaller peaks on the inner boundary layer of the cylinder. For these two reasons the DVIE method on a staggered grid is concluded to result in the most accurate solution, especially for coarser grids. A contrast dependence study also showed that for larger permittivity values the staggered method is much more accurate than the non-staggered methods. Human body simulations confirm that the DVIE method on a staggered grid performs very well, while non-staggered methods involve false heat production on low resolution.

A 4×4 averaging filter has shown to eliminate the strongly local large jumps in the cylinder test case. Larger filters have the capability of eliminating stronger jumps, and choosing the averaging filter too small results in a partly vanished jump. Although the smoothing procedure is effective in reducing the staircasing error, it also affects the internal fields for coarse grids. One should decide per application whether either the staircasing error should be reduced or the best overall accuracy should be obtained. In any case, real body simulations do not require a smoothing procedure because the local behavior of the errors makes sure that false heat production is kept to a minimum. A 2×2 averaging filter can be applied to provide less noisy images.

The iterative method IDR(s) shows excellent performance in reducing the computation time of the scattering problem for all studied grid sizes. The number of iterations turns out to be hardly dependent on the grid size, which might be an advantageous result of the volume integral approach. The DVIE method and the DVIE method on a staggered grid show similar convergence behavior and result in the shortest computation times. Most gain with respect to the other discretizations is to be made for fine grids. Fine grids are unavoidable in MRI applications and therefore either the DVIE method or the DVIE method on a staggered grid would be recommended purely based on the computation times. A study on the choice of s shows that the shortest computation times are obtained with $s = 7$ and this value is therefore advised for further research that studies the rooftop expansion procedure on a staggered grid. IDR(s) brings extensions to fast 3D human body simulations one step closer.

Combining the above findings, the DVIE method on a staggered grid is the only method that meets both the requirement of obtaining an accurate solution on low resolution and of obtaining the solution fast. These findings can be taken into account in the development of medical tools and may offer insights for further research. Suggestions for improvement will be proposed in the final chapter.

11

DISCUSSION

During this research, insight has been obtained into the method of moments with the rooftop basis functions in particular. This method is used in multiple applications and although it has advantages over other discretization methods, questions regarding several steps in the procedure arose in this study.

The first step that should be argued is the neglect of the boundary integral appearing in the weak form. The neglect of the boundary terms is motivated by the fact that the basis functions in normal direction are chosen equal to zero on the boundary of the domain. However, in this reasoning the basis function corresponding to the node located on the boundary is ignored, which is only allowed in case of homogeneous Dirichlet boundary conditions for the divergence of the vector potential. The divergence of the vector potential does not satisfy homogeneous Dirichlet boundary conditions, so new methods might consider taking into account boundary terms with correct boundary conditions. Boundary conditions are also needed for applying the weighting procedure consistently. Currently, homogeneous Dirichlet boundary conditions are wrongly applied for the electric field and the electric displacement.

A second point of attention is the transformation of the electric fields on a staggered grid back to the fields on a non-staggered grid. This is done by interpolation, while interpolation with discontinuous functions is unreliable. It might be worthwhile to use the material boundary conditions in deriving suitable interpolation rules for the electric field. The same can be done for transforming the contrast from non-staggered grid to staggered grid.

Next to these critical remarks, suggestions for future work will be given below.

- The accuracy of the methods has been studied by comparing the numerical results with an analytical solution. This analytical solution is a series representation and in order to implement the expression numerically, the infinite sum has to be terminated after a chosen number of terms. The accuracy of the analytical solution increases with the number of terms, but in practice numerical errors are introduced by solving close to singular systems for the coefficients. Improvements will probably be possible here after finding clever expressions for the coefficients. This will be left for future work.
- In this project only 2D equations have been studied after assuming that the fields are invariant in z -direction. In reality, the human body does not have the perfect shape of a cylinder and variations in z -direction will occur. Further research should compare the accuracies of different methods in 3D to find out whether also in this case the DVIE method on a staggered grid performs much better than the non-staggered methods.
- As mentioned earlier, Galerkin convergence is guaranteed only if the test functions are chosen in the dual space of the operator range. In order to construct mathematically correct models in which Galerkin convergence is guaranteed, it is an option to switch to the JVIE formulation whose operator maps from $[L^2(\mathbb{R}^3)]^3 \mapsto [L^2(\mathbb{R}^3)]^3$. It is unknown what the effect of the different operator spaces on the accuracy of the obtained solutions is in practice and therefore it would be useful to investigate this further. However, care should be taken in treating the JVIE formulation, since direct partial integration results in a derivative on the discontinuous contrast function.

- The method of moments with rooftop basis functions on a rectangular grid has the advantage of an easy to construct system matrix. Moreover, FFT algorithms are used to efficiently compute matrix-vector products. Best results are expected when working with boundary conforming elements to avoid staircasing. Due to time limitations this is not applicable method for MRI, but a compromise between the rectangular grid and the boundary conforming elements might be feasible. For further research a structured triangular grid with grid nodes as vertices is proposed. A comparison between this method and the studied methods in this thesis will provide insight in the effect of the position of grid nodes at vertices or at cell centers.
- Finally, part of this research focused on the local large peaks on material interfaces. Results of scattering on a square shaped object strongly suggest that these errors are caused by staircasing. Human body simulations indicate that the effect of staircasing errors is not alarming. However, if one would prefer to avoid these errors, boundary conforming elements could be chosen with the cost of computation time.

There will always be many ways of modeling electromagnetic fields and one should balance the benefits with the costs when choosing a suitable procedure. Modeling electromagnetic fields clearly remains a challenging task with much work left for future research. The above suggestions offer directions in which the quality of models and their outcomes can possibly be improved.

A

LIST OF USED VARIABLES AND THEIR SI UNITS

Symbol	SI units	Quantity
H	A/m	Magnetic field intensity
J	A/m ²	Electric current density
D	C/m ²	Electric displacement
E	V/m	Electric field
B	T	Magnetic field
J^{ext}	A/m ²	External electric current density
K^{ext}	V/m ²	External magnetic current density
J^{ind}	A/m ²	Induced electric current density
K^{ind}	V/m ²	Induced magnetic current density
J^{tot}	A/m ²	Total electric current density
H^{inc}	A/m	Magnetic incident field
E^{inc}	V/m	Electric incident field
H	A/m	Magnetic scattered field
E	V/m	Electric scattered field
<i>f</i>	Hz	Frequency
<i>ω</i>	rad/s	Angular Frequency
<i>k_b</i>	1/m	Wave number
<i>χ_e</i>	1	Electric susceptibility
<i>χ_m</i>	1	Magnetic Susceptibility
<i>ε</i>	F/m	Permittivity
<i>μ</i>	H/m	Permeability
<i>σ</i>	S/m	Conductivity
<i>ε₀</i>	F/m	Permittivity in vacuum
<i>μ₀</i>	H/m	Permeability in vacuum
<i>t</i>	s	Time
<i>ρ</i>	C/m ³	Volume charge density / radius
<i>c₀</i>	m/s	speed of light / wave speed in vacuum

B

INVERSE FOURIER TRANSFORM OF THE GREEN'S FUNCTION

First the identity

$$k_b^2 = \left(\sqrt{-\eta_0 \zeta_0}\right)^2 = \left(i\sqrt{\eta_0 \zeta_0}\right)^2 = -\eta_0 \zeta_0 = -\gamma_0^2$$

is introduced. The Green's function therefore translates in ω -domain to

$$\tilde{g} = \frac{1}{\mathbf{k}^T \mathbf{k} - k_b^2}$$

and in two dimensions,

$$\begin{aligned} \hat{g}(\mathbf{x}, \omega) &= \frac{1}{(2\pi)^2} \int_{\mathbf{k} \in \mathbb{R}^2} \frac{1}{\mathbf{k}^T \mathbf{k} - k_b^2} e^{-i\mathbf{k} \cdot \mathbf{x}} dV \\ &= \frac{1}{(2\pi)^2} \int_{\mathbf{k} \in \mathbb{R}^2} \frac{1}{k_1^2 + k_2^2 - k_b^2} e^{-ik_1 x_1 - ik_2 x_2} dV \\ &\stackrel{\Gamma = \sqrt{k_b^2 - k_1^2}}{=} \frac{1}{(2\pi)^2} \int_{k_1 \in \mathbb{R}} e^{-ik_1 x_1} \int_{k_2 \in \mathbb{R}} \frac{1}{k_2^2 - \Gamma^2} e^{-ik_2 x_2} dk_2 dk_1. \end{aligned}$$

Since the function in the inner integral has two simple poles, the residue theorem gives

$$\int_C \frac{1}{z^2 - \Gamma^2} e^{-izx_2} dz = 2\pi i \operatorname{Res}(f, \Gamma) = \frac{\pi i}{\Gamma} e^{-i\Gamma|x_2|},$$

where C is the closed curve along the semicircle with radius R in the upper half plane and $f(z) = \frac{1}{z^2 - \Gamma^2} e^{-izx_2}$.

The integral along the curved path $\beta_r = R e^{it}$ drops to zero when $R \rightarrow \infty$, since

$$\left| \int_{\beta_r} \frac{1}{z^2 - \Gamma^2} e^{-izx_2} dz \right| = \left| \int_{\beta_r} \frac{Ri}{R^2 e^{2it} - \Gamma^2} e^{i(t - R e^{it} x_2)} dt \right| \leq \int_{\beta_r} \frac{|Ri|}{|R^2 e^{2it} - \Gamma^2|} \left| e^{i(t - R e^{it} x_2)} \right| dt \leq \int_{\beta_r} \frac{1}{\left| R e^{2it} - \frac{\Gamma^2}{R} \right|} dt.$$

Therefore

$$\int_{k_2 \in \mathbb{R}} \frac{1}{k_2^2 - \Gamma^2} e^{-ik_2 x_2} dk_2 = \frac{\pi i}{\Gamma} e^{-i\Gamma|x_2|}$$

and

$$\begin{aligned} \hat{g}(\mathbf{x}, \omega) &= \frac{i}{4\pi} \int_{k_1 \in \mathbb{R}} \frac{e^{-ik_1 x_1 - i\Gamma|x_2|}}{\Gamma} dk_1 \\ &= \frac{i}{4\pi} \int_{k_1 \in \mathbb{R}} \frac{e^{-ik_1 x_1 + \sqrt{k_b^2 - k_1^2}|x_2|}}{\sqrt{k_b^2 - k_1^2}} dk_1. \end{aligned} \tag{B.1}$$

In (B.1) a Hankel function of the second kind can be recognized. [30] states

$$\hat{g}(\mathbf{x}, \omega) = -\frac{i}{4} H_0^{(2)}(k_b |x|).$$

C

WEAKENING OF THE GREEN'S FUNCTION

The function

$$\hat{g}(\mathbf{x}, \omega) = -\frac{i}{4} H_0^{(2)}(k_b |\mathbf{x}|)$$

has a singularity at $\mathbf{x} = 0$.

Recall that the Green's function satisfies

$$\nabla^2 \hat{g}(\mathbf{x}, \omega) + k_b^2 \hat{g}(\mathbf{x}, \omega) = -\delta(\mathbf{x}).$$

In order to avoid the singularity in the Green's function, the whole function is approximated by a 'weakened' Green's function, that satisfies

$$\nabla^2 \hat{g}^w(\mathbf{x}, \omega) + k_b^2 \hat{g}^w(\mathbf{x}, \omega) = -f(\mathbf{x}) \quad (\text{C.1})$$

with

$$f(\mathbf{x}) = \begin{cases} \frac{1}{\pi a^2} & \text{if } \mathbf{x} \in \mathbb{D} \\ 0 & \text{if } \mathbf{x} \notin \mathbb{D} \end{cases}$$

and \mathbb{D} a circular domain with radius $a = \frac{1}{2} \min\{\Delta x, \Delta y\}$. In this way \mathbb{D} is contained in one cell and the function $f(\mathbf{x})$ approaches the Dirac delta function as $a \downarrow 0$.

The solution of (C.1) is given by

$$\begin{aligned} \hat{g}^w(\mathbf{x}, \omega) &= \int_{\mathbf{x}' \in \mathbb{R}^2} \hat{g}(\mathbf{x} - \mathbf{x}', \omega) f(\mathbf{x}') dV' \\ &= \frac{1}{\pi a^2} \int_{\mathbf{x}' \in \mathbb{D}} \hat{g}(\mathbf{x} - \mathbf{x}', \omega) dV' \end{aligned}$$

In order to actually compute \hat{g}^w the problem is split in two cases: $\mathbf{x} \notin \mathbb{D}$ and $\mathbf{x} \in \mathbb{D}$. In both cases the integral

$$\hat{g}^w(\mathbf{x}, \omega) = -\frac{i}{4\pi a^2} \int_{\mathbf{x}' \in \mathbb{D}} H_0^{(2)}(k_b |\mathbf{x} - \mathbf{x}'|) dV' \quad (\text{C.2})$$

has to be evaluated.

The Hankel function inside the integral can be written as an infinite sum, using the addition theorem for the Hankel function $H_0^{(2)}$ which can be found in [22]. With ϕ the angle between \mathbf{x} and \mathbf{x}' and J_k the k -th order Bessel function of the first kind, the result is given by

$$H_0^{(2)}(k_b |\mathbf{x} - \mathbf{x}'|) = \begin{cases} \sum_{k=-\infty}^{\infty} J_k(k_b |\mathbf{x}|) H_k^{(2)}(k_b |\mathbf{x}'|) e^{ik\phi}, & |\mathbf{x}| \leq |\mathbf{x}'| \\ \sum_{k=-\infty}^{\infty} J_k(k_b |\mathbf{x}'|) H_k^{(2)}(k_b |\mathbf{x}|) e^{ik\phi}, & |\mathbf{x}'| \leq |\mathbf{x}| \end{cases} \quad (\text{C.3})$$

In the first case, where $\mathbf{x} \notin \mathbb{D}$, it holds that $|\mathbf{x}| > |\mathbf{x}'|$ for all $\mathbf{x}' \in \mathbb{D}$ and therefore

$$\hat{g}^w(\mathbf{x}, \omega) = -\frac{i}{4\pi a^2} \int_{\mathbf{x}' \in \mathbb{D}} \sum_{k=-\infty}^{\infty} J_k(k_b |\mathbf{x}'|) H_k^{(2)}(k_b |\mathbf{x}|) e^{ik\phi} dV'. \quad (\text{C.4})$$

Transforming (C.4) into polar coordinates, gives

$$\begin{aligned}
\hat{g}^w(\mathbf{x}, \omega) &= -\frac{i}{4\pi a^2} \int_0^{2\pi} \int_0^a \sum_{k=-\infty}^{\infty} J_k(k_b r) H_k^{(2)}(k_b |\mathbf{x}|) e^{ik\phi} r dr d\phi \\
&= -\sum_{k=-\infty}^{\infty} \frac{i}{4\pi a^2} H_k^{(2)}(k_b |\mathbf{x}|) \int_0^{2\pi} e^{ik\phi} d\phi \int_0^a J_k(k_b r) r dr \\
&= -\frac{i}{2a^2} H_0^{(2)}(k_b |\mathbf{x}|) \int_0^a J_0(k_b r) r dr \\
&= -\frac{i}{2a^2} H_0^{(2)}(k_b |\mathbf{x}|) \frac{1}{k_b^2} \int_0^{k_b a} z J_0(z) dz \\
&= -\frac{i}{2a^2} H_0^{(2)}(k_b |\mathbf{x}|) \frac{1}{k_b^2} \int_0^{k_b a} \frac{d}{dz} (z J_1(z)) dz \\
&= -\frac{i}{2ak_b} H_0^{(2)}(k_b |\mathbf{x}|) J_1(k_b a).
\end{aligned}$$

In the second case, where $\mathbf{x} \in \mathbb{D}$, only $\hat{g}^w(\mathbf{0}, s)$ is of interest for the discretization procedure. To obtain this value, $|\mathbf{x}| = \varepsilon < a$ is fixed after which the limit $\varepsilon \downarrow 0$ is taken. The integration region is split in two parts: the circular disc \mathbb{D}_ε with radius ε and the rest of \mathbb{D} , denoted by $\mathbb{D} \setminus \mathbb{D}_\varepsilon$. In the point $\mathbf{x} = \mathbf{0}$ (C.2) now becomes

$$\hat{g}^w(\mathbf{0}, \omega) = -\frac{i}{4\pi a^2} \lim_{\varepsilon \downarrow 0} \left[\int_{\mathbf{x}' \in \mathbb{D}_\varepsilon} H_0^{(2)}(k_b |\mathbf{x} - \mathbf{x}'|) dV' + \int_{\mathbf{x}' \in \mathbb{D} \setminus \mathbb{D}_\varepsilon} H_0^{(2)}(k_b |\mathbf{x} - \mathbf{x}'|) dV' \right]. \quad (\text{C.5})$$

For the second integral in (C.5) it holds that $|\mathbf{x}| < |\mathbf{x}'|$ and (C.3) tells that

$$\begin{aligned}
\int_{\mathbf{x}' \in \mathbb{D} \setminus \mathbb{D}_\varepsilon} H_0^{(2)}(k_b |\mathbf{x} - \mathbf{x}'|) dV' &= \int_{\mathbf{x}' \in \mathbb{D} \setminus \mathbb{D}_\varepsilon} \sum_{k=-\infty}^{\infty} J_k(k_b \varepsilon) H_k^{(2)}(k_b |\mathbf{x}'|) e^{ik\phi} dV' \\
&= \sum_{k=-\infty}^{\infty} J_k(k_b \varepsilon) \int_0^{2\pi} e^{ik\phi} d\phi \int_\varepsilon^a H_k^{(2)}(k_b r) r dr \\
&= J_0(k_b \varepsilon) \frac{2\pi}{k_b^2} \int_{k_b \varepsilon}^{k_b a} H_0^{(2)}(z) z dz \\
&= J_0(k_b \varepsilon) \frac{2\pi}{k_b} \left(H_1^{(2)}(k_b a) a - H_1^{(2)}(k_b \varepsilon) \varepsilon \right). \quad (\text{C.6})
\end{aligned}$$

For the first integral in (C.5) it holds that $|\mathbf{x}| > |\mathbf{x}'|$ and (C.3) tells that

$$\begin{aligned}
\int_{\mathbf{x}' \in \mathbb{D}_\varepsilon} H_0^{(2)}(k_b |\mathbf{x} - \mathbf{x}'|) dV' &= \int_{\mathbf{x}' \in \mathbb{D}_\varepsilon} \sum_{k=-\infty}^{\infty} J_k(k_b |\mathbf{x}'|) H_k^{(2)}(k_b |\mathbf{x}|) e^{ik\phi} dV' \\
&= \sum_{k=-\infty}^{\infty} H_k^{(2)}(k_b \varepsilon) \int_0^{2\pi} e^{ik\phi} d\phi \int_0^\varepsilon J_k(k_b r) r dr \\
&= 2\pi H_0^{(2)}(k_b \varepsilon) \int_0^\varepsilon J_0(k_b r) r dr \\
&= \frac{2\pi \varepsilon}{k_b} H_0^{(2)}(k_b \varepsilon) J_1(k_b \varepsilon). \quad (\text{C.7})
\end{aligned}$$

Substitution of (C.6) and (C.7) in (C.5) and taking the limit gives

$$\begin{aligned}
\hat{g}^w(\mathbf{0}, \omega) &= -\frac{i}{4\pi a^2} \lim_{\varepsilon \downarrow 0} \left[\frac{2\pi \varepsilon}{k_b} H_0^{(2)}(k_b \varepsilon) J_1(k_b \varepsilon) + J_0(k_b \varepsilon) \frac{2\pi}{k_b} \left(H_1^{(2)}(k_b a) a - H_1^{(2)}(k_b \varepsilon) \varepsilon \right) \right] \\
&= -\frac{i}{2k_b a} \left(H_1^{(2)}(k_b a) - \frac{2i}{\pi k_b a} \right).
\end{aligned}$$

The weakened Green's function is therefore given by

$$\hat{g}^w(\mathbf{x}, \omega) = \begin{cases} -\frac{i}{2ak_b} H_0^{(2)}(k_b |\mathbf{x}|) J_1(k_b a) & \text{if } \mathbf{x} \notin \mathbb{D} \\ -\frac{i}{2k_b a} \left(H_1^{(2)}(k_b a) - \frac{2i}{\pi k_b a} \right) & \text{if } \mathbf{x} = \mathbf{0} \end{cases}$$

and this function can be used to approximate the Green's function in all grid points.

BIBLIOGRAPHY

- [1] M. M. Botha, *Solving the volume integral equations of electromagnetic scattering*, Journal of Computational Physics **218**, 141 (2006).
- [2] N. Joachimowicz and C. Pichot, *Comparison of three integral formulations for the 2-D TE scattering problem*, IEEE Transactions on Microwave Theory and Techniques **38**, 178 (1990).
- [3] J. Markkanen, C.-C. Lu, X. Cao, and P. Ylä-Oijala, *Analysis of volume integral equation formulations for scattering by high-contrast penetrable objects*, IEEE Transactions on Antennas and Propagation **60**, 2367 (2012).
- [4] A. Polimeridis, J. Villena, L. Daniel, and J. White, *Stable FFT-JVIE solvers for fast analysis of highly inhomogeneous dielectric objects*, Journal of Computational Physics **269**, 280 (2014).
- [5] J. P. Kottmann and O. J. Martin, *Accurate solution of the volume integral equation for high-permittivity scatterers*, IEEE Transactions on Antennas and Propagation **48**, 1719 (2000).
- [6] J. Markkanen and P. Ylä-Oijala, *Discretization of electric current volume integral equation with piecewise linear basis functions*, IEEE Transactions on Antennas and Propagation **62**, 4877 (2014).
- [7] P. Zwamborn and P. M. van den Berg, *A weak form of the conjugate gradient FFT method for two-dimensional TE scattering problems*, IEEE Transactions on Microwave Theory and Techniques **39**, 953 (1991).
- [8] F. Nataf, *Absorbing boundary conditions and perfectly matched layers in wave propagation problems*, Direct and Inverse Problems in Wave Propagation and Applications , 219 (2013).
- [9] B. J. Kooij and P. M. van den Berg, *Nonlinear inversion in TE scattering*, IEEE Transactions on Microwave Theory and Techniques **46**, 1704 (1998).
- [10] R. Remis and E. Charbon, *An electric field volume integral equation approach to simulate surface plasmon polaritons*, Advanced Electromagnetics **2**, 15 (2013).
- [11] H. H. Schild, *MRI Made Easy: (-well Almost)* (Berlex Laboratories, 1992).
- [12] P. de Heer, W. Brink, B. Kooij, and A. Webb, *Increasing signal homogeneity and image quality in abdominal imaging at 3T with very high permittivity materials*, Magnetic Resonance in Medicine **68**, 1317 (2012).
- [13] W. M. Brink, A. M. van der Jagt, M. J. Versluis, B. M. Verbist, and A. G. Webb, *High permittivity dielectric pads improve high spatial resolution magnetic resonance imaging of the inner ear at 7T*, Investigative radiology **49**, 271 (2014).
- [14] W. M. Brink and A. G. Webb, *High permittivity pads reduce specific absorption rate, improve B1 homogeneity, and increase contrast-to-noise ratio for functional cardiac MRI at 3T*, Magnetic Resonance in Medicine **71**, 1632 (2014).
- [15] N. Budko, *Electromagnetic radiation, scattering and imaging, Delft 2004*, .
- [16] R. G. Martín, *Electromagnetic field theory for physicists and engineers: Fundamentals and applications*, Grupo de Electromagnetismo de Granada (2006).
- [17] G. Beylkin, C. Kurcz, and L. Monzón, *Fast convolution with the free space Helmholtz Green's function*, Journal of Computational Physics **228**, 2770 (2009).
- [18] M. van Beurden and S. van Eijndhoven, *Well-posedness of domain integral equations for a dielectric object in homogeneous background*, Journal of Engineering Mathematics **62**, 289 (2008).

- [19] M. van Beurden and S. van Eijndlioven, *Gaps in present discretization schemes for domain integral equations*, in *International Conference on Electromagnetics in Advanced Applications, 2007. ICEAA 2007*. (IEEE, 2007) pp. 673–675.
- [20] B. H. Jung, *Time and Frequency Domain Solutions of EM Problems: Using Integral Equations and a Hybrid Methodology* (IEEE Press, 2010).
- [21] W. C. Chew, *Waves and fields in inhomogeneous media*, Vol. 522 (IEEE press New York, 1995).
- [22] C. Balanis, *Advanced engineering electromagnetics*, Vol. 20 (Wiley New York, 1989).
- [23] L. Hu, L.-W. Li, T.-S. Yeo, and R. Vahldieck, *An accurate and robust approach for evaluating VIE impedance matrix elements using SWG basis functions*, in *Microwave Conference, 2008. APMC 2008. Asia-Pacific* (IEEE, 2008) pp. 1–4.
- [24] Y. Saad and M. H. Schultz, *GMRES: A generalized minimal residual algorithm for solving nonsymmetric linear systems*, *SIAM Journal on Scientific and Statistical Computing* **7**, 856 (1986).
- [25] P. Sonneveld and M. B. van Gijzen, *IDR(s): A family of simple and fast algorithms for solving large nonsymmetric systems of linear equations*, *SIAM Journal on Scientific Computing* **31**, 1035 (2008).
- [26] M. B. van Gijzen and P. Sonneveld, *The IDR(s) method for solving nonsymmetric systems: a performance study for CFD problems*, *High Performance Algorithms for Computational Science and Their Applications* (2008).
- [27] J. Häggblad and O. Runborg, *Accuracy of staircase approximations in finite-difference methods for wave propagation*, *Numerische Mathematik* **128**, 741 (2014).
- [28] E. Blåsten, L. Päivärinta, and J. Sylvester, *Corners always scatter*, *Communications in Mathematical Physics* **331**, 725 (2014).
- [29] M. B. van Gijzen and P. Sonneveld, *Algorithm 913: An elegant IDR(s) variant that efficiently exploits biorthogonality properties*, *ACM Transactions on Mathematical Software (TOMS)* **38**, 5 (2011).
- [30] J. T. Fokkema and P. M. van den Berg, *Seismic applications of acoustic reciprocity* (Elsevier, 2013).

